Experimental investigations on the preferential concentration and clustering phenomena of wall-bounded gas-solid flows

A DISSERTATION
SUBMITTED TO THE FACULTY OF THE GRADUATE SCHOOL
OF THE UNIVERSITY OF MINNESOTA
BY

Kee Onn Fong

IN PARTIAL FULFILLMENT OF THE REQUIREMENTS
FOR THE DEGREE OF
DOCTOR OF PHILOSOPHY

Dr. Filippo Coletti

May, 2021

Acknowledgements

The journey of discovery that resulted in this thesis is not one that can be undertaken alone – rather, it is a culmination of decades of nurturing, from a young age where the mindsets of curiosity and thirst for knowledge is instilled; through adolescence where teachers and educators impart knowledge and the drive to succeed; culminating in graduate school, where with the support of advisors and fellow graduate students that one can finally embark on their very first project of original research. My own path is very much similar, and I have many people to thank for their support on my journey.

As fate would have it, I met my Ph.D. advisor, Prof. Filippo Coletti in January 2014 while seeking a part-time job in my junior year of college. With his startup funds and unbridled enthusiasm, I had my first taste of experimental fluid mechanics and got hooked. The excitement of being on the leading edge of fluids research, doing experiments where results are eagerly awaited by computational collaborators, the satisfaction when the flow profile matches the log-law profile of a turbulent wall-bounded flow, all of these pulled me in and the thrill of these magical moments held me together as I trudged through seven years of doing, and redoing, and redoing experiments, as I doggedly seek an answer to my hypotheses. Here Filippo does what he does best – leaving me to my devices when need be, or stepping in with help when I do not even know I needed it. Sharing moral encouragements, his past failures, and his day-to-day experiences as a new professor; all of that sustains me to complete my dream of accomplishing original research, and continue to inspire me to hopefully one day attempt the path of the professorship, with the guiding stars of service to community and scientific discovery in mind. I couldn't ask for a better advisor. Thank you, Filippo.

My completion of graduate school would also not be possible without my colleagues and the band of Akerman 30 basement lab mates. Dr. Andras Nemes, Prof. Omid

Amili, Prof. Kyle Winters, Prof. Diogo Barros, and Dr. Yan Ming Tan, your invaluable guidance and advice during the early years of grad school helped shaped the foundation on which my dissertation work stands years later. Dr. Doug Carter, Dr. Alec Petersen, Dr. Sahar Jalal, Dr. Yi Hui Tee and Dr. Peng Mun Siew, Dr. Tim Berk, Dr. Roumaissa Hassaini, Mr. Yanchong Duan, Mr. Tristan Van de Moortele, Ms. Rong Ma, and others: it was an honor to be your colleague in graduate school, slaying exams, exchanging ideas and equipment; and I hope I have helped you as much as you all helped me. Ms. Yinghui Li, Ms. Amy Tinklenberg, Mr. Henri Sanness Salmon, and Mr. Sagnik Paul: you all inspire me as the next generation of graduate students picking up the baton and continuing to advance science and discovery. It is my honor to have known all of you during my graduate school journey.

I would also like to thank my committee members who did not just give essential feedback on my research, but also played crucial roles in my undergraduate and graduate education as well as in support of my research journey. My deepest thanks to Prof. Ellen Longmire, Prof. Krishnan Mahesh, and Prof. Michele Guala. Many thanks also to Mr. Nick Sloan and Mr. Kale Hedstrom for assisting me with constructing and running the various experiments over the course of my research.

When I left home nine years ago to pursue my studies in Minnesota, the future was a blank slate and I have no idea yet what was in store. Throughout the years in undergraduate and then graduate studies, my family has always been a bedrock of financial and moral support as I hit those milestones in career and in life. I am immeasurably grateful to have my parents, Teng-Loon Fong and Kwai-Fun Yong in my life, and my siblings Yan Yi and Kee Win for being with me together on this world. I thank you all from the bottom of my heart. I am also extremely fortunate to have a lab mate who is also my best friend, a partner at work and in life, supporting me as we walk down an exciting path that is also sometimes exhausting. I am extremely grateful to my wife, Dr. Lucia Baker for her love and support throughout the years. Thank you, Luci.

Finally, from the lakes and forests of the Miní Sóta Makhóčhe to the wind-swept, coconut tree-lined beaches of Kerteh, Terengganu; I would like to extend my gratitude to the natural world that has nurtured me, and to the cities of Minneapolis and Saint Paul which has been a welcoming home away from home. I would also like to acknowledge the

funding agencies, including the National Science Foundation, the Army Research Office, and the Legislative-Citizen Commission on Minnesota Resources (LCCMR). Without their support, this research work and dissertation would not have been possible.

Dedication

To my parents, Teng-Loon Fong and Kwai-Fun Yong - none of this would have been possible without your support and sacrifices.

Abstract

The transport of solid particles by fluid flows are ubiquitous in many environmental, biomedical and industrial processes, yet a full understanding of the dynamics of these processes remain elusive. In this thesis, we present experimental investigations of two different phenomena that arises in particle-laden flows: the preferential concentration of particles in turbulent flows, and the clustering of particles in dense gas-solid flows. In the former case, we investigate inertial particles dispersed in a turbulent downward flow through a vertical channel. The working fluid is air laden with size-selected glass microspheres, having Stokes numbers $St = \mathcal{O}(10)$ and $\mathcal{O}(100)$ when based on the Kolmogorov and viscous time scales, respectively. Cases at friction Reynolds numbers $Re_\tau = 235$ and 335 and solid volume fractions $\phi_V = 3 \times 10^{-6}$ and 5×10^{-5} are considered. Between the more dilute and denser cases, substantial differences are observed in all measured statistics e.g. the particle concentration profile, mean velocity profile and the velocity fluctuation levels; consistent with a scenario in which the increase in volume fraction from $\mathcal{O}(10^{-6})$ to $\mathcal{O}(10^{-5})$ triggers two-way and local four-way coupling effects. An analysis of the spatial distributions of particle positions and velocities in the higher volume fraction cases also reveals different behavior in the core and near-wall regions. In the channel core, dense clusters form that travel faster than the less concentrated particles; whereas in the near-wall region the particles arrange in highly elongated streaks that are associated with negative streamwise velocity fluctuations. In the denser regime, we present experimental observations on the velocities and spatial distribution of particles in a three-dimensional, gas-solid riser with particle volume fractions approaching 1%. The setup consists of a vertical square channel in which air flows upwards against falling 212 µm glass spheres. We use a backlighting technique and high-speed imaging to quantify the spatial and temporally resolved particle concentration and velocity fields. By controlling the particle feed rate and the flow rate of the fluidizing air, volume fractions and bulk flow Reynolds number are adjusted independently. Results show that, in the present range of parameters, clustering of particles appear beyond a critical volume fraction regardless of fluidization velocities, influencing the mean and r.m.s. statistics and strongly modulating the two-point correlation statistics. Space-time autocorrelation

analysis reveals the convection of structures in the velocity and concentration fields, and the fluctuations of velocities and concentrations are well-described by the classic gradient diffusion hypothesis. Particle-resolved measurements reveal that particles in the riser have a sub-Poissonian spatial distribution, and their streamwise velocity fluctuations are correlated in the streamwise direction. This indicates significant hydrodynamic interaction between the particles, especially in the direction of gravity.

Contents

List of Tables

List of Figures

Chapter 1

Introduction

1.1 Particle-laden flows

The transport of solid particles by fluid flows is relevant in a broad spectrum of environmental, biomedical and industrial processes. Examples include sediment transport in rivers (Niño & Garcia, 1996), aerosol inhalation in human airways (Kleinstreuer & Zhang, 2010) and reactors in chemical engineering processes (Capecelatro *et al.*, 2014). Particle-laden flows can consist of two to three phases of matter (solids, liquids, and gas), but we focus on the scenario with solid particles in a gas. The latter (which can also be interchangeably referred to as a 'fluid') has intrinsic properties such as the density, ρ_f and the kinematic viscosity, ν; as well as the flow properties depending on the driving mechanism (pressure-driven, gravity-driven, or shear-driven) and possibly the presence of walls separated by a characteristic dimension D to contain the flow. These properties combined gives a characteristic velocity of the fluid, U_f from which a dimensionless number, the Reynolds number of the flow can be defined as $Re = U_f D/\nu$. The Reynolds number is a representation of the ratio of inertial to viscous forces in the fluid, and when inertia dominates viscous dissipation (i.e., $Re \gg 1$) the flow becomes chaotic or turbulent.

Likewise, individual solid particles (also known as the 'dispersed phase') are characterized by their intrinsic properties, such as the density, ρ_p and the physical diameter of the particle, d_p. In relation to the fluid, the particle is advected by the flow with a time delay due to its inertia, commonly characterized as the particle relaxation time, which

for a sphere in a Stokesian flow (i.e., dominated by viscous forces) is $\tau_p = \rho_p d_p^2/18\rho_f\nu$. In the limit of vanishingly small (or light) particles, the relaxation time is very small and the particles will faithfully track the fluid flow; this, for example, is the working assumption of the particle image velocimetry (PIV) technique that uses small particle tracers. The particle also exerts a feedback force onto the fluid, which is usually dissipated into heat by viscosity. However, when more than one particle is present in the flow, the collective feedback force exerted on the fluid may or may not be ignored, depending on the particle volume fraction in the system, ϕ_V which is defined by the total volume of particles divided by the total volume of the system. Elghobashi (1994) proposed a separation of particle-laden turbulent flows into three regimes based on ϕ_V. At $\phi_V \leq 10^{-6}$, the particle-fluid interaction is considered as one-way coupled: the particle motion is controlled by the fluid forces and the feedback force is negligible. At $10^{-6} \leq \phi_V \leq 10^{-3}$, the particle-fluid interaction is considered as two-way coupled: the feedback forces of the particles are no longer negligible and can modify the turbulence properties. Beyond $\phi_V \geq 10^{-3}$, 'four-way coupling' is engaged as inter-particle collisions influence particle motion and their spatial distribution.

1.2 Preferential concentration of particles in turbulent wall-bounded flows

Turbulent flows feature multiple interacting eddies, which gives rise to rich topological features in the flow (Davidson, 2015). When dispersed inertial particles are present, they are known to reside in regions of high strain rate and low vorticity if τ_p is comparable to some flow time scale (Eaton & Fessler, 1994). Collectively, this results in the particles exhibiting preferential concentration (Eaton & Fessler 1994; Monchaux *et al.* 2012; Bragg & Collins 2014; Gustavsson & Mehlig 2016; Petersen *et al.* 2019). This effect is thought to be maximized when the particle response time, τ_p, is comparable to the Kolmogorov time scale, τ_η, such that the Stokes number $St_\eta = \tau_p/\tau_\eta$ is of order unity (Wang & Maxey 1993; Fessler *et al.* 1994). Preferential concentration is observed in regions of homogeneous turbulence (Petersen *et al.* 2019), or the core region of a turbulent channel flow (Eaton & Fessler 1994) and has implications on bulk flow properties such as heat and mass transfer (Frankel *et al.* 2016).

Preferential concentration also occurs in the presence of a wall, where turbulent structures originating from the wall influences the motion and distribution of near-wall inertial particles. One effect that arises is turbophoresis, where a mean drift of the particles occurs following the negative gradient of turbulence intensity and causing an accumulation of particles near the wall (Caporaloni *et al.* 1975; Reeks 1983; Young & Leeming 1997; Guha 2008; Fouxon *et al.* 2018). For this effect, the relevant parameter usually considered is the viscous Stokes number $St^+ = \tau_p/\tau_\nu$, where τ_ν is the viscous time scale, with strong turbophoresis reported for $St^+ \sim$ 10–100 (e.g. Marchioli & Soldati 2002; Sardina *et al.* 2012*a*; Bernardini 2014). Studies of turbophoresis using techniques such as quadrant analysis have related this effect to turbulent near-wall structures, where a combination of ejection and sweep motions are mainly responsible for particle transport to and away from the wall (Marchioli & Soldati 2002, Li *et al.* 2012). In addition, inertial particles were also experimentally observed to arrange in long near-wall streaks parallel to the flow (Kaftori *et al.* 1995*a*,*b*;Niño & Garcia 1996), and numerical simulations demonstrated the role of coherent turbulent structures in determining such behavior (McLaughlin 1989; Zhang & Ahmadi 2000; Rouson & Eaton 2001; Marchioli & Soldati 2002; Soldati & Marchioli 2009; Sardina *et al.* 2012*a*; Nilsen *et al.* 2013; Richter & Sullivan 2013).

1.3 Clustering of particles in dense gas-solid flows

The process of cluster formation in dense gas-solid flows (with volume fractions large enough for the particle momentum to dominate over the gas momentum) is distinct from preferential concentration processes occurring in turbulent wall-bounded flows. The difference is best described in the review of Fullmer & Hrenya (2017), *"Clustering is intrinsic to the solids (i.e., their dissipative nature or relative motion with the gas), whereas preferential concentration relies on a hydrodynamic instability (i.e., turbulence) of the carrier fluid."* Factors concurring to clustering in this case include inter-particle collisions, effect of the interstitial fluid and of the slip velocity between the solid and gas phases (Fullmer & Hrenya 2017). The interparticle collision pathway is well-described in homogeneous cooling system studies (randomly distributed particles whose kinetic energy is entirely contained in the fluctuating velocity component, which decays in time

for the lack of any external forcing). For such a system Goldhirsch & Zanetti (1993) described a mechanism where particles dissipate energy through inelastic collisions, leading to reduced fluctuations in their relative velocities and reduced interparticle distances. These less-excited, more closely packed particles collide with their neighbours and cause more particles to migrate into their vicinity, hence forming clusters. Damping through interstitial fluid operates on a similar principle, where the fluid will quench the fluctuating motion of particles, reducing their energy and causing them to reside in the same pocket for a longer time (Fullmer & Hrenya 2017). A numerical simulation by Wylie & Koch (2000) modelled fully elastic collisions between particles which do not cluster in a vacuum but form clusters when interstitial fluid is present.

Another factor that is more relevant to gas-solid flows is the influence of slip velocity on cluster formation: as the drag coefficient generally grows with local concentration, more dilute particles approach aggregated ones, leading to a kinematic instability (Fullmer & Hrenya 2017). At the same time, clusters fall faster by gravity and also accrete by encountering other particles (Agrawal *et al.* 2001). This particular route to cluster formation is most easily investigated in a setup of particles setting in a quiescent fluid, with particles gaining slip velocity by falling under the action of gravity. Studies using this setup have observed clustering in numerical and experimental studies, for both gas-solid flows (Capecelatro *et al.* 2015; Guo & Capecelatro 2019) and also liquid-solid suspensions (Uhlmann & Doychev 2014; Huisman *et al.* 2016). If the slip velocity and particle size are large enough for the particle Reynolds number to be significant, wake-induced clustering may also occur (Kajishima & Takiguchi 2002; Uhlmann & Doychev 2014). The particle clusters formed imparts fluctuations onto the fluid medium causing a flow that is otherwise laminar to exhibit turbulence-like behaviour; this is termed as 'particle-phase turbulence' (Hrenya & Sinclair 1997) or 'cluster-induced turbulence' (Capecelatro *et al.* 2015).

Testing the limits of the clustering instability involves either using increasingly smaller particles (from ballistic to tracer-like) or varying the particle volume fraction (from extremely dilute to dense). Experiments by Weit *et al.* (2018, 2019) used a fluidized bed configuration with forced rising air and varied the mean bulk concentration in the system. They found that for low enough concentrations all particles are suspended; but when a threshold amount of particles is exceeded, clusters form and rapidly descend

to create a bed on the bottom of the vessel. The critical volume fraction was found to be $\mathcal{O}(10^{-2})$, regardless of the particle size and Reynolds number. Numerical simulations of a turbulent channel flow with increasing volume fraction show qualitatively similar results, where particle distribution patterns change from patterns characteristic of preferential concentration to meso-scale clusters resembling those observed in risers (Capecelatro *et al.* 2018). However, in a physical experiment this line of investigation is not possible with conventional fluidized bed setups (Shaffer *et al.* 2013; Varas *et al.* 2017), and a different kind of facility is needed to achieve volume fraction control, which we will describe in this dissertation.

1.4 Thesis outline

In this dissertation, we explore both the preferential concentration and clustering phenomena of particles through experiments in a laboratory setting. The different conditions and mechanisms of these two phenomena necessitates two separate experimental setups, which is elaborated on in the remainder of the dissertation. Chapter 2 describes a turbulent channel flow with 50µm glass particles, which has a relaxation time such that they are comparable to both the Kolmogorov time scale, τ_η and the viscous time scale, τ^+. Chapter 3 describes a particle riser with 212µm glass particles, in which the solid volume fraction and gas flow rate can be controlled independently, and the volume fraction is varied across the threshold for which clustering appears. Finally, the dissertation concludes with a summary of the findings from both experiments, and recommendations for future experimental and numerical investigations.

Chapter 2

Preferential concentration of particles in a turbulent channel flow

The contents of this chapter were published in the journal article: Kee Onn Fong, Omid Amili & Filippo Coletti, "Velocity and spatial distribution of particles in a turbulent channel flow", Journal of Fluid Mechanics, Vol. 872, pg. 367-406, reproduced with permission.

Wall-bounded turbulent flows laden with inertial particles are relevant to a broad spectrum of environmental, biomedical and industrial processes. The motion of heavy particles in homogeneous turbulence is already complex, featuring well-known (though not fully understood) phenomena such as preferential concentration and consequent clustering (Eaton & Fessler 1994, Monchaux *et al.* 2012, Bragg & Collins 2014, Gustavsson & Mehlig 2016). The latter is thought to be maximized when the particle response time, τ_p, is comparable to the Kolmogorov time scale, τ_η, such that the Stokes number $St_\eta = \tau_p/\tau_\eta$ is of order unity (Wang & Maxey 1993, Fessler *et al.* 1994). In the presence of a wall, a mean drift of the particles sets up following the negative gradient of turbulence intensity (so-called turbophoresis) and causing a segregation of particles towards the wall (Caporaloni *et al.* 1975, Reeks 1983, Young & Leeming 1997, Guha 2008, Fouxon *et al.* 2018). The relevant parameter is usually considered the Stokes number $St^+ = \tau_p/\tau_\nu$, where τ_ν is the viscous time scale, with strong turbophoresis for $St^+ \sim 10-100$ (e.g., Marchioli & Soldati 2002, Sardina *et al.* 2012*a*, Bernardini 2014). Moreover, inertial particles were experimentally observed to arrange in long near-wall streaks (Kaftori *et al.* 1995*a*, Kaftori *et al.* 1995*b*, Niño & Garcia 1996), and numerical simulations demonstrated the role of coherent turbulent structures in determining such behavior (McLaughlin 1989; Zhang & Ahmadi 2000; Rouson & Eaton 2001; Marchioli & Soldati 2002; Soldati & Marchioli 2009; Sardina *et al.* 2012*a*; Nilsen *et al.* 2013; Richter & Sullivan 2013; Bernardini 2014). For typical Reynolds numbers used in laboratory and computational studies, the parameter ranges leading to both clustering and turbophoresis overlap. In fact, it has been argued that both phenomena represent different aspects of the same process (Sardina *et al.*, 2012*a*). Moreover, although rarely discussed in particle-laden turbulence studies, inelastic particle collisions may also contribute to near-wall particle accumulation (Hrenya & Sinclair, 1997). Other relevant experiments with similar scope includes the vertical pipe study of Varaksin *et al.* (2000) and the horizontal channel study of Wu *et al.* (2006).

Most of the studies mentioned above considered very dilute particles smaller than all scales of the flow – a regime in which the backreaction of the dispersed phase on the carrier fluid is usually deemed negligible. According to Elghobashi (1994), this condition (referred to as one-way coupling) is satisfied only for volume fractions $\phi_v \leq \mathcal{O}(10^{-6})$, while at higher loadings the particles do influence the turbulence (two-way

coupling). This classification, however, was merely proposed as a guideline for numerical approaches; the boundary between both regimes is problem-dependent and is affected by other physical parameters, including the particle-to-fluid density ratio, ρ_p/ρ_f. In wall-bounded turbulence, the flow dynamics and the local particle concentration also evolve with wall distance, especially in the presence of turbophoresis. Several numerical studies investigated the two-way coupled regime by direct numerical simulation (DNS) of wall turbulence, representing the particles as material points that exchange momentum with the fluid (see, for example, Pan & Banerjee 1996; Vreman 2007; Zhao *et al.* 2010; Dritselis & Vlachos 2011; Richter & Sullivan 2013; Richter & Sullivan 2014; Li *et al.* 2016; Wang & Richter 2018). The particles were found to affect the ejection-sweep cycle, the dynamics of streamwise vortices, the formation and strength of hairpin eddies, and in general to significantly modify the fluid Reynolds stresses. These modifications to the flow, in turn, altered the particle transport and thus their concentration and velocity statistics. By increasing the particle mass loading, $\phi_m = \phi_v \times \rho_p/\rho_f$, simulations also indicated the sizeable effect of inter-particle collision (four-way coupling), notably in reducing the near-wall concentration otherwise enhanced by turbophoresis (Li *et al.* 2001; Vreman 2007, Nasr *et al.* 2009, Kuerten & Vreman 2015). Recently, Capecelatro *et al.* (2018) demonstrated a dramatic change from shear-production-dominated to drag-production-dominated regimes when the mass loading increased from $\mathcal{O}(0.1)$ to $\mathcal{O}(10)$.

Despite the remarkable insight offered by the point-particle approach, this method presents well-known limitations, partly related to the point-wise forcing on the fluid computational grid (Eaton 2009, Balachandar & Eaton 2010). To overcome these shortcomings, advanced simulation strategies have been proposed (Capecelatro & Desjardins 2013, Gualtieri *et al.* 2015, Horwitz & Mani 2016, Ireland & Desjardins 2017, Balachandar *et al.* 2019). In general, our understanding of the physics of two-way coupled particle-laden turbulence is still incomplete, and as a result any simplified model may miss or misestimate significant aspects (Balachandar & Eaton, 2010). The availability of ever-increasing computational capabilities has allowed particle-resolved DNS to investigate relatively large numbers of particles in wall-bounded turbulent flows without the need of modeling the momentum exchange (Garcia-Villalba *et al.* 2012; Picano *et al.* 2015; Lin *et al.* 2017; Wang *et al.* 2017). Those studies, however, can typically deal with $\mathcal{O}(10^4)$ particles much larger than the viscous scales, as opposed to the millions

of sub-Kolmogorov particles usually present in point-particle simulations. The latter situation is most relevant to gas-solid mixtures.

In this scenario, the importance of well-controlled laboratory experiments is paramount to reach a predictive understanding of these regimes, and to inform and validate numerical models. Unfortunately, similar studies are rare in the literature and cover limited portions of the parameter space. Several past experiments considered particle-laden water flows with $\rho_p/\rho_f = \mathcal{O}(1)$ and particle diameters of several wall units (Kaftori *et al.* 1995*a*; Kaftori *et al.* 1995*b*; Niño & Garcia 1996; Kiger & Pan 2002; Righetti & Romano 2004; Rabencov *et al.* 2014; Oliveira *et al.* 2017; Shokri *et al.* 2017). These conditions are relevant to sediment transport and pipelines, but not to other important applications such as dust and particulate transport in air. For gas-solid suspensions, a non-exhaustive list of previous experiments and their relevant physical parameters is provided in table 1. Currently, the main reference is still represented by the vertical channel flow measurements by Eaton and co-workers. In particular, Fessler *et al.* (1994) and Kulick *et al.* (1994) provided seminal insight into preferential concentration and turbulence modulation for a variety of regimes. However, Benson *et al.* (2005) showed that their apparatus presented substantial wall roughness due to particle deposition on the walls, which according to Vreman (2015) partly explained the disagreement with simulations. Benson *et al.* (2005) repeated the measurements with a smooth test section, only focusing on the most inertial particles that did not display turbophoresis. Taniere *et al.* (1997) investigated a particle-laden boundary layer in a horizontal wind tunnel, focusing on particles with $St^+ > 270$. As in all horizontal flow configurations, the particle concentration profile was strongly impacted by gravity. Kussin & Sommerfeld (2002) measured particle motion and concentration as well as turbulence modulation in a horizontal channel flow with rough walls. Their particles were highly inertial and could not display turbophoresis or turbulence-induced clustering. Caraman *et al.* (2003) considered a vertical particle-laden pipe flow in a regime where turbophoresis is expected, and carried out a detailed analysis of the moments of the particle velocity. Still, comparison with simulations was hampered by the measurement station being downstream of the pipe exit, the lack of concentration profiles, and possible wall roughness (Vreman, 2007). Khalitov & Longmire (2003) conducted measurements in a vertical channel flow laden with glass spheres of various sizes, covering a range of Stokes numbers for which

turbophoresis is expected. They documented both particle-particle and gas-particle velocity correlations in the streamwise and spanwise directions, but not the concentration profiles. Hadinoto *et al.* (2005) considered a vertical pipe flow laden with glass beads that were too inertial to segregate at the wall. Li *et al.* (2012) imaged inertial particles at $St^+ \approx 100$ in a range of concentrations where two-way coupling effects are expected to be weak. Because their channel was horizontal and they only reported data near the bottom wall, possible turbophoresis was not distinguishable from gravitational settling.

Overall, there is a clear lack of laboratory observations of wall-bounded gas-solid flows in regimes where preferential concentration and turbophoresis are at play. In particular, little is known on the changes occurring when varying the loading across what is considered the boundary between one-way and two-way coupling. Liquid-solid flow studies cannot compensate for these deficiencies in the literature, as the momentum coupling is heavily affected by the density ratio. Importantly, concentration profiles are seldom reported, and therefore near-wall segregation (clearly evident in simulations) has not been fully documented. The seminal studies usually cited as experimental evidence of this phenomenon (e.g., Kaftori *et al.* 1995*a*; Kaftori *et al.* 1995*b*) were carried out in horizontal flumes where gravitational effects may be important. In order to bridge such knowledge gap, the present study experimentally investigates the transport of small solid particles in turbulent air flowing downward in a smooth-wall vertical channel. We focus on regimes (summarized in Table 2.1) for which significant clustering and turbophoresis are expected, and use planar imaging to analyze the particle behavior for different levels of mass loading.

2.1 Experimental setup

2.1.1 Experimental facility and parameters

Experiments are conducted in a vertical recirculating wind tunnel depicted in figure 2.1, featuring a 1.9 m long rectangular channel with a 0.24 m by 0.03 m cross-section. A 1.5 kW centrifugal blower (Atlantic Blowers) controlled by a frequency converter drives air downwards, and the flow rate is continuously monitored via a Venturi flowmeter. Before the air enters the channel, size-selected glass beads (Mo-Sci Corp.) with a density of 2500 kg/m^3 and diameter of 50 ± 6 µm (mean $\pm$ standard deviation measured by optical

	Re_τ	St^+	d^+	ϕ_v	ϕ_m	Configuration	Wall quality
Fessler *et al.* (1994)	630	27-150	0.8-3	5×10^{-5} -2×10^{-4}	0.03-1	Vertical channel	Rough
Kulick *et al.* (1994)	630	1500-2000	2.5-3	5×10^{-5} -2×10^{-4}	0.02-0.8	Vertical channel	Rough
Taniere *et al.* (1997)	1700	270-540	1.6-2.3	5×10^{-6}	0.006-0.01	Horizontal boundary layer	Smooth
Kussin & Sommerfeld (2002)	700-1300	570-7800	3-38	4×10^{-4}-4×10^{-3}	0.1-1	Horizontal channel	Rough
Caraman *et al.* (2003)	133	70	0.8	5×10^{-5}	0.11	Vertical pipe	Smooth
Khalitov & Longmire (2003)	238	50-3190	0.6-5.1	5×10^{-5}	0.1	Vertical channel	Smooth
Hadinoto *et al.* (2005)	253-544	730-2700	0.8-15	3×10^{-4}	0.7	Vertical pipe	Smooth
Benson *et al.* (2005)	630	1800	5	7×10^{-5}	0.15	Vertical channel	Smooth, rough
Li *et al.* (2012)	430	100	1.7	3×10^{-7} -5×10^{-6}	0.00025-0.005	Horizontal channel	Smooth
Present study	235-335	64-130	0.8-1.1	3×10^{-6} -5×10^{-5}	0.006-0.1	Vertical channel	Smooth

Table 2.1: A list of experimental studies addressing gas-solid wall-bounded flows. When not explicitly reported in the referenced papers, the parameters are calculated using information therein.

microscopy over $\mathcal{O}(10^4)$ samples) are injected into the flow through a precision screw-feeder (Vibra Screw Inc.). This corresponds to a ratio of channel width to particle diameter of $2h/d_p = 600$. A flow conditioning section consisting of four screens and three honeycombs is placed at the channel inlet to disperse the particles uniformly. The measurement station consists of a 0.3 m long, fully transparent acrylic section that follows a 1.6 m long development section. The latter has a through-flow time 25 - 40 times larger than the particle response time, depending on the air flow regime. Integration of the particle equation of motion with the Schiller and Neumann's correction (Clift *et al.*, 2005) indicates that the particles reach their terminal velocity in about half the time it takes them to reach the test section. The particles exhausted from the channel are collected in a 109-liter settling chamber, allowing for the run times needed to achieve well-converged statistics without particles being ingested into the blower. Electrostatic dissipative acrylic (SciCron Technologies) is used to build the optical test section, and the channel is provided with static discharge wires grounded to structural supports. This prevents the particles from accumulating upon impaction and building up unwanted roughness, an effect that has impacted past experiments (Benson *et al.*, 2005). This point is demonstrated and elaborated upon in Appendix A.1.

The fluid and particle parameters for the investigated cases are listed in table 2.2. Two flow rates are considered, associated with friction Reynolds numbers $Re_\tau = 235$ and 335, respectively. The particle Reynolds number, defined with the still-air terminal velocity of the particles $V_t = \tau_p g = 0.17$ m/s as a representative relative velocity with respect to the fluid, is $Re_p < 1$ (here g is the gravitational acceleration). Using the particle root mean square (rms) of the particle velocity fluctuations as a velocity scale leads to higher values, but still within $Re_p = \mathcal{O}(1)$, suggesting that particle wakes negligibly affect the flow. The Froude number, defined as the ratio of the centerline fluid velocity over the still-air settling velocity, satisfies the condition $Fr \gg 1$. It has been argued that this warrants a negligible influence of gravity (see the boundary layer study of Sardina *et al.* (2012*b*), where the freestream velocity is used to define Fr). However, this condition is not strictly applicable to the near-wall region where the fluid velocity vanishes. Moreover, for particle-turbulence interaction the relevant velocity scale is arguably the fluid rms fluctuation, which at the channel centerline is of the same order as the still-air settling velocity. Indeed, recent measurements in a

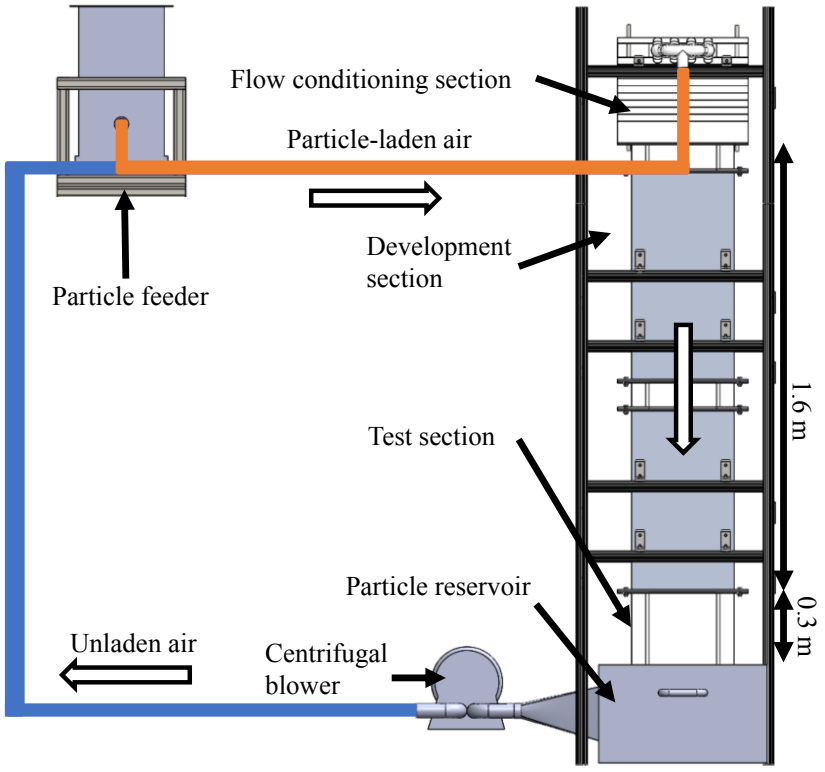

Figure 2.1: A schematic diagram of the particle-laden channel flow facility and its main elements.

vertical pipe from Oliveira *et al.* (2017) at $Fr > 10$ show large differences in particle behavior between downward and upward flow. Therefore, we will not generalize the present findings to other channel orientations, as gravity may play a significant role in this regime (as also discussed in §2.2).

The regimes $Re_\tau = 235$ and 335 are associated with different fluid timescales, resulting in two different Stokes number cases referred to as LoSt and HiSt, respectively. The change in Reynolds number, while not inconsequential, is expected to have a lesser impact over the considered range compared to the variation in St. The range of St^+ and St_η (the latter being defined with the Kolmogorov timescale at the channel centerline in the unladen flow) suggests significant turbophoresis and preferential concentration. For each Stokes number, two sets of measurements are carried out by changing the screw size in the particle feeder, resulting in volume fractions $\phi_v = 3\times10^{-6}$ (for a mass loading $\phi_m = 0.6\%$) and 5×10^{-5} ($\phi_m = 10\%$), referred to as LoVF and HiVF, respectively. These correspond to global concentrations $C_0 = 46$ and 880 particles/cm^3, respectively. The four-case matrix is summarized in table 2.3. The fluid phase parameters in table 2.2 are based on the unladen flow, characterized by particle image velocimetry (PIV) as described in the following. While the mass loading for the LoVF cases is not expected to produce sizeable changes in the fluid flow, in the HiVF cases the turbulence is likely to be impacted (Kulick *et al.*, 1994), and therefore the listed values of the flow properties should be regarded as estimates.

The coefficient of restitution, e for particle-wall collisions is measured in a separate experiment. e is defined as the ratio of the wall-normal particle velocity just after and just before the collision; details on the experimental measurements are elaborated upon in Appendix A.2. It is known that the value of e is dependent on the particle Reynolds number and Stokes number based on the particle velocity relative to the fluid (Gondret *et al.*, 2002). However, the terminal velocity happens to be on the order of the rms wall-normal velocity of the particles in the vicinity of the wall ($0.02U_c$ – $0.05U_c$, where U_c is the centerline velocity), as will be shown later. Thus, the quoted restitution coefficient is relevant to the particle-laden flow condition. Still, the actual collision velocity in the channel flow experiment is expected to have significant scatter; possible consequences of such variance are discussed in §4.

	LoSt	HiSt
Fluid phase parameters		
Fluid density, ρ_f (kg m^{-3})	1.2	
Kinematic viscosity, ν (m^2 s^{-1})	1.5×10^{-5}	
Channel half height, h (mm)	15	
Fluid centerline velocity, U_c (m s^{-1})	4.41	6.51
Fluid bulk velocity, U_{bulk} (m s^{-1})	3.01	4.66
Bulk Reynolds number, $Re_{bulk} = 2hU_{bulk}/\nu$	6020	9320
Fluid friction velocity, U_τ (m s^{-1})	0.235	0.335
Friction Reynolds number, $Re_\tau = hU_\tau/\nu$	235	335
Viscous lengthscale, λ_ν (µm)	64	45
Viscous timescale, τ_ν (ms)	0.27	0.13
Kolmogorov scale close to centerline, η_c (µm)	200	150
Kolmogorov timescale (at centerline), τ_η (ms)	2.6	1.5
Particle characteristics		
Density, ρ_p (kg m^{-3})	2500	
Mean diameter, d_p (µm)	50	
Mean diameter in wall units, d_p^+	0.78	1.1
Aerodynamic response time, τ_p (ms)	17	
Reynolds number, $Re_p = d_p\tau_p g/\nu$	0.6	
Froude number, $Fr = U_c/(\tau_p g)$	26	38
Kolmogorov-based Stokes number, St_η	6.7	11.5
Viscous Stokes number, St^+	64	130
Restitution coefficient, e	0.73	

Table 2.2: Fluid and particle parameters for the investigated cases. η_c is calculated using the relation $\eta_c = \lambda_\nu(\kappa Re_\tau)^{1/4}$ (Pope, 2000).

Parameters	$St^+ = 64$	$St^+ = 130$
$\phi_v = 3 \times 10^{-6}$	LoSt-LoVF	HiSt-LoVF
$\phi_v = 5 \times 10^{-5}$	LoSt-HiVF	HiSt-HiVF

Table 2.3: Cases studied in this experiment and respective notation.

2.1.2 Measurement methods

The imaging system consists of a double-pulsed Nd:YAG laser (30 mJ/pulse, New Wave Instruments) and a 1376 $\times$ 1040 pixel CCD camera (Sensicam, PCO Instruments) operated at 5 Hz and synchronized to the laser via a delay generator (BNC-5500, Berkeley Nucleonics). Planar measurements are obtained by shaping the laser beam into a sheet via an optical module combining cylindrical and spherical lenses. For all cases, the measurement locations include a wall-normal plane that contains the channel centerline. We denote with x, y, and z the streamwise, wall-normal, and spanwise directions, the channel walls being located at $y = 0$ and $y = 2h$. For the HiVF cases, several wall-parallel planes are also imaged and compared, one at the centerline ($y = h$) and one in the near-wall region ($y = 0.11h$), see figure 2.2a. An additional wall-parallel plane (not shown in figure 2.2a) is imaged at $y = 0.2h$ for comparisons with wall-normal profiles. Spatial calibration and plane location are performed by imaging a target plate mounted on a micrometric traverse, inserted in the channel from the opening at the outflow end. The laser sheet thickness is evaluated using a photodiode (Thorlabs Inc.) coupled with a neutral density filter (CW Optics) and mounted on a traverse. The full width at half maximum is approximately 1.1 mm (Figure 2.2b).

The unladen (single-phase) case is characterized using 2C-2D PIV along the wall-normal symmetry plane. The flow is seeded with DEHS oil atomized by a Laskin nozzle into 1 - 2 µm droplets that faithfully follow the flow, their viscous Stokes number being $\mathcal{O}(10^{-2})$. For those measurements, the CCD camera mounts a 200-mm Micro-Nikkor lens at f/5.6 to obtain a 13.3 $\times$ 10.1 mm^2 field of view. The full channel height is covered by stitching together four slightly overlapping windows. The pulse delay is set to 10 µs and 15 µs for the higher and lower flow rate, respectively, keeping the typical tracer displacement to about 8 pixels. Image pairs are processed via a multi-pass cross-correlation algorithm, with a final interrogation window of 32 $\times$ 32 pixels and 50% overlap. Flow statistics are obtained ensemble-averaging over 2000 uncorrelated realizations as well as in the homogeneous streamwise direction. The fully developed nature of the flow at the measurement station is confirmed by comparing profiles across the imaging window, with no appreciable changes for statistics up to second order.

In the particle-laden cases, the inertial particle position and velocity are characterized by Particle Tracking Velocimetry (PTV) using an in-house code developed based

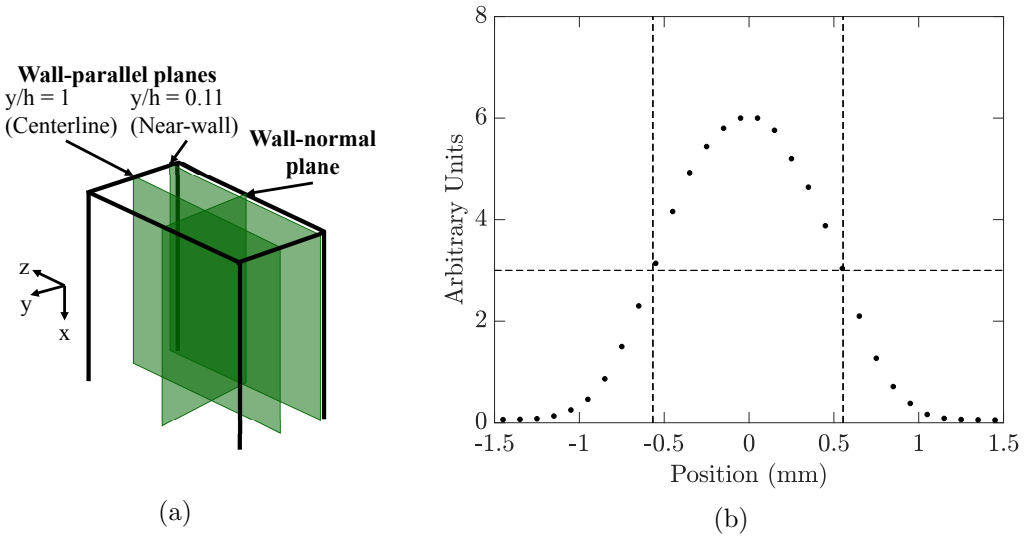

Figure 2.2: (a) Main imaging planes investigated in the present study. (b) Light intensity profile as measured by a photodiode to estimate the laser sheet thickness. The dashed lines mark the full width at half maximum.

on the cross-correlation methods described in Hassan *et al.* (1992) and Ohmi & Li (2000). Further details on the algorithm can be found in Petersen *et al.* (2019). For the measurements along the wall-normal plane, the CCD camera mounts a 105-mm Micro-Nikkor lens at f/16, providing an imaging magnification of 36.1 px/mm for a 34.3 $\times$ 25.9 mm^2 field of view encompassing the full channel height. The particle-per-pixel density is 4.0×10^{-5} for the LoVF cases and 6.9×10^{-4} for the HiVF cases. Along the wall-parallel planes, an aperture of f/4 is used, providing an imaging magnification of 19.0 px/mm for a 55 $\times$ 70 mm^2 window at the spanwise center of the channel. The particle-per-pixel density is 1.8×10^{-3} for the centerplane and 3.9×10^{-3} for the near-wall plane.The particle images are about 3 pixels, whose centroid is retrieved with an accuracy of approximately ± 0.1 pixels, as confirmed by tests on synthetic images. The pulse delay ranges between 70 µs and 100 µs depending on the cases and imaging locations, with typical particle displacements of 15 to 20 pixels. A pre-processing thresholding routine is applied to eliminate out-of-focus particles. The in-focus particles are tracked between image pairs using the relaxation method described by Baek & Lee (1996). The local concentration is measured along the wall-normal plane by counting the number of particle centroids detected. This approach was used for inertial particles

in air (Yang & Shy 2005; Sahu *et al.* 2014; Sahu *et al.* 2016) and in water (Kiger & Pan, 2002). Knowles & Kiger (2012) showed that, in water, laser-based measurements of particle concentration can be misestimated by as much as 30%; however, they considered volume fractions one order of magnitude higher than the present case. Even at the higher loading investigated here, the average interparticle distance is ~ 1 mm, which is much larger than the particle image. Due to clustering, the instantaneous local concentration can be higher, and some particles may go undetected. However, intense clustering usually pertains to a limited fraction of the particle set (Baker *et al.*, 2017); here the regions where such bias may be more significant are near the wall, due to turbophoresis. Still, the volume fraction evaluated from the particle count along the wall-normal plane (assuming a 1.1 mm thick imaging volume) agrees within 12 - 15% with the value obtained by weighing the particles accumulated in the settling chamber during a given run time, lending confidence to the approach. Concentration and velocity statistics are based on ensemble-averaging over 2000 uncorrelated realizations (collected over four runs of 500 realizations each) as well as over the streamwise direction. The streamwise homogeneity of the particle statistics is discussed in §2.2.2. All statistics are verified to be steady-state during each run, with excellent repeatability in each run (within variations of the order of the statistical uncertainty). It is noted that simultaneous fluid-phase measurements are not acquired in this experiment. This is due to the relatively high image concentration of the inertial particles, especially near the wall, reducing the signal from fluid tracers. The feasibility of obtaining simultaneous fluid measurements are discussed in §4.

2.2 Wall-normal measurements

2.2.1 Particle concentration

Figure 2.3 displays the mean profiles of normalized particle concentration C/C_0 for the four particle-laden cases. Here and in the following wall-normal profile plots, data points in the profiles are plotted at the y/h location at the center of the respective wall-normal bin, each bin having a width of 0.25mm (about 9 pixels). Data points measured for the HiVF cases along wall-parallel planes are also shown and found to agree closely to the wall-normal imaging results. Both LoVF and HiVF cases display a

peak of concentration in the near-wall region, confirming that turbophoresis is active in the present regime. However, in the more dilute cases the peak is mild, and away from the wall the concentration gradually increases towards another local maximum at the centerline. On the other hand, the higher-loading cases display a much stronger peak of concentration near the wall, and the profile is essentially flat in the core region. The peaks appear to be at a finite standoff distance from the wall, which is however hard to quantify precisely.

As mentioned in the Introduction, previous measurements of near-wall segregation in similar regimes are lacking, and a comparison with past numerical simulations is in order. We refer to point-particle DNS studies, which are free from issues associated to turbulence modeling. Among those, several one-way-coupled simulations yielded near-wall concentration peaks two or more orders of magnitude above the channel mean, and mostly contained within the viscous sub-layer (Marchioli & Soldati 2002; Marchioli *et al.* 2008; Sardina *et al.* 2012*a*; Bernardini 2014). Those results, while insightful, are influenced by the fact that point-particles can amass to arbitrary densities. In two-way-coupled simulations, the momentum back-reaction from the particles reduced the near-wall segregation, as did the inter-particle collisions, see Li *et al.* (2001), Vreman (2007); Nasr *et al.* (2009). These authors did show concentrations reaching a minimum adjacent to the near-wall peak and increasing up to a centerline maximum, similarly to our LoVF profiles. However, they found that such reduction of the near-wall peak (and the simultaneous appearance of a centerline maximum) occurred for increasing mass loading, in contrast with the present results. On the other hand, the concentration profiles we observe for LoVF are consistent with the argument of Young & Leeming (1997) that turbophoresis is driven by the gradient of fluid V_{rms}. The concentration is maximized in correspondence to the concentration minimum, decays steeply towards the wall and more mildly towards the centerline, following approximately the same trend as the wall-normal gradient of V_{rms}. We remark that the centerline concentration maximum was observed in several, but not all, one-way-coupled simulations, and was found to depend on the flow orientation: for example, Nilsen *et al.* (2013) found it for downward and no-gravity flow, but not for upward flow.

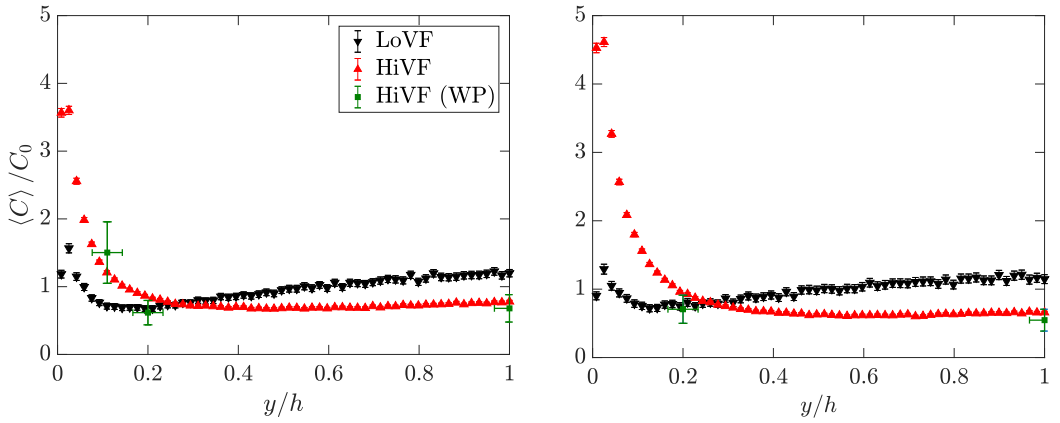

Figure 2.3: Mean particle concentration profiles normalized by the global concentration for (a) LoSt cases and (b) HiSt cases. Here and in the following plots, WP indicates data points from wall-parallel measurements, with the horizontal error bars indicating uncertainty on laser sheet position.

2.2.2 Particle mean and r.m.s. profiles

Figure 2.4 displays mean velocity profiles compared to the unladen air velocity. The data is presented both in outer (a, b) and inner (c, d) units, normalizing by the unladen velocity scales. In the viscous and buffer layer, the particles travel faster than the unladen air. This is a consequence of fast-moving particles retaining part of their momentum when transported towards the wall by turbulent fluctuations, without being constrained by the no-slip boundary condition. Such behavior was already highlighted by Kulick *et al.* (1994) and in several later experimental and numerical studies (e.g., Taniere *et al.* 1997; Rouson & Eaton 2001; Vreman 2007; Li *et al.* 2012). Righetti & Romano (2004) explicitly commented on an effective slip boundary condition for the particle field. Further away from the wall, in the LoVF cases the particles travel at approximately the same speed as the unladen air, while in the HiVF cases they lag in the logarithmic and buffer layers, recovering to the unladen air velocity in the channel core. A decrease of mean velocity with increasing mass loading was also reported by Kulick *et al.* (1994), although for higher St^+. In that case the lag was visible up to the centerline, but this was likely due to the wall roughness (Benson *et al.*, 2005). In general, we observe less flat velocity profiles than in previous experiments, see e.g.

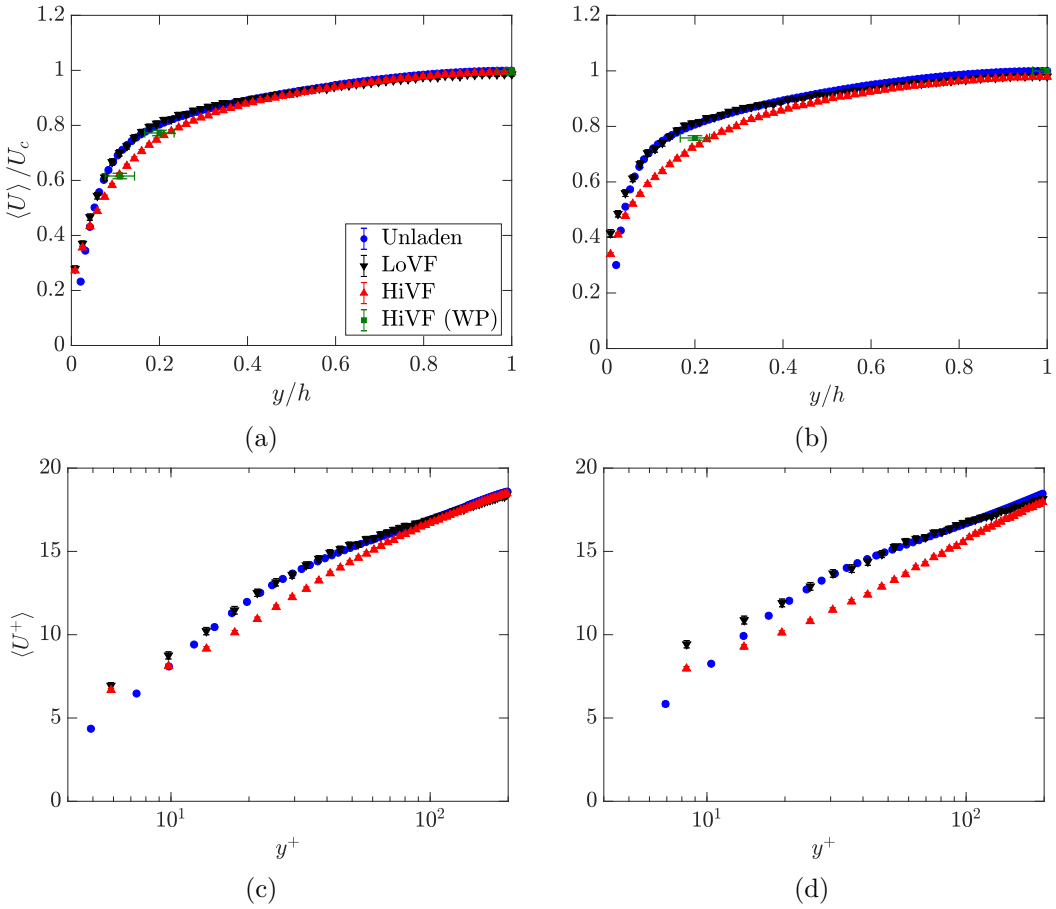

Figure 2.4: Profiles of mean streamwise particle velocity for (a, c) LoSt and (b, d) HiSt cases, normalized in outer units (top panels) and inner units (bottom panels). Unladen fluid profiles plotted for comparsion.

Kulick *et al.* (1994); Paris (2001); Caraman *et al.* (2003); Benson *et al.* (2005). Vreman (2015) argued that those were again influenced by some wall roughness that enhanced the wall-normal particle velocity fluctuations and in turn flattened the mean velocity profiles.

Figure 2.5 displays profiles of mean wall-normal particle velocity. In a fully developed state, this should be identically zero. This is the case (within error bounds) for the unladen fluid, while the particles do show some residual drift towards the wall. This is likely caused by turbophoresis; the effect is exemplified in the LoVF case where the peak at $y/h \sim 0.2$ approximately corresponds to the maximum of unladen fluid V_{rms} and to

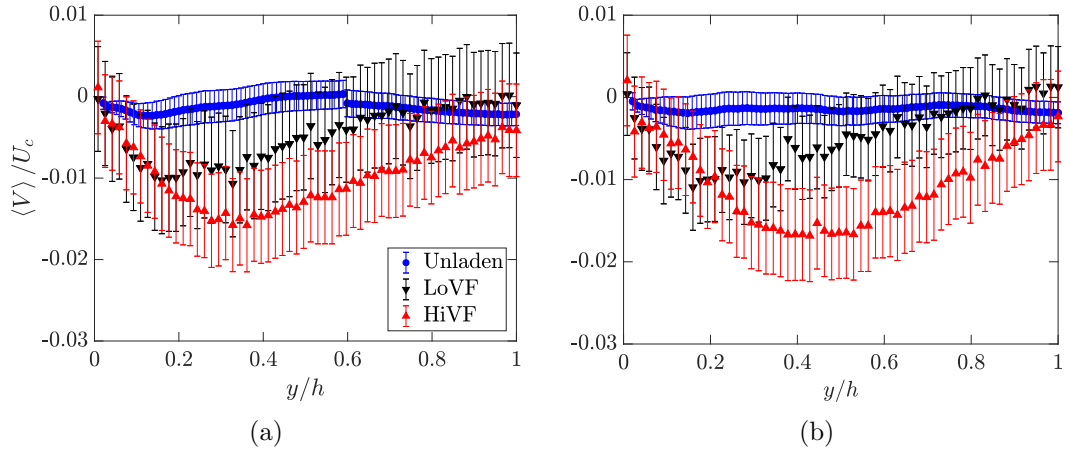

Figure 2.5: Profiles of mean wall-normal particle velocity for (a) LoSt and (b) HiSt cases. Unladen fluid profiles plotted for comparison.

the minimum of particle concentration, consistent with the theory of Young & Leeming (1997) (see also Capecelatro *et al.* 2016). Numerical simulations at similar St^+ indicated that the turbophoretic drift continues to modify the particle field during $\mathcal{O}(10^4)$ viscous time scales, which over the considered range of Re_τ corresponds to $\mathcal{O}(10^3)$ channel heights (Marchioli *et al.* 2008; Sardina *et al.* 2012*a*; Bernardini 2014). While these estimates are influenced by the one-way coupled nature of the modeling, they clearly indicate that the particle field requires a much greater development length than the sole hydrodynamics. However, we also remark that the observed wall-normal mean velocities are about 1% of the streamwise velocity, and smaller than the rms fluctuation in the same direction (reported below). Moreover, all statistics show no visible trend over the imaging windows (about $1.7h$ and $3.7h$ in streamwise direction for the wall-normal and wall-parallel measurements, respectively). Thus, also considering that the particles are expected to have reached terminal velocity much before entering the imaging section, the influence of the partial streamwise development is unlikely to qualitatively impact the reported trends.

The rms streamwise fluctuations of the particle velocity is plotted in figure 2.6. The LoVF cases display profiles similar to the unladen flow in the channel core, and significantly more intense fluctuations (up to 20% higher than the fluid) in the near-wall

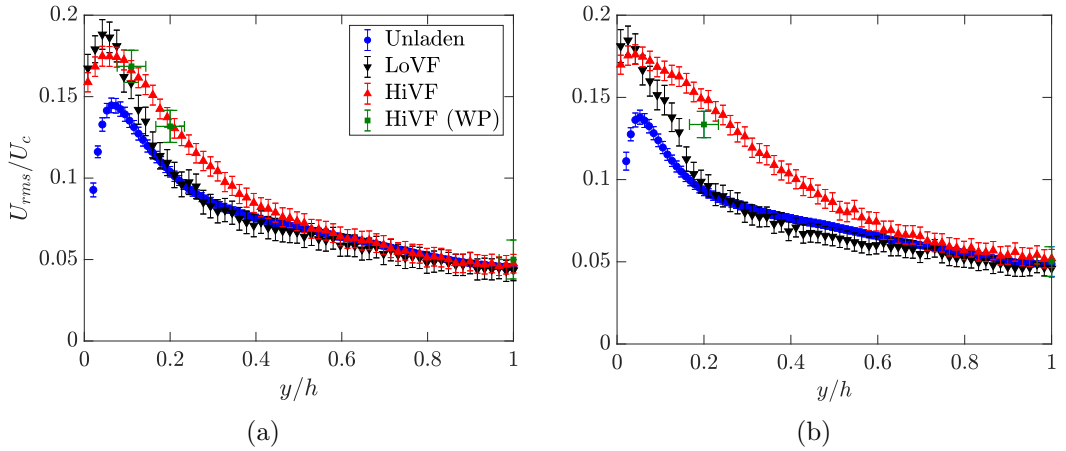

Figure 2.6: Profiles of rms streamwise particle velocity for (a) LoSt and (b) HiSt cases. Unladen fluid profiles plotted for comparison.

region, with little differences between LoSt and HiSt. Previous studies have found particles with velocity fluctuations stronger than the carrier fluid in several configurations, including particle-laden jets and homogeneous turbulence (e.g., Hardalupas *et al.* 1989; Petersen *et al.* 2019). Specifically in channel flows, the observed trend agrees with one-way coupled simulations as reported by Marchioli *et al.* (2008) and Nasr *et al.* (2009) for lower but still turbophoretic Stokes numbers. Following Taniere *et al.* (1997), the increase in rms velocities may be interpreted as a consequence of the spread in momentum of particles with different history: the ones arriving to a near-wall interrogation window from more distant locations retain some of their relatively high speed due to inertia; while those coming from a rebound on the wall have lost some of their kinetic energy in the collision. Remarkably, the HiVF cases show a significant increase of particle velocity fluctuations even at $y/h \sim 0.4$, which is even more dramatic for HiSt. The near-wall peak is about the same as in LoVF, but the cross-section-average rms fluctuation is substantially augmented for the higher loading. This is in contrast with past two-way and four-way coupled point-particle DNS: considering mass loadings higher than but comparable to the current HiVF cases, Li *et al.* (2001), Vreman (2007), and Nasr *et al.* (2009) found a decrease in streamwise rms fluctuations (although the trend with increasing ϕ_v reported by Vreman was locally not monotonic at high loadings).

Figure 2.7 shows profiles of the wall-normal rms fluctuations of the particle velocities.

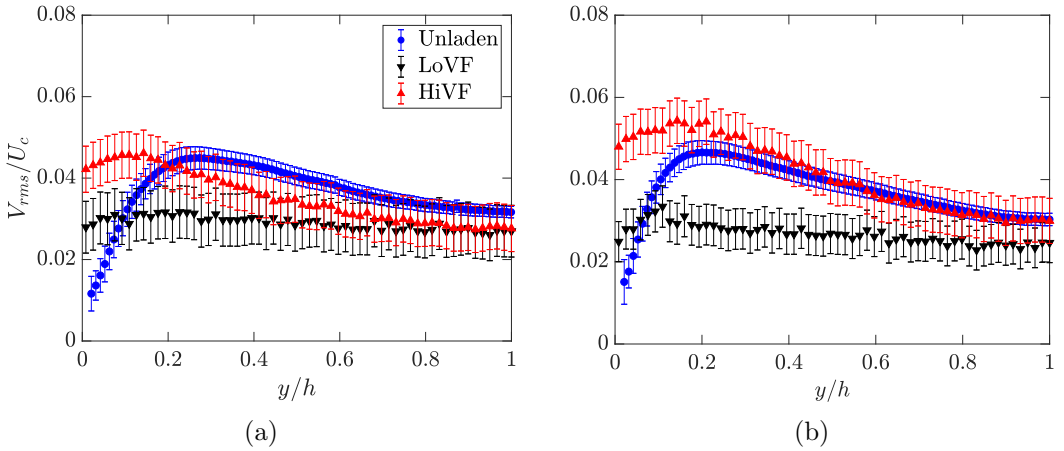

Figure 2.7: Profiles of rms wall-normal particle velocity for (a) LoSt and (b) HiSt cases. Unladen fluid profiles plotted for comparison.

For LoVF, the particle V_{rms} is lower than the unladen fluid V_{rms} in the channel core, but it remains fairly flat across the channel and largely exceeds the unladen fluid levels for $y/h < 0.1$. The effect of St^+ in the considered range is minor. Moreover, while the fluctuation level decreases approaching the wall, it does not appear to vanish. This is in contrast with one-way coupled simulations where the particle V_{rms} is consistently lower than the fluid V_{rms} (thus vanishing at the wall, Marchioli *et al.* 2008), but is consistent with previous experiments with particles of similar St^+ (Li *et al.*, 2012). The approximately even redistribution of the lateral kinetic energy across the channel cross-section may partly be due to particle inertia, and partly to collisions with the wall (inter-particle collision being relatively unlikely at the lower volume fraction). At HiVF, V_{rms} increases more significantly approaching the wall, and the tendency is stronger for HiSt. This behavior is similar as for U_{rms}, and indicates again that the particle-fluid dynamics has been altered: by the modification of the underlying turbulent flow and/or by the increase in particle-particle/wall-particle collisions.

2.2.3 Further analysis of particle velocities

The wall-normal velocity is tightly related to the particle flux towards the wall, which eventually may lead to particle deposition. The flux can be expressed as the rate of particles per unit area crossing a control plane, $J = (dN/dt)/A_s$, where N is the number

of particles on either side of the plane, t indicates time and A_s is the surface area of the control plane. Normalizing by the global concentration C_0 yields a characteristic velocity $k = J/C_0$; taking the control plane at the wall gives the commonly used deposition velocity k_d, which in turn can be made non-dimensional with a velocity scale usually taken as the friction velocity, $k_d^+ = k_d/u_\tau$ (Liu & Agarwal 1974; Young & Leeming 1997; Bernardini 2014). Here the spanwise direction is assumed homogeneous and the above definitions are adapted to the two-dimensional measurements: the concentration is areal rather than volumic, and wall-parallel lines act as the control planes. Figure 2.8 shows the non-dimensional characteristic velocity k^+ as a function of wall distance for the LoSt case (which shows similar trends to the HiSt case). We plot separately the fluxes towards and away from the wall. Because there is no net particle deposition, at the wall both fluxes are in balance (within experimental scatter). Wall collision cannot be directly detected with the present setup, but the absolute value of k^+ at the measurement location closest to the wall (i.e., control plane at $y^+ \sim 4$ for the LoSt case) is taken as a proxy of k_d^+. For the LoVF case, one retrieves $k_d^+ = \mathcal{O}(0.1)$, in agreement with previous observations (see, e.g., the collection of data in Young & Leeming 1997). On the other hand, the HiVF case shows a sharp increase of flux in the inner layer and a much higher deposition velocity $k_d^+ = \mathcal{O}(1)$. This is consistent with the high V_{rms} levels reported above, and indicates that the change in particle transport properties at high loading greatly impact wall collision and (for a non-reflective wall) deposition.

In figure 2.9 we present profiles of the cross-correlation between the particle streamwise and wall-normal fluctuations, referred to as particle Reynolds shear stress, along with the unladen fluid counterpart. For LoVF, these are found to follow the trend of the unladen fluid in the channel core up to about $y/h = 0.2$, but visibly exceed those values in the near wall region. A similar behavior was reported in the vertical pipe flow of Caraman *et al.* (2003), whereas in horizontal flow studies such as Li *et al.* (2012) particle Reynolds stresses were above/below the fluid levels in the core/near-wall region. These discrepancies stress once more the consequential differences between configurations, in particular as it pertains the gravity force direction. The HiVF cases show again an earlier departure from the unladen fluid statistics and a more dramatic increase in correlation magnitude.

To explore this dynamic further, we perform a quadrant analysis in the (u, v) plane.

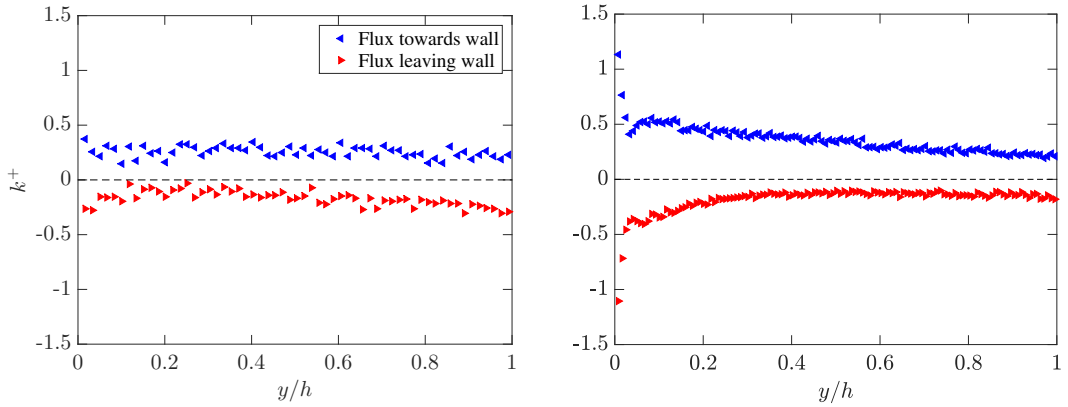

Figure 2.8: Profiles of characteristic flux velocity k^+ based on fluxes towards and away from the wall, for (a) LoSt-LoVF and (b) LoSt-HiVF cases.

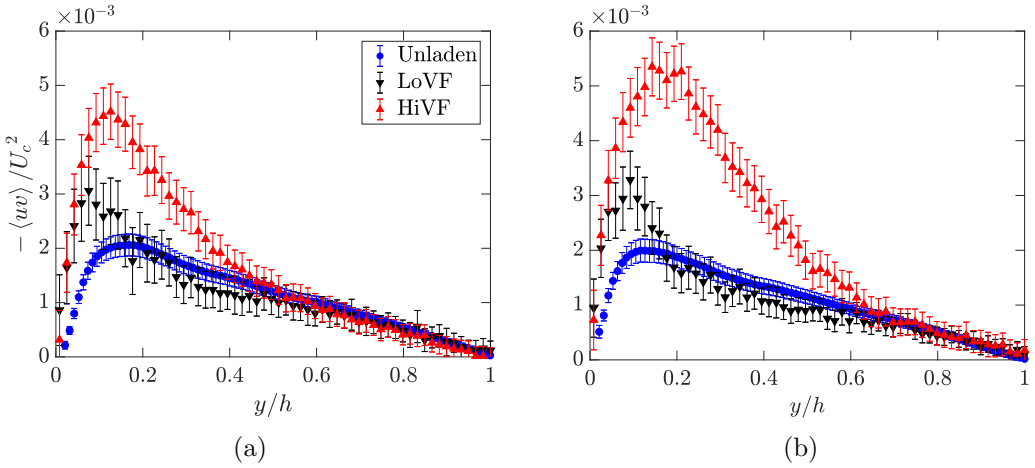

Figure 2.9: Profiles of particle Reynolds shear stress for (a) LoSt and (b) HiSt cases. Unladen fluid profiles plotted for comparison.

Following classic notation utilized in wall turbulence studies, we label events belonging to the four quadrants as Q1 ($u>, v>0$), Q2 ($u<0, v>0$), Q3 ($u<0, v<0$), and Q4 ($u>, v<0$). We report on the LoSt cases, which behave similarly to the HiSt. Figure 2.10a shows, for reference, the contributions to the Reynolds stresses for the unladen fluid velocity at the same Reynolds number. This highlights the predominance of the Q2 and Q4 events which contribute to positive turbulence production, with Q4 prevailing on Q2 for $y/h < 0.06$ (or $y^+ < 15$), and vice versa further from the wall (Kim *et al.*, 1987). The particles (figure 2.10b,c) follow a similar trend, but with noteworthy differences. The prevalence of Q4 events in the near-wall region is much more pronounced, which is consistent with sweeps being crucial in the process of trapping the particles near the wall (Marchioli & Soldati, 2002). This is in stark contrast with the result of Li *et al.* (2012): they found overwhelmingly higher probability of Q2 events near the floor of their horizontal channel, where gravity caused much more frequent wall rebounds. At HiVF, both Q2 and Q4 contributions are similarly enhanced, but the cross-over point is farther from the wall compared to LoVF: the region where particles are swept towards the wall is wider, which corresponds to a more intense turbophoretic drift, a stronger near-wall peak of concentration, and a depletion of the centerline peak (see figure 2.3). For this case also Q3 is remarkably large near the wall, probably a consequence of particles colliding with each other and with the wall (Righetti & Romano, 2004).

For completeness, we present in figure 2.11 the rms of the particle spanwise velocity fluctuations from the wall-parallel measurements. At $y/h = 0.2$ and 1, the values are consistent with the fluid W_{rms} in the DNS of Moser *et al.* (1999) for $Re_\tau = 180$ and 395 at the same wall-normal locations, which are expected to be close to the unladen fluid values in the present case. The sharp increase at $y/h = 0.11$ for the LoSt-HiVF case indicates again an augmented fluctuation of the particle velocity near the wall with higher loading, at odds with previous two-way coupled simulations (Li *et al.* 2001; Nasr *et al.* 2009).

We conclude this section considering the skewness of the streamwise velocity fluctuations for the inertial particles, in comparison with the unladen fluid. Figure 2.12 shows data for the LoSt cases (HiSt cases displaying the same trend). To improve convergence, the particle profiles are binned in four regions, each displaying fairly homogeneous behavior and roughly corresponding to the inner layer ($y^+ < 10$), buffer layer

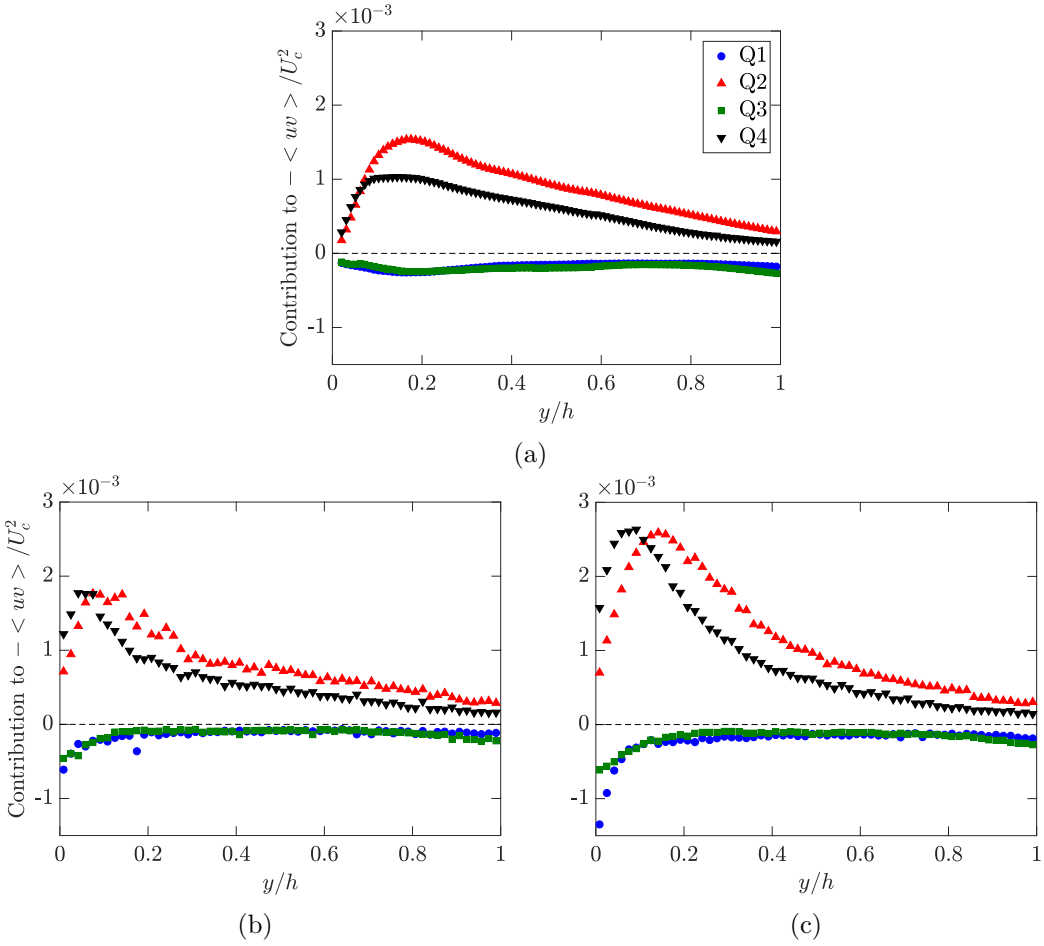

Figure 2.10: Contribution of each quadrant of the (u, v) plane to the Reynolds shear stresses for (a) unladen fluid and (b) inertial particles for the LoSt-LoVF case and (c) LoSt-HiVF case.

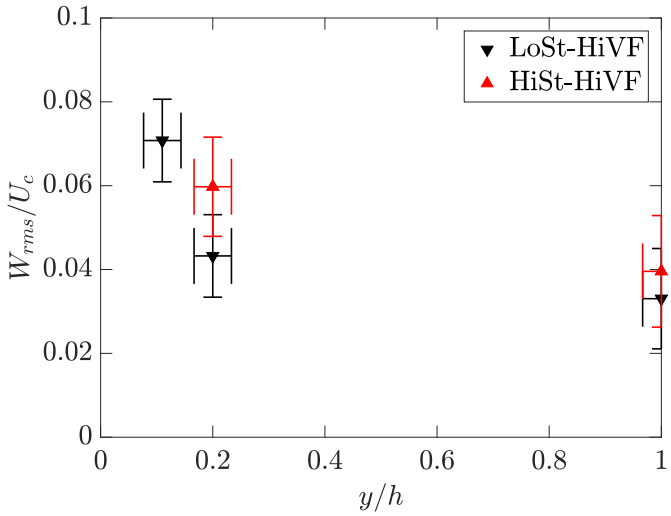

Figure 2.11: Profile of rms spanwise particle velocity for LoSt-HiVF and HiSt-HiVF cases, obtained from the wall-parallel measurements expanded in §2.3.

($10 < y^+ < 30$), log layer ($30 < y^+ < 100$), and outer layer ($100 < y^+ < 235$). The unladen fluid streamwise fluctuations have positive skewness in the inner layer and part of the buffer layer, and negative elsewhere as expected (see e.g. Kim *et al.* 1987). On the other hand, the inertial particles show positive skewness across the channel height, irrespective of volume fraction. Considering the flow is in the direction of gravity, this may be due to a tendency of the particles in the channel core to favor the downward side of turbulent eddies, as it is known to happen in homogeneous turbulence (Wang & Maxey, 1993). We will return to this point in §2.3.2.

2.3 Wall-parallel measurements

We leverage the wall-parallel plane imaging to investigate the instantaneous spatial organization of the particles and their velocity distribution. Streamwise-spanwise planes are especially suitable for this analysis, as they extend along homogeneous directions and thus allow for the efficient calculation of statistics that are unbiased by spatial gradients. We employ two-point quantities such as radial distribution functions (RDFs) and two-point Eulerian velocity correlations of streamwise velocity fluctuations, as well as tessellation techniques such as Voronoi diagrams and box-counting. We do not report

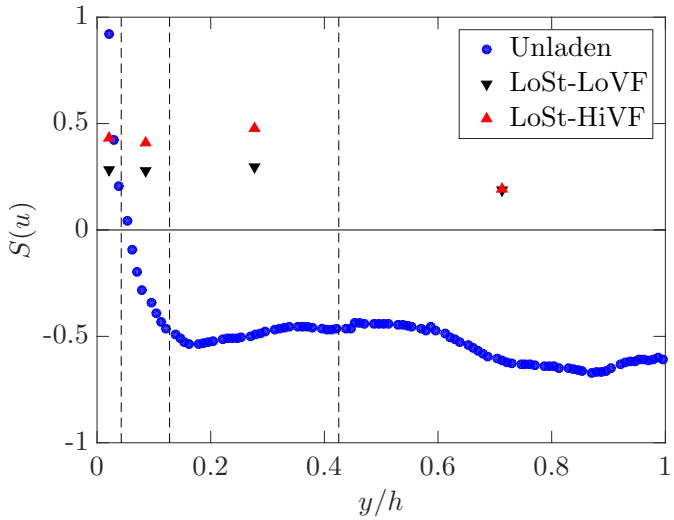

Figure 2.12: Profile of the skewness of the particle streamwise velocity fluctuations in the LoSt-LoVF and LoSt-HiVF cases. Unladen fluid profiles plotted for comparison. The vertical dashed lines demarcate the regions over which the particle-laden data are averaged.

here on the spanwise velocity fluctuation correlations in the wall-parallel planes, as the spanwise displacements are not sufficiently larger than the uncertainty to yield accurate second-order statistics. These tools are used to investigate the wall-parallel plane at the centerline (centerplane) and the near-wall plane at $y/h = 0.11$. The analysis is carried out only for the HiVF cases, for which the number of particles is sufficient to provide sufficient spatial resolution and statistical accuracy. While this does not allow direct assessment of the volume fraction effect on such quantities, it does bring useful insight to the particle spatial distribution in the regime for which the interphase coupling is expected to be more complex.

2.3.1 Two-point statistics

We use radial distribution functions (RDFs) to describe the scale-by-scale concentration in the area surrounding a generic particle, compared to a uniform distribution (Sundaram & Collins, 1997). For 2D distributions such as those obtained by planar imaging, this can be written as (see, e.g., Wood *et al.* 2005):

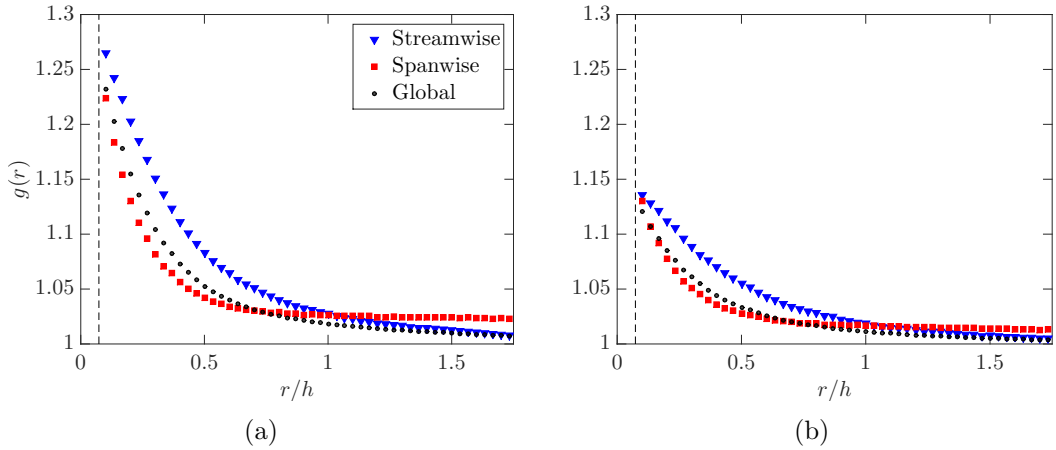

Figure 2.13: Global and directional RDFs along the center-plane for (a) LoSt-HiVF and (b) HiSt-HiVF. The vertical dashed line indicates the laser sheet thickness.

$$g(r) = \frac{\langle N_r/A_r \rangle}{N/A}, \tag{2.1}$$

where N_r represents the number of particles within an annulus of radius r and area A_r, N is the total number of particles within the planar domain of area A. In presence of clustering, the RDF is expected to increase above 1 for decreasing r, and the range over which it remains significantly greater than unity approximately indicates the length scale over which clustering occurs. We compute RDFs by binning particle pairs in equally spaced annuli of radial width 0.5 mm ($0.03h$). An edge-correction strategy is needed for particles near the image boundaries. Omitting annuli that cross the image boundary limits the maximum separation to the radius of the domain-inscribed circle, reducing the number of usable particle pairs with increasing separations and thus affecting the large-scale characterization. We instead mirror the particle field across the image boundaries, so that the same number of annuli is used for each particle location. The maximum separation then equals the full image size, introducing only small biases near the boundaries (Salazar *et al.* 2008; de Jong *et al.* 2010; Petersen *et al.* 2019). To avoid projection biases at separations below the illuminated volume thickness (Holtzer & Collins, 2002), we only present $g(r)$ for $r > 1.1$ mm.

This "global" (i.e., omnidirectional) definition of RDF does not discriminate between different directions of the separation r. We also calculate "directional" RDFs, in which

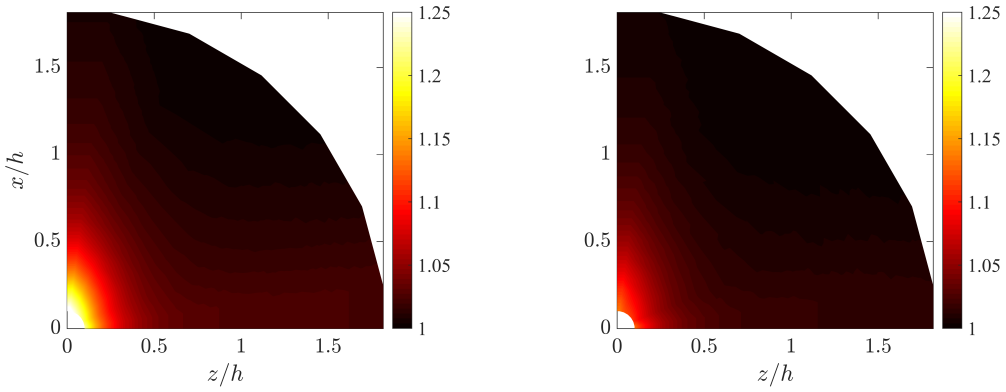

Figure 2.14: Angular distribution functions (ADFs) along the center-plane for (a) LoSt-HiVF and (b) HiSt-HiVF.

the separations are oriented either streamwise or spanwise. This allows us to characterize the streamwise and spanwise extent of the highly concentrated particle structures. Additionally, we calculate the angular distribution function (ADF, see Gualtieri *et al.* 2009, Nicolai *et al.* 2013) which is obtained by binning the planar domain in polar coordinates (r, θ):

$$g(r,\theta) = \langle \frac{N_{r,\theta}(r,\theta)}{A_{r,\theta}(r,\theta)} \rangle \, / \, (\frac{N}{A}), \tag{2.2}$$

Here $\theta = 0$ and $\theta = 90$ degrees correspond to spanwise and streamwise directions, respectively. We use equally spaced annuli of radial width 0.03 h and divide each of them in 24 azimuthal sectors of area A (in which we count N particles). Streamwise and spanwise homogeneity are leveraged to limit the analysis to one quarter of the (r, θ) circle.

We first consider the wall-parallel plane at the center-plane. Figure 2.13 shows RDFs (global and directional) for LoSt and HiSt cases. The global RDFs indicate that clustering extends over similar length scales for both cases, but it is significantly more pronounced for LoSt. This is not unexpected since the latter is closer to the condition $St_\eta \sim 1$, which was shown to produce more intense clustering in homogeneous turbulence (Wang & Maxey 1993; Wood *et al.* 2005) and at the center-plane of channel flows (Fessler

et al., 1994). The directional RDFs also indicate that the clusters are more elongated in streamwise than in spanwise direction. The spanwise RDF remains somewhat above unity throughout the field, indicating that some structure in the particle distribution persists over large scales in that direction. This general picture is confirmed by the ADFs in figure 2.14, which also show how the particle field becomes more quickly decorrelated for separations in direction $\theta \sim 45$ degrees.

We next consider the two-point Eulerian velocity correlations, which provide information on the level of spatial coherence of the particle motion. We follow Fevrier *et al.* (2005), who in turn borrowed the formalism proposed by Sundaram & Collins (1999), and write the general expression for the correlation between the streamwise velocity fluctuations of particles m and n, normalized by their velocity variance:

$$R_{uu}(r) = \frac{\langle u^{(m)} u^{(n)} \,|\, \boldsymbol{x} = \boldsymbol{x_p^{(m)}}; \boldsymbol{x} + \boldsymbol{r} = \boldsymbol{x_p^{(n)}} \rangle}{\langle u^2 \rangle}, \tag{2.3}$$

Here $\boldsymbol{x}$ is the location within the measurement plane, $\boldsymbol{x_p^{(i)}}$ is the position of the generic $\boldsymbol{i}$th particle, $\boldsymbol{r}$ is the separation vector connecting the particle pair (m,n), and angle brackets represent ensemble-averaging over all particle pairs. Boldface denotes vectorial quantities. The calculation is implemented with the same processing routine used for the RDFs and ADFs (which contains the information on the particle pair mutual positions). Again, we calculate both "directional" correlations, in which the separation vector is either streamwise or spanwise, and polar correlations, which span the (r, θ) space.

Figure 2.15 displays the directional velocity correlations evaluated at the center-plane. For both LoSt and HiSt cases, the normalized values do not approach unity for vanishingly small separations. (This is also confirmed by data points for separations smaller than the laser sheet thickness, not shown because inherently less accurate.) This indicates that a significant portion of the particle velocity is not spatially correlated. This is in line with the mesoscopic Eulerian formalism introduced by Fevrier *et al.* (2005), according to which inertial particle motion consists of two components: a contribution from the underlying turbulent velocity field, spatially correlated; and a quasi-Brownian velocity distribution, random and as such spatially uncorrelated. The latter is rooted in the particle inertia, in particular the memory of interactions with

distant eddies. This results in different velocities of arbitrarily close particles, possibly enhancing collision rates, and is consistent with the concepts of caustics and sling effect (Wilkinson & Mehlig 2005; Bewley *et al.* 2013; Reeks 2014). The gap between unity and R_{uu} for vanishing separations is a measure of the fraction of random uncorrelated motion (Fevrier *et al.* 2005; Vance *et al.* 2006). This framework has been employed in numerous theoretical and numerical studies to analyze and model different particle-laden flows, from turbulent channels (Vance *et al.*, 2006) to homogenous turbulence (Meneguz & Reeks, 2011) and planar jets (Masi *et al.*, 2014). However, experimental observations of Eulerian particle velocity correlations have been rarely reported, Khalitov & Longmire (2003) and Sahu *et al.* (2014) being notable exceptions. Figure 2.15 indicates that HiSt particles display a larger uncorrelated component of the motion than LoSt, consistently with the mesoscopic Eulerian formalism.

From figure 2.15 one also observes that more inertial particles show a slower decay of velocity correlation with increasing separation, according to the picture of high-St particles responding to larger turbulent scales. Moreover, the streamwise fluctuations are significantly more correlated in streamwise than spanwise directions. This is consistent with the idea that the correlated particle motion is dictated by the turbulent flow. Indeed, if one defines integral scales of the fluctuating particle velocity based on the separation at which the correlation drops by 50%, the transverse scale appears to be roughly half the longitudinal one, similar to the expected behavior of the underlying turbulence. The polar diagrams of R_{uu} in figure 2.16 confirm this picture, and further suggest that the particle motion is organized in large streamwise-elongated structures, whose half-width is about $0.5h$. This is consistent with the spatial particle distributions as deduced from the RDFs.

After considering two-point statistics at the center-plane, we move our attention to the near-wall plane. We focus on the LoSt case, for which more significant preferential concentration is expected. Figure 2.17 displays global and directional RDFs and ADFs, which indicate how the particles are arranged in elongated streaks, multiple channel heights in length. Indeed, due to the highly anisotropic spatial distribution of the particles in this region, the global RDFs provide limited insight compared to the directional

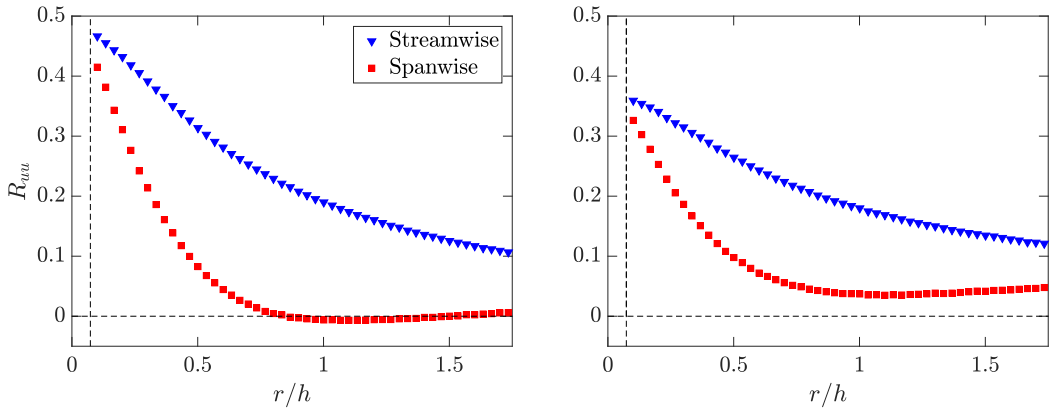

Figure 2.15: Two-point correlation of streamwise velocity fluctuations with separations in streamwise and spanwise directions along the center-plane, for (a) LoSt-HiVF and (b) HiSt-HiVF. The vertical dashed line indicates the laser sheet thickness.

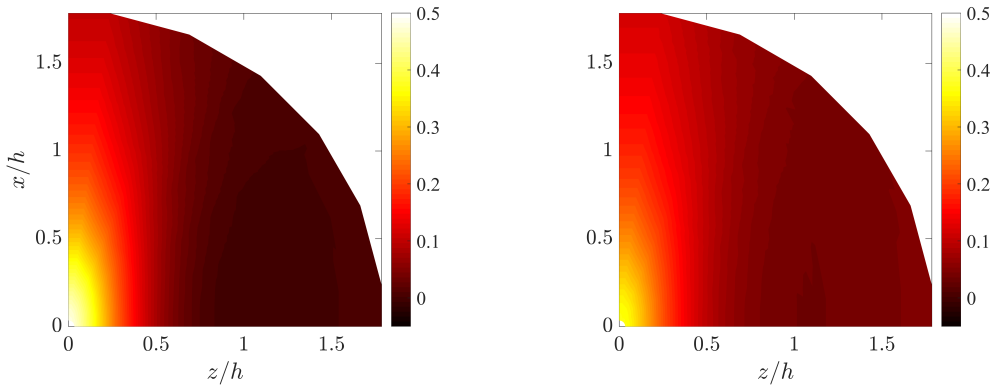

Figure 2.16: Polar map of streamwise velocity two-point correlation along the center-plane, for (a) LoSt-HiVF and (b) HiSt-HiVF.

representations. The amplitude of the peak is significantly smaller than at the center-plane, indicating generally weaker clustering. This is consistent with the fact that particles have much larger response times than the near-wall turbulent scales. As mentioned in the Introduction, several authors used point-particle simulations to investigate the near-wall structure of the particle distributions in regimes for which turbophoresis and preferential concentration are intense (McLaughlin 1989; Zhang & Ahmadi 2000; Rouson & Eaton 2001; Marchioli & Soldati 2002; Soldati & Marchioli 2009; Sardina *et al.* 2012*a*; Bernardini 2014). They found thin streaks separated by $\mathcal{O}(100)$ wall units, which roughly correspond to fluid-phase low-speed streaks in wall-bounded flows (Robinson, 1991), and are even longer than the fluid streaks. Experimental observations of particle streaks have been sporadic, and mostly limited to snapshot realizations (Kaftori *et al.* 1995*a*; Niño & Garcia 1996). The present measurements provide quantitative information on such structures: the spanwise RDF shows a minimum at separations of $\sim 0.3h$ or 70 wall units (which can be interpreted as a measure of the streaks width) and recovery to a local maximum at $\sim 0.75h$ or 175 wall units (a measure of the streak spacing). These values are somewhat larger than what reported by numerical studies at similar regimes. Moreover, the RDF amplitude we observe at small separations is much smaller than in computations, as will be confirmed by instantaneous particle distributions shown later. Beside the above-mentioned limitations of the point-particle modeling approach, the differences can be partly attributed to the location and thickness of the observation region. Most numerical studies report on streaks along thin slices within the viscous sublayer, which are challenging to isolate in laboratory experiments. Here the imaged particles are contained in a slab of thickness ~ 1.1 mm centered at $y/h \sim 0.11$, thus in the approximate range $y^+ = 17 - 34$. The projection through this thickness may significantly influence the apparent concentration in a region of large wall-normal gradients. Future quantitative comparisons with simulations should take into account such finite thickness of the illumination volume.

When compared to the center-plane, the two-point velocity correlations at $y/h = 0.11$ show an even stronger uncorrelated component of the motion as shown in figure 2.18. The uncorrelated velocity component near the wall is expected to increase with increasing particle inertia (Fevrier *et al.*, 2005), and indeed in the near-wall region the particle response time is much larger than the local time scale of the turbulence (i.e.,

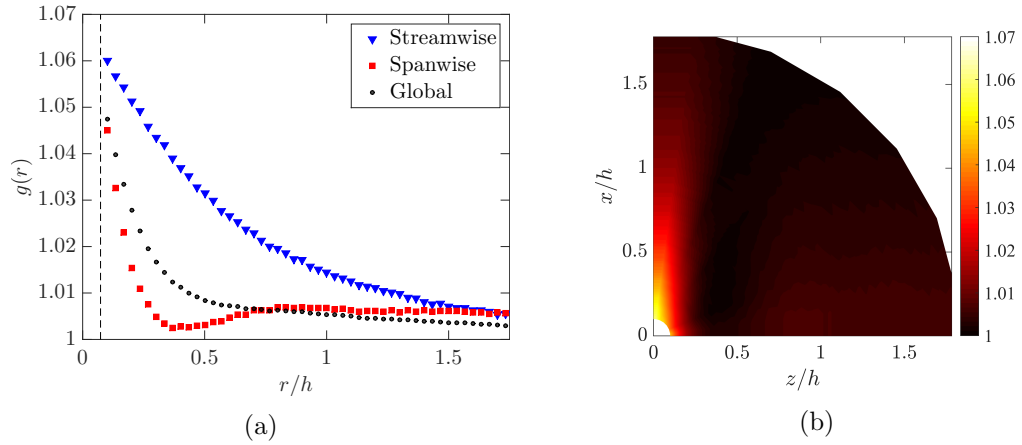

Figure 2.17: (a) Global and directional RDFs and (b) ADF for the LoSt-HiVF case along the near-wall plane.

$St^+ \gg 1$). Besides inertia, inter-particle and wall-particle collisions may also contribute to the random particle motion (Vance *et al.*, 2006). In the HiVF regime considered, both near-wall concentration and deposition velocity are relatively high (§2.2.1), thus collisions may play a significant role in the observed partitioning between correlated and uncorrelated velocity. The negative lobe of velocity correlation along the spanwise direction indicates that the particles are arranged in a streaky fashion, alternating positive and negative streamwise velocity fluctuations. The longitudinal extent of those features cannot be precisely assessed from the present measurements, but the long tail of the correlation function in streamwise direction suggests they can extend beyond the field of view. The trends in figure 2.18 are quantitatively similar to the RDFs and ADFs in figure 2.17, implying that the fluctuations of particle velocity and concentration are simultaneous. We will elaborate on this point in the next subsection.

2.3.2 Domain tessellation

In order to further investigate the instantaneous distribution of the inertial particle positions and velocities, we apply domain tessellation methods along the wall-parallel planes. These have been widely used to study clustering of inertial particles in turbulence (Monchaux *et al.*, 2012). These approaches should be considered complementary

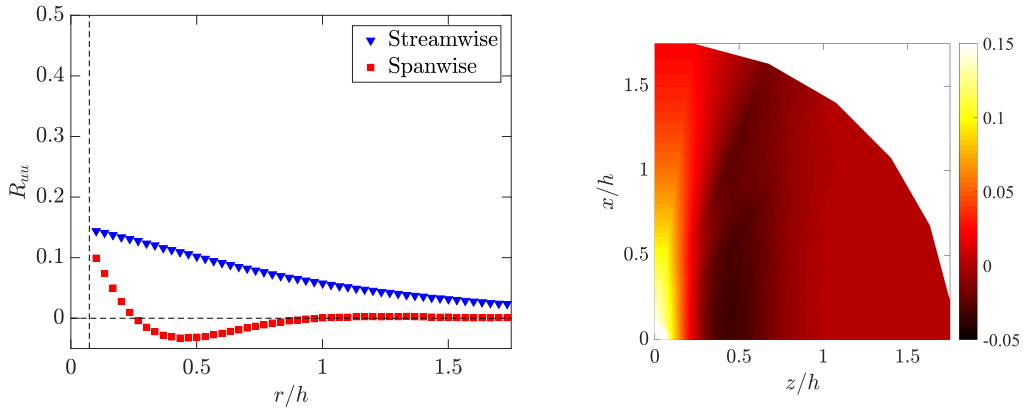

(a) (b)

Figure 2.18: (a) Two-point correlation of streamwise velocity fluctuations with separations in near-wall plane. (b) Spatial velocity correlation map for streamwise velocity fluctuations of inertial particles in the near-wall plane.

to RDFs, since the latter are strictly two-point quantities, while tessellations are sensitive to the multi-particle arrangement. The simplest method is perhaps box-counting, which consists of dividing the domain into boxes of equal size, counting the particles in each box, and comparing the PDF of the number of particles per box against the Poisson distribution expected for randomly distributed particles. This technique provides a simple scalar measure of the amount of clustering and has been fruitfully exploited in experimental studies (Fessler *et al.* 1994; Aliseda *et al.* 2002). In recent years, the Voronoi tessellation method (Monchaux *et al.*, 2010) has gained broader favor: the domain (in our case the two-dimensional image) is divided into cells associated to individual particles, each cell containing the set of points closer to that particle than to any other. The inverse of the area of each cell equals the local instantaneous concentration, $C = 1/A_{cell}$. The method has been used in several experimental and numerical studies of wall-bounded particle-laden flows (Garcia-Villalba *et al.* 2012; Nilsen *et al.* 2013; Nicolai *et al.* 2013; Rabencov *et al.* 2014). Compared to the box-counting method, it has the advantage of not requiring an extrinsic/arbitrary length scale (the box size).

Here we adopt the Voronoi tessellation to investigate the particle distribution along the center-plane. Figure 2.19a shows a sample instantaneous realization for the LoSt-HiVF case, with Voronoi cells drawn around each particle. In figure 2.19c the PDF of the

cell areas (normalized by its ensemble average) is plotted. As typical of inertial particles clustered by turbulence, the distribution is much wider compared to a random Poisson process, which is well approximated by a Γ distribution (Ferenc & Néda, 2007). The PDF of the Voronoi cells is found to closely follow a log-normal distribution (Monchaux *et al.* 2010; Petersen *et al.* 2019), which allows us to characterize the curve by its standard deviation σ_A. The latter is a metric of the amount of clustering: LoSt and HiSt cases are found to have $\sigma_A/\langle A_{cell}\rangle = 0.78$ and 0.70, respectively, confirming that the former has stronger tendency to produce clusters.

The topology and behavior of clusters of highly concentrated particles are relevant to the interphase coupling, especially in view of significant collective backreaction of the dispersed phase on the carrier fluid. We therefore analyze individual clusters (colored in figure 2.19b), defined as connected groups of particles whose Voronoi cell areas are smaller than a threshold value A^*_{cell} (figure 2.19c): the latter is taken as the value below which the probability of finding small cell areas is higher than for randomly distributed particles (Monchaux *et al.*, 2010). To avoid spurious edge effects, we apply the additional constraint that the area of the cells neighboring a cluster also be smaller than A^*_{cell} (Zamansky *et al.*, 2016). The sum of the areas of all cells belonging to each cluster is taken as its "cluster area", A_C.

Figure 2.20 shows the probability distribution of cluster areas $P(A_C)$ along the center-plane for LoSt and HiSt, the PDF in (a) normalized by the corresponding Kolmogorov length scale and (b) normalized by the square of the channel half-height, h^2. Consistent with previous experimental studies, typical sizes are $\mathcal{O}(10\eta)$ (Aliseda *et al.*, 2002), although such estimates may be affected by the number of particles in the system (Petersen *et al.*, 2019). HiSt particles tend to cluster over larger sets, consistent with their limitation of only responding to the larger scales of turbulence. Above a certain size the probability distributions approach a power-law decay, which is a feature of fractality or geometric self-similarity, indicating a fractal-like formation process due to turbulence (Baker *et al.*, 2017). This was clearer in the homogeneous turbulence studies of Sumbekova *et al.* (2017) and Petersen *et al.* (2019), probably due to a combination of limited number of particles in the field of view and limited dynamic spatial range at the present Reynolds numbers. Figure 2.20b shows that normalizing by the channel half-height produces a remarkable collapse of the LoSt and HiSt cases. This

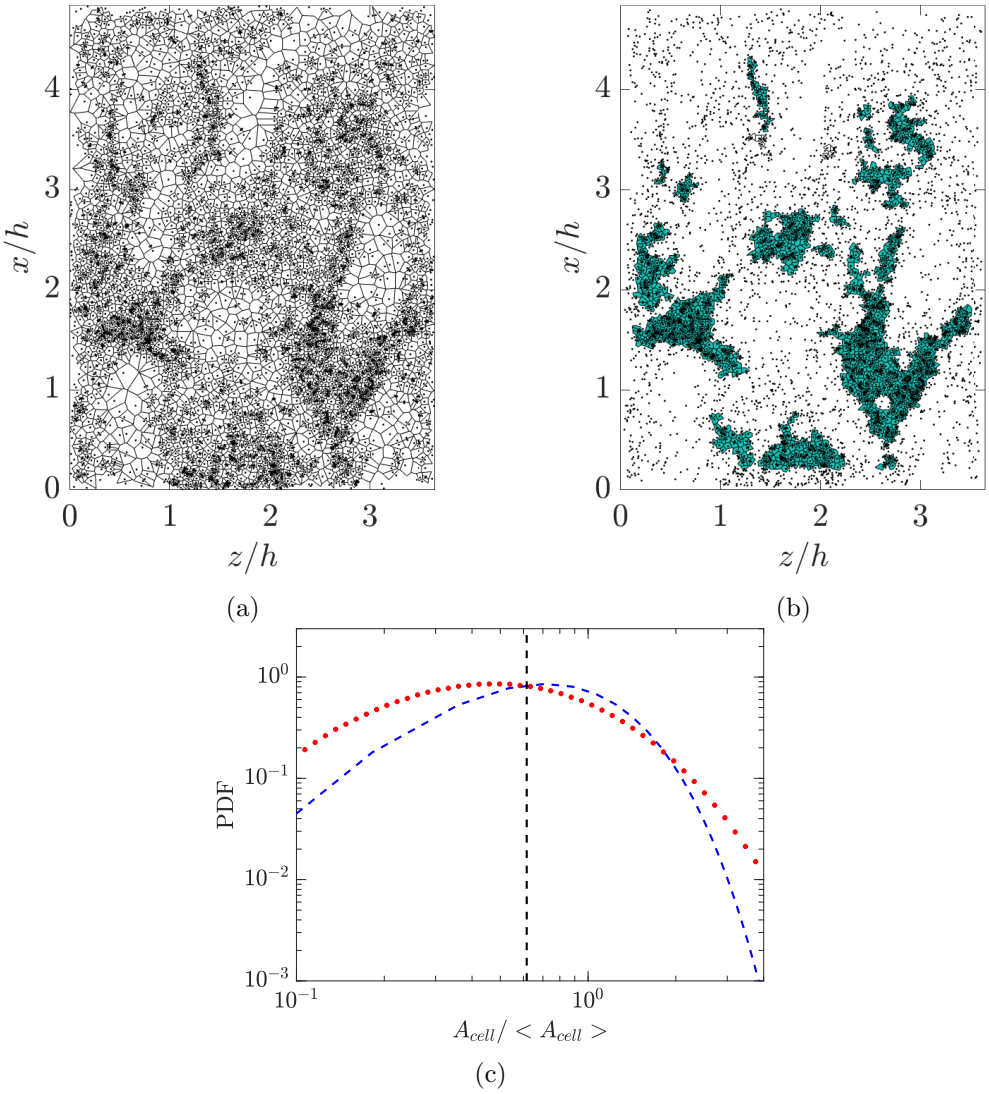

Figure 2.19: (a) Voronoi tessellation diagram in a sample center-plane realization, with (b) highlighted clusters (coherent clusters in cyan). (c) PDF of the Voronoi cell areas A_{cell} along the center-plane (red circles), compared with a Γ distribution (blue dashed line); the vertical dashed line indicates the threshold A^*_{cell}.

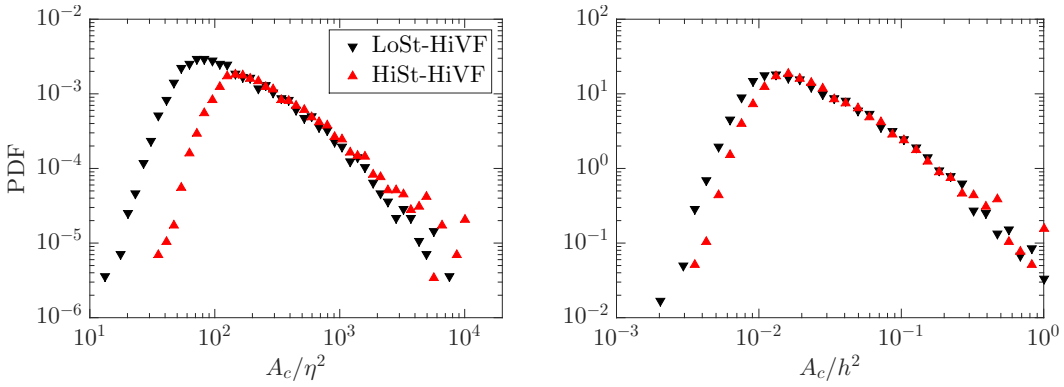

Figure 2.20: PDF of the cluster areas for the LoSt-HiVF and HiSt-HiVF cases in the channel center plane, normalized by (a) the Kolmogorov scales corresponding to the flow velocity, and (b) the square of the channel half-height, h^2.

may suggest that, while particle clustering at the present St is influenced by small-scale turbulence, the energetic scales of fluid motion also play a major role (as recently argued, e.g., by Petersen *et al.* 2019). Moreover, this may indicate that the cluster size is significantly influenced by the channel geometry. Indeed, an *a priori* estimate of the controlling effect of channel walls on clustering is often deduced from the ratio of the channel height to a characteristic cluster size, $L_c = \tau_p^2 g$ (Capecelatro et al. 2014). Here $L_c = 2.8$ mm and $2h/L_c = 10.6$, and the value of L_c is close to the peak of PDF(A_c). We remark, however, that the definition of L_c is usually adopted in much denser regimes than the present one, being independent of the air flow characteristics. Further studies with different particle properties and turbulence conditions shall discriminate whether L_c is an appropriate scale for highly dilute systems.

Following Baker *et al.* (2017), we define "coherent clusters" as those objects large enough to display a scale-invariant topology, i.e. in the range of $P(A_C)$ that approximates the power-law decay. Smaller objects are considered as randomly occurring groups of particles, not necessarily brought together by the underlying turbulent flow. We conventionally set the cutoff at the respective maxima of $P(A_C)$ for both LoSt and HiSt, noting that the choice of twice larger cutoffs does not qualitatively change the observed trends. Besides the physical interpretation discussed in Baker *et al.* (2017), this step allows us to discard clusters formed by only a few particles (too small for a

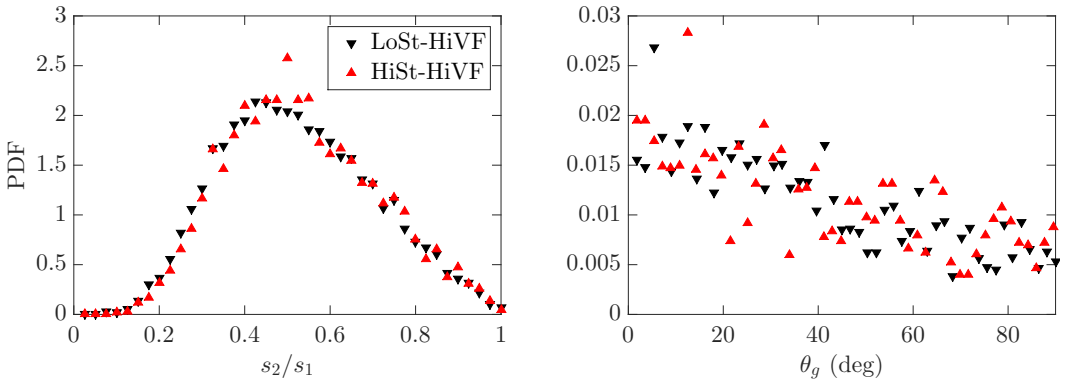

Figure 2.21: PDFs of (a) the SVD-based aspect ratio and (b) the angle between the primary axis and the vertical for the LoSt-HiVF and HiSt-HiVF cases.

meaningful topological description).

We use the singular value decomposition (SVD) method introduced by Baker *et al.* (2017) to probe the shape and spatial orientation of the coherent clusters. The SVD provides the principal axes and corresponding singular values for a particle set: the primary axis lies along the direction of greatest particle spread from the cluster centroid, the secondary axis being orthogonal to it. The corresponding singular values s_1 and s_2 measure the spread along the respective axes. In figure 2.21a the PDF of the aspect ratio s_2/s_1 is plotted for LoSt (differences with HiSt are marginal). The limit values 0 and 1 correspond to particles arranged in a straight line and in a perfect circle, respectively. The distribution is quantitatively similar to what reported by Petersen *et al.* (2019) for clusters settling in homogeneous turbulence. The peak ratio between 0.4 and 0.55 reflects a tendency to form somewhat elongated objects. Figure 2.21b illustrates the probability distribution of the primary axis orientation, measured by the angle of the latter with the vertical (θ_g). The peak at $\theta_g = 0$ indicates a tendency of the (coherent) clusters to be aligned with gravity (and thus the direction of motion). This behavior was also reported in homogeneous turbulence studies (Baker *et al.* 2017; Petersen *et al.* 2019) and is consistent with the directional RDFs and ADFs presented above.

The local particle concentration within clusters can be significantly higher compared to the global value C_0 (Baker *et al.*, 2017). Figure 2.22 shows PDFs of C/C_0 associated with the particles within coherent clusters, compared to the unconditional distribution:

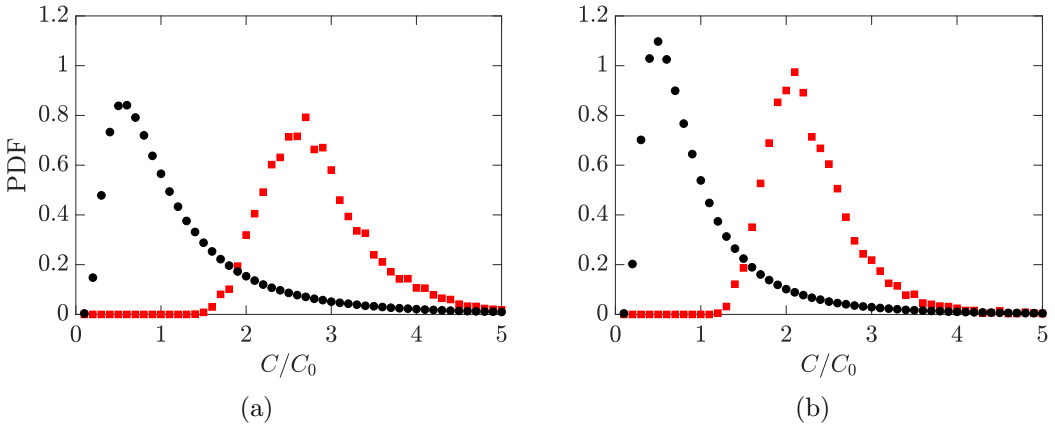

Figure 2.22: PDFs of normalized in-cluster (shown in red squares) and global concentrations (in black circles) for (a) LoSt-HiVF and (b) HiSt-HiVF.

the peaks in the PDF for the clustered particles are about four times higher in HiSt and almost five times higher in LoSt. Besides reaffirming that the latter case displays more intense clustering, these plots indicate how the in-cluster concentration can be substantial, such that two-way-coupling (and possibly four-way-coupling) effects may be at play.

The traveling velocity of the clustered particles is also important to the transport process. Figure 2.23a depicts the same instantaneous realization as in figure 2.19, with the Voronoi cells now color-coded by the streamwise velocity of the respective particles. The more concentrated regions appear associated with higher velocities, as confirmed by the joint PDF for LoSt-HiVF (figure 2.23b): the local particle concentration and streamwise velocity are positively correlated. For a more quantitative account, shown in figure 2.24 are the PDF of the streamwise velocity for particles belonging to coherent clusters along the center-plane, as well as for all particles in the field of view. The clustered particles travel downward measurably faster than the generic particles. The explanations may be two-fold: on one hand, particles may be favoring the downwash side of turbulent eddies, according to the picture of preferential sweeping originally proposed by Maxey (1987) and later demonstrated by the simulations of Wang & Maxey (1993) and recently by the experiments of Petersen *et al.* (2019); on the other hand, the highly concentrated clusters may be exerting a collective drag force on the fluid, in turn enhancing their vertical velocity as shown in the numerical simulations of Bosse *et al.*

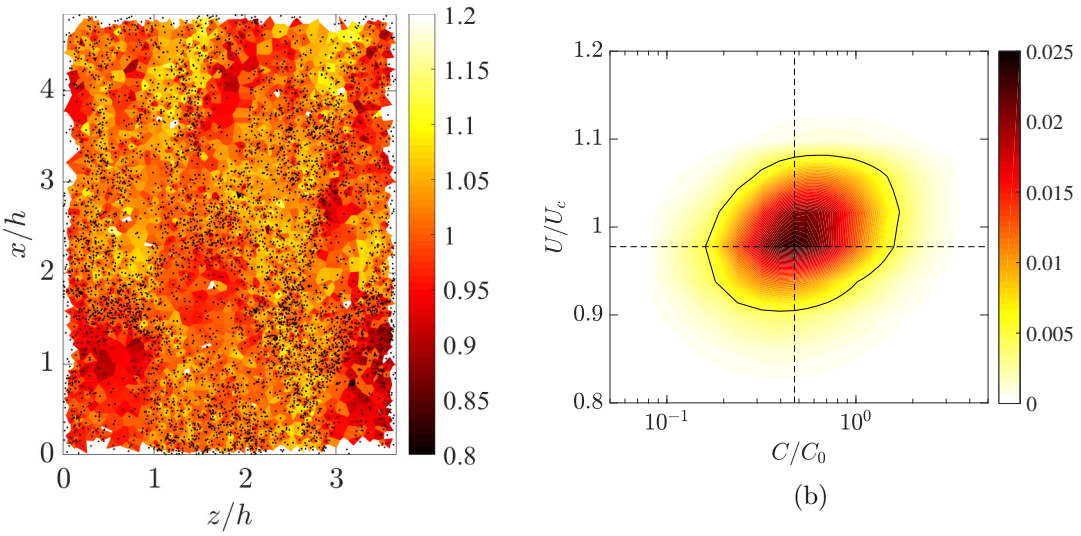

(a) (b)

Figure 2.23: (a) The same instantaneous realization as in figure 2.19, with the Voronoi cell color-coded by the local particle streamwise velocity. (b) Joint PDF of streamwise velocity and concentration at the center-plane for the LoSt-HiVF case. The dashed lines indicate the velocity and concentration values averaged along the center-plane. The black contour line indicates the PDF level at 0.005.

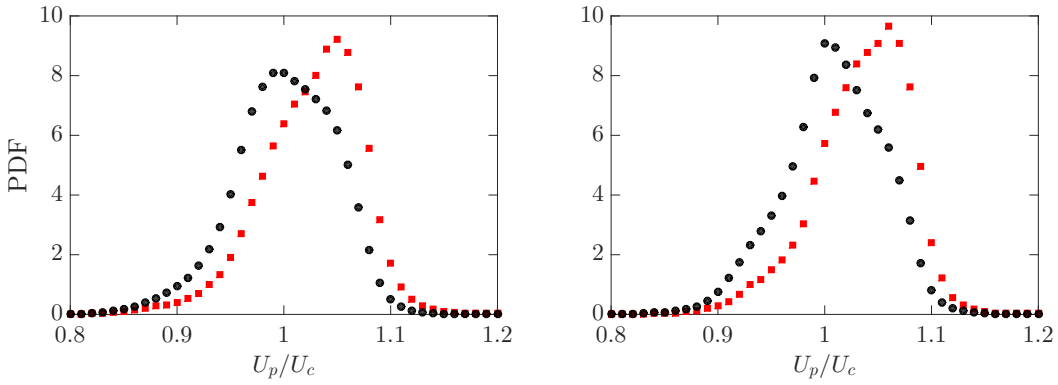

Figure 2.24: PDFs of normalized in-cluster (shown in red squares) and global velocities (in black circles) for (a) LoSt-HiVF and (b) HiSt-HiVF in the channel center plane.

(2006) and Frankel *et al.* (2016).

In principle, the Voronoi method may also be used to identify the highly concentrated structures near the wall. However, figure 2.25a shows how the PDF of the Voronoi cell areas measured along the near-wall plane is in fact narrower than for randomly distributed particles. This may be an artifact due to the relatively high concentration near the wall: particles very close to each other might be identified as one, reducing the probability of detecting small cell areas. Alternatively, the actual topology of the particle field, expected to be organized in streaks, could result in a "crystallized" pattern with a relatively regular arrangement of cells (and thus a narrow PDF of their area). Either way, the Voronoi tessellation method (in its standard form) does not appear as a suitable tool to study clustering in the present near-wall particle fields. We therefore resort to the box-counting approach: we tessellate the domain with square boxes of size 60 wall units or $\sim 0.18h$, and in figure 2.25b we plot the PDF of the concentration in each box C_{box}, comparing it with the Poisson distribution expected for randomly located particles. The relatively broad distribution indicates that the particles are indeed clustered over scales of the order of the box size. The choice of the latter is informed by the width of the particle streaks as estimated from the RDF analysis in the previous subsection, although it is verified that varying it by a factor two yields similar conclusions. The box index $BI = (\sigma - \sigma_{Poisson})/\mu$ (where μ and σ indicate mean and standard deviation of the distribution, respectively, and $\sigma_{Poisson}$ is the standard deviation of the Poisson

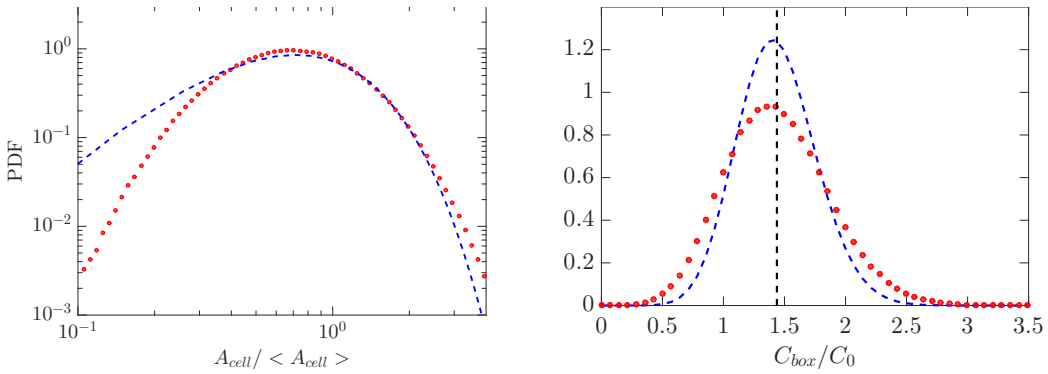

(a) (b)

Figure 2.25: (a) PDF of the Voronoi cell areas A_{cell} along the near-wall plane (red cicles), compared with a Γ distribution (blue dashed line). (b) PDF of particle concentration in square boxes of size $0.18h$ used to tessellate the near-wall plane (red circles) compared to a Poisson distribution (blue dashed line).

distribution) is a comparative measure of clustering. Near the wall we find $BI = 0.05$, while $BI = 0.2$ at the center-plane. The latter (consistent with the results of Fessler *et al.* 1994) confirms the indication from the RDF analysis that clustering in the channel core is significantly more intense.

Figure 2.26a shows an instantaneous realization of the near-wall particle field, color-coded with the mean particle velocity in each square box of the tessellation. The visual impression of elongated slow-velocity streaks is in line with the RDF results. In figure 2.26b we plot a joint PDF of local particle concentration and streamwise velocity, based on values averaged in each box. The apparent negative correlation contrasts with the center-plane trend in figure 2.23b, indicating a tendency of the highly concentrated particles to travel slower than the average. Combined with the RDFs, ADFs and two-point correlations reported above, this confirms the picture of particles accumulating in slow-moving streaks.

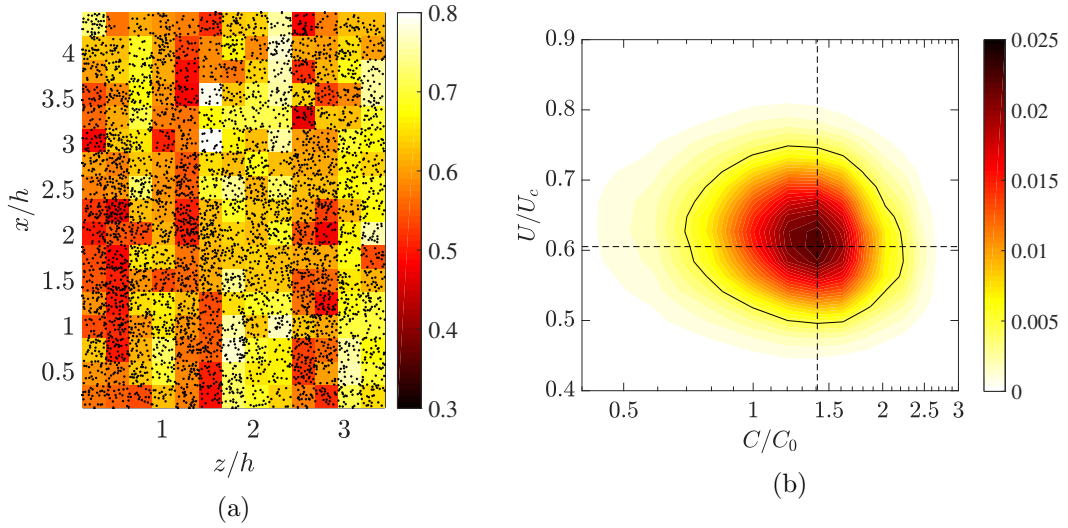

Figure 2.26: (a) Sample realization at the near-wall plane, tessellated by $0.18h \times 0.18h$ boxes and color-coded by the mean local streamwise particle velocity within the boxes. (b) Joint PDF of streamwise velocity and box-based concentration at the near-wall plane for the LoSt-HiVF case. The dashed lines indicate the velocity and concentration averaged along the near-wall plane. The black contour line indicates the PDF level at 0.005.

Chapter 3

Highly concentrated falling inertial particles in a vertical riser

In this chapter we discuss a flow where highly inertial particles are falling against forced rising air. This is commonly know as particle risers, which are ubiquitous setups in chemical engineering systems, e.g., as part of circulating fluidized beds (Shaffer *et al.* 2013,Capecelatro *et al.* 2014). They are utilized in industrial processes to increase contact efficiency between the reacting gas and solid phases, for example in coal combustion and biomass pyrolysis processes (Beetham & Capecelatro, 2019). The high solids concentration in the flow leads to a non-negligible backreaction of the dispersed phase onto the carrier fluid, and enable new pathways for energy dissipation via, e.g., interparticle collisions (Elghobashi 1994, Fullmer & Hrenya 2017). A phenomenon commonly observed in these regimes is the development of local regions of densely packed particles, referred to as clusters (Shaffer *et al.* 2013, Varas *et al.* 2017). These have sizes of the order of the riser channel diameter (Capecelatro *et al.*, 2014) and can greatly alter the bulk mass and heat transfer properties of the system, as well as reduce contact between the reactive phases leading to reduced efficiency of the reactions (Beetham & Capecelatro, 2019).

The prominence of particle risers in industrial settings has led to many experimental and numerical studies. Early computational works developed two-fluid models for dense particle-laden flows, modelling both phases as continuums (Agrawal *et al.*, 2001), and

observed formation of clusters when the particle phase is settling in a quiescent fluid medium. This approach is powerful and scalable to full-reactor sizes, but its ability to capture meso-scale structures such as clusters is dependent on the grid resolution, and does not provide insight on the microscopic sequence of events that lead to cluster formation. Modern advances in computing power have enabled gas-solid simulations of higher resolution to be performed, both in risers and for particles settling in quiescent fluid (Capecelatro *et al.* 2014,Capecelatro & Desjardins 2015, Capecelatro *et al.* 2015, Guo & Capecelatro 2019). These studies used the Eulerian-Lagrangian framework, where individual particle trajectories are resolved, including collisions. Clusters are observed and the ability to track individual particles within these clusters enable direct quantification of granular temperature and radial distribution functions. Even more highly resolved models, namely particle-resolved direct numerical simulations (PR-DNS), are able to resolve the flow field around each particle and can be used to validate closure laws for higher-order models (Tenneti & Subramaniam, 2014), but are limited in the number of particles simulated and thus are still unable to capture meso-scale structures (Sundaresan *et al.*, 2018).

In contrast, experimental studies are relatively scarce, having to face the challenges posed by the opaqueness of dense gas-solid flows. Shaffer *et al.* (2013) and Breault *et al.* (2020) investigated experimentally the formation of clusters in particle risers in laboratory-scale circulating fluidized beds. However, these experiments report mostly on the bulk properties of the riser, such as pressure drops and mean velocity profiles, and instantaneous details of the concentration and velocity fields are only observed adjacent to a transparent window. More recently, a series of quasi-two-dimensional riser experiments conducted by Varas *et al.* (2017) gave a comprehensive view of the concentration distribution of particles and their velocities within the riser, as well as discussed cluster detection strategies and their morphology. These studies, while providing valuable insights in dense gas-solid flows, are limited by the two-dimensional setup; this is numerically shown to exaggerate particle concentration and fluctuations in volume fractions due to restraining each particle to a limited plane of motion (Capecelatro *et al.*, 2014). Importantly, most of the studies mentioned above utilized a fluidized bed riser setup, in which the amount of particles is constant and both concentration and gas velocity are controlled by the flow rate of fluidization. This is similar to industrial setups but

provides poor control over the solids volume fraction across the whole system, which can range from almost completely packed near the bottom to highly dilute at the top of the riser. Also, this setup does not allow the important parameters to be controlled independently, limiting the insight into the fundamental particle-fluid dynamics. These limitations are solved in the present experimental study, where we configure a 3D riser in which the solid volume fraction and gas flow rate can be controlled independently, while spatially and temporally resolving particle concentration and velocity fields. The present study is focused on a vertical square duct in which mono-dispersed spherical particles are suspended by an upward air flow. The simplicity of the configuration allows us to tackle fundamental issues in gas-solid flows, in which we pay special attention to the formation and characteristics of clusters.

3.1 Experimental setup

3.1.1 Experimental facility and parameters

Experiments are conducted in the riser facility depicted in figure 3.1. This features a vertical square duct, 21 mm x 21 mm in cross-section and 1 m long. The air flows upwards driven by a 1.5 kW centrifugal blower (Atlantic Blowers), with the flow rate monitored by a digital flowmeter (Kelly Pneumatics) at the inlet of the channel. In an upper chamber of the wind tunnel above the riser section, size-selected glass beads (Mo-Sci Corp.) with a density of 2500 kgm^{-3} and diameter of 212 $\pm$ 21 µm (mean $\pm$ standard deviation) are released in the flow through a 3D printed funnel that smoothly connects to the vertical duct. The funnel has interchangeable throat insets to control the feeding rate. The particle size (and density) places them in the Geldart Group B category (Cocco *et al.*, 2014) and yields a ratio of channel width-to-particle diameter $2h/d_p = 100$. The funnel is kept full by means of a screw-feeder (Vibra Screw Inc.) to ensure steady particle dispensing. Flow conditioners (three screens and two honeycombs) are placed at both ends of the apparatus, guaranteeing uniform particle influx at the top and smooth air inflow at the bottom. The upper conditioning section also features an additional honeycomb in the funnel which damps fluctuations that would occur due to flow separation. The particle distribution is verified to be uniform through the channel when they are in free fall (no airflow). The particles are collected in a 3-litre

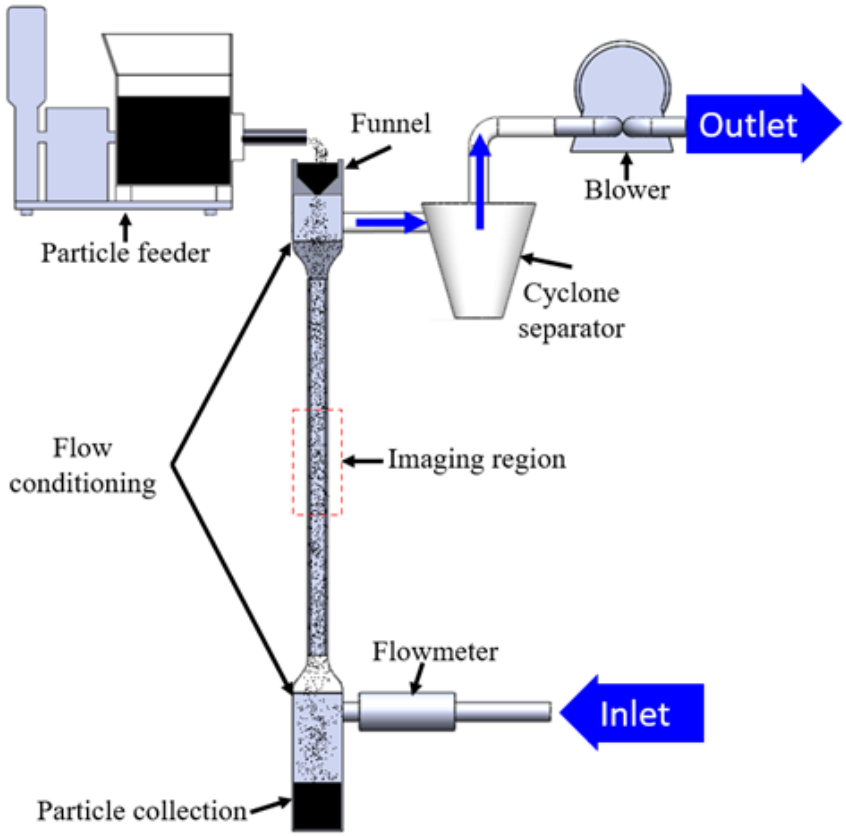

Figure 3.1: A schematic diagram of the particle-laden channel flow facility and its main elements.

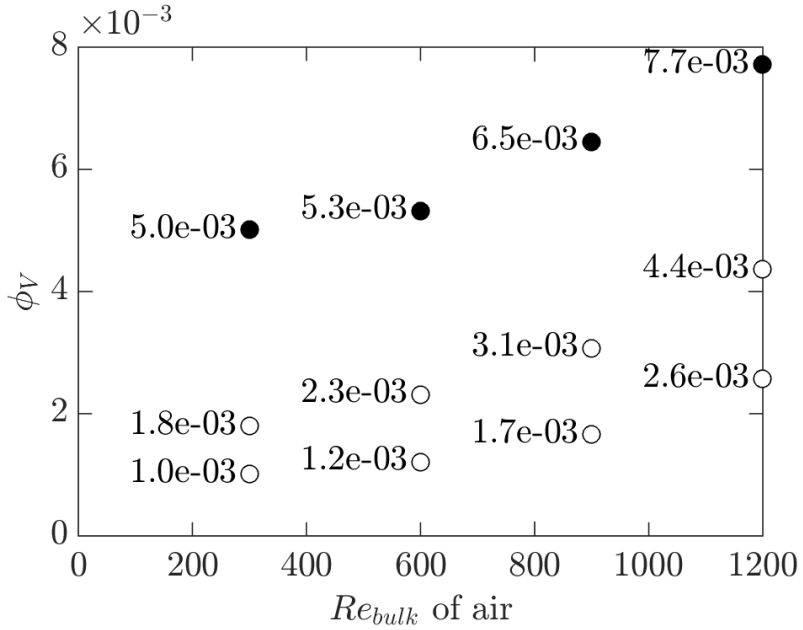

Figure 3.2: Parameter space probed in the particle riser experiment. Filled symbols indicate clustering cases whereas non-filled symbols indicate non-clustering cases. The value of the particle fraction, ϕ_V is also printed beside each point for clarity.

chamber at the bottom. The transparent section for imaging is made out of Electrostatic dissipative acrylic (SciCron Technologies), which was shown in the previous chapter to prevent particle adhesion.

The fluid flow and particle parameters are listed in table 3.1. A range of particle feeding rates and fluidizing air velocities are considered, leading to the parameter space in figure 3.2. This is defined by the flow Reynolds number Re_{bulk}, based on the bulk velocity of the airflow and the channel height, and the particle volume fraction ϕ_V. The latter is determined from the image intensity using the calibration procedure described later. While the range of Re_{bulk} is well within the laminar regime for a single-phase flow (Pope, 2000), the significant loadings of massive particles leads to significant flow fluctuations of the gas-solid mixture, as we shall discuss. Indeed, the still-air terminal velocity $U_t = \tau_p g$ (where τ_p is the particle response time calculated with the formula by Schiller & Naumann (1933) is larger than the bulk flow velocity for all cases, suggesting that the source of the fluid fluctuating energy lies in the relative motion between carrier and dispersed phases rather than in the mean shear (Sundaresan *et al.*, 2018). The

Air density, ρ_f (kg m^{-3})	1.2			
Air kinematic viscosity, ν (m^2 s^{-1})	1.5×10^{-5}			
Channel half width, h (mm)	10.5			
Bulk flow velocity, U_{bulk} (m s^{-1})	0.214	0.428	0.642	0.856
Bulk Reynolds number, Re_{bulk}	300	600	900	1200
Particle density, ρ_p (kg m^{-3})	2500			
Mean diameter, d_p (µm)	212			
Particle response time, τ_p (s)	0.155			
Particle terminal velocity in still air, V_t (m s^{-1})	1.52			
Particle Reynolds number in still air, Re_p	21.5			
Galileo number, Ga	29.4			

Table 3.1: Fluid and particle parameters for the investigated cases.

particle Reynolds number $Re_p = U_t d_p/\nu$ and the Galileo number $U_g d_p/\nu$ (where $U_g = [(\rho_p/\rho_p – 1)d_p g]^{1/2}$)) indicates significant wake effects, but no unsteady wake behavior (Ern *et al.*, 2012).

3.2 Zoomed-out measurements

3.2.1 Imaging and calibration procedure

The riser is imaged in the central 200 mm of its length, a tradeoff for the falling particles to approach their terminal velocity and for the upward airflow to develop. We use a backlighting method (figure 3.3a) consisting of a DC LED light source (Lightpanels) and a light diffuser to make the illumination more uniform (Westcott Scrim Jim). Images are taken with a 4-megapixel high-speed camera (Vision Research) and a 105 mm lens (Nikkor, aperture f/2.8) at a standoff distance of 1.5 m, imaging 215 mm streamwise, or about 10 channel widths. The depth-of-field of the camera images encompasses the full channel depth. This is verified by traversing a pair of transparent slides sandwiching sparse glass particles, which are found to be in focus across the cross-section. Examples of instantaneous realizations at different volume fractions are shown in figure 3.3b. The

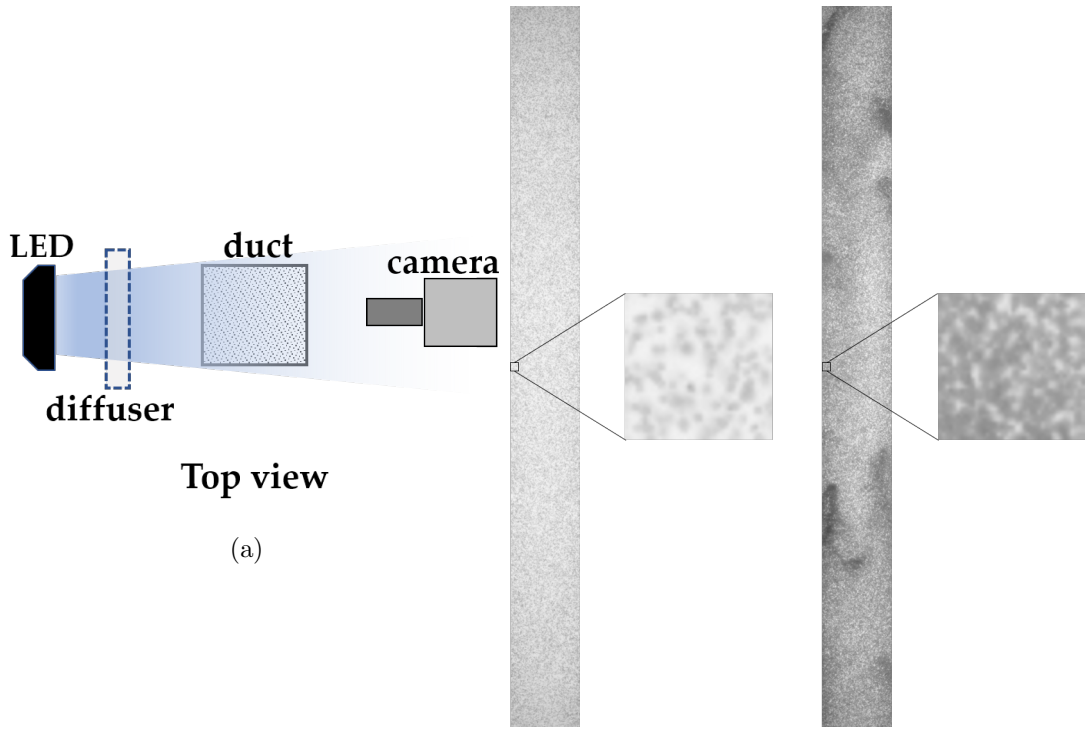

(a)

(b)

Figure 3.3: (a) Imaging setup of the experiment as viewed from the top of the facility. (b) Full frame, raw intensity images for two different volume fractions $\phi_V = 2.6 \times 10^{-3}$ and 7.7×10^{-3}, corresponding to a non-clustered and clustered case. Insets show the corrresponding 40×40 pixel interrogation window as used in PIV.

intensity is inversely related to local particle concentration along the light path, although an exact conversion to the depth-average concentration cannot be assumed.

The acquisition frequency ranges from 2500 to 4000 Hz depending on the flow regime, keeping the displacements of the intensity patterns within approximately 8 pixels. Velocity fields are obtained from successive images using particle image velocimetry (PIV) with 40-by-40 pixel interrogation windows. While individual particles cannot be detected, the patterns (see examples in figure 3.3b) are sufficiently distinct for cross-correlation, as confirmed by signal-to-noise ratio and universal outlier detection techniques (Westerweel & Scarano, 2005). Interrogation refinement and 50% overlap yield a vector spacing of 1.05 mm. Flow statistics are obtained by ensemble averaging 40000 realizations, with acquisition times ranging from 10 to 16 s.

In order to estimate the volume fraction, we establish a relation between particle concentration and pixel intensity. This is done by leveraging the homogeneity of the particle dispersion and velocity observed in the absence of airflow. From the known mass flow rate through the funnel m_p (verified by digital scale measurements) and the fall speed of particles, U measured by PIV (uniform across the width within 70%), the particle volume fraction is calculated as:

$$\phi_V = \dot{m}_p/(4h^2\rho_p U), \tag{3.1}$$

Figure 3.4 shows the spatially averaged brightness of (inverted) images from five free-fall experiments at different volume fractions. Free-fall experiments are used for calibration due to their known mass flow rate and largely uniform particle distribution in the channel. The intensity increases linearly with ϕ_V up to 3×10^{-3}, obtained for the maximum m_p achievable without airflow. While this is significantly lower compared to the riser experiments, the clearly linear trend supports the extrapolation. Bernard & Wallace (2002) also reported that light intensities scattered by monodisperse particles increases linearly with particle concentration.

In order to mitigate the effect of unequal illumination and the shadow cast by the channel walls, this procedure is applied locally, binning the intensity fields in windows congruent with the PIV grid. Linear relations between intensity and volume fraction are determined in each window, and are used to obtain time-resolved ϕ_V fields. To

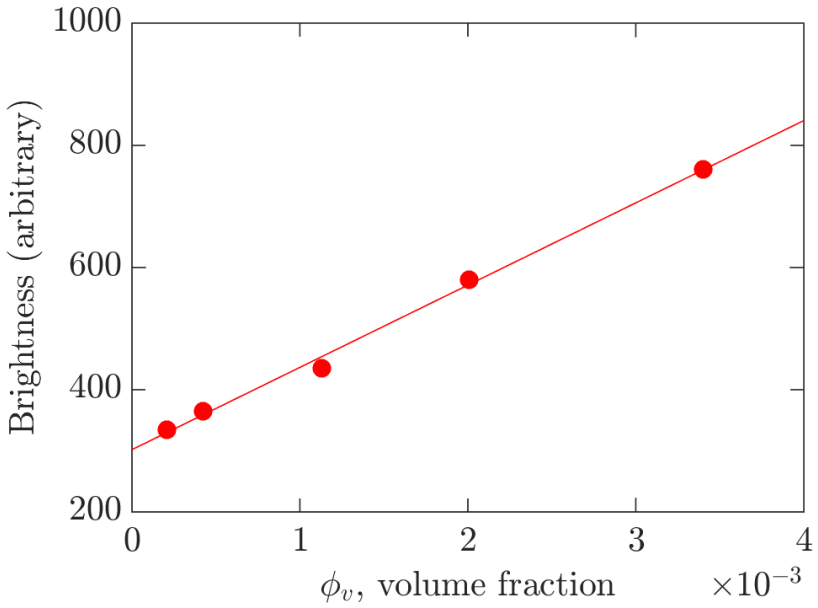

Figure 3.4: Plot of image intensity versus particle volume fractions for 5 calibration cases. The line marks the linear fit.

guarantee unchanged imaging conditions, the free-fall calibration images are acquired right before the riser experiments.

The above procedures to evaluate particle velocity and concentration are affected by the nature of the backlighting, in which the information is integrated through the channel depth in a complex manner. Therefore, the quantitative values do not represent a specific plane location. Yet, this approach allows us to appreciate the riser particle dynamics at concentrations impenetrable to laser illumination.

3.3 Zoomed-out measurements: Results

Throughout this section, U_p denotes the particle vertical velocity which is negative when particles are falling with gravity. U_p is normalized with U_t, which is the single-particle terminal velocity when in free-fall (1.52 m/s).

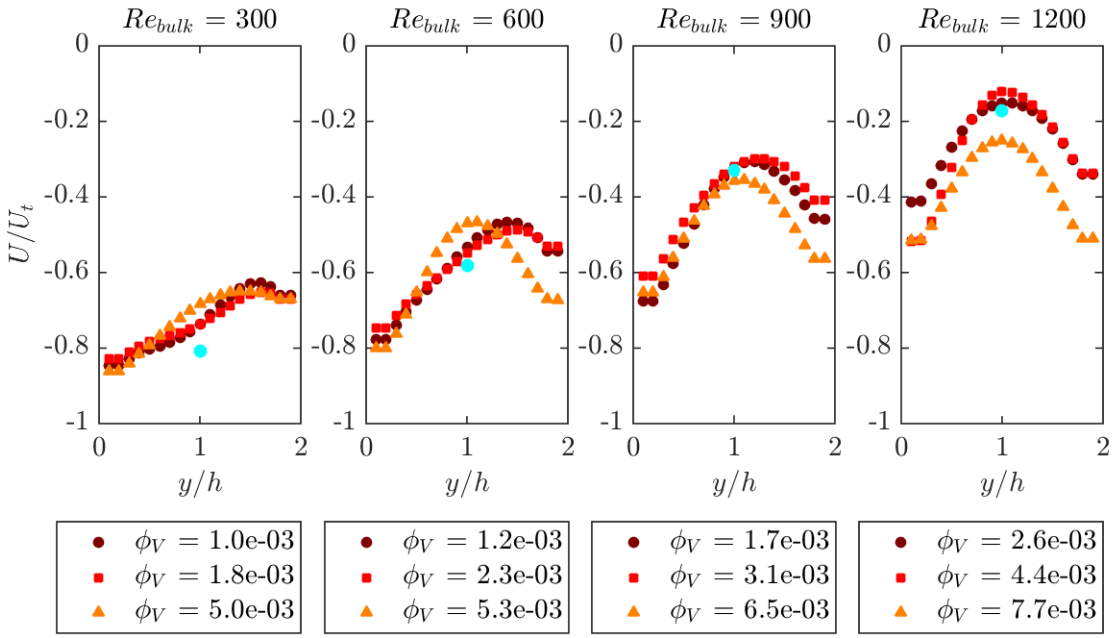

Figure 3.5: Profiles of mean streamwise particle velocity for different volume fractions, grouped by similar bulk fluidizing air velocities increasing from left to right. Cyan circles represent the mean streamwise particle velocity as obtained from the zoomed-in measurements detailed in §3.4 for the lowest volume fraction cases in each Re_{bulk} group.

3.3.1 Particle velocity and concentration profiles

Figure 3.5 displays the wall-to-wall particle mean velocity profiles for the 12 riser cases in different volume fractions as well as bulk fluidizing velocities. The particle falling velocity is mainly correlated with the bulk fluidizing air – as the strength of the air increases, the particles fall slower due to being suspended by the rising air. In this configuration, the particles descent velocities are shown to be reduced to as much as 15% of their single-particle terminal settling velocity in the center, and 40% near the wall. In low fluidization velocities the velocity profiles are asymmetric, likely due to large-scale recirculation of the air flow, the direction of which is expected to be highly sensitive to initial conditions as well as minute irregularities in the channel. In contrast, higher fluidization velocities result in a velocity profile more symmetric about the centerline, due to particle-phase agitation promoting mixing. The particle falling velocity is also weakly dependent on the volume fraction, where a higher volume fraction in the riser generally leads to larger falling velocities. This dependency is more apparent at higher Re_{bulk}. The cyan circles represent the particle streamwise velocities obtained from the zoomed-in measurements (§3.4), where individual particle streamwise velocities in the centerplane are averaged across the channel to obtain a 'depth-averaged' velocity to compare with those of the zoomed-out, optically depth-averaged measurements. Although the comparison is only available for the lowest volume fraction cases in each Re_{bulk} group, the streamwise velocities from both measurements agree well, lending confidence to the measurement technique.

Similar to figure 3.5, figure 3.6 displays wall-to-wall profiles of the r.m.s. fluctuations of the particle streamwise velocities. Here the profiles clearly show that beyond a volume fraction of 5×10^{-3}, the average r.m.s. velocity fluctuation value is about 10 to 20% of U_t and is observed to increase with fluidizing airflow, as well as having larger values near the walls. This is in contrast to the cases with volume fraction below 5×10^{-3}, which have r.m.s. velocity fluctuations of about 5% of U_t regardless of fluidization velocity. The analysis of particle clusters, to be presented later, will provide insight on the origin of these trends.

Figure 3.7 shows the particle volume fraction profile across the channel, with the spanwise-averaged mean shown at the bottom. As mentioned in the Introduction, the particle volume fraction is dependent on the particle flow rates from the funnel as well

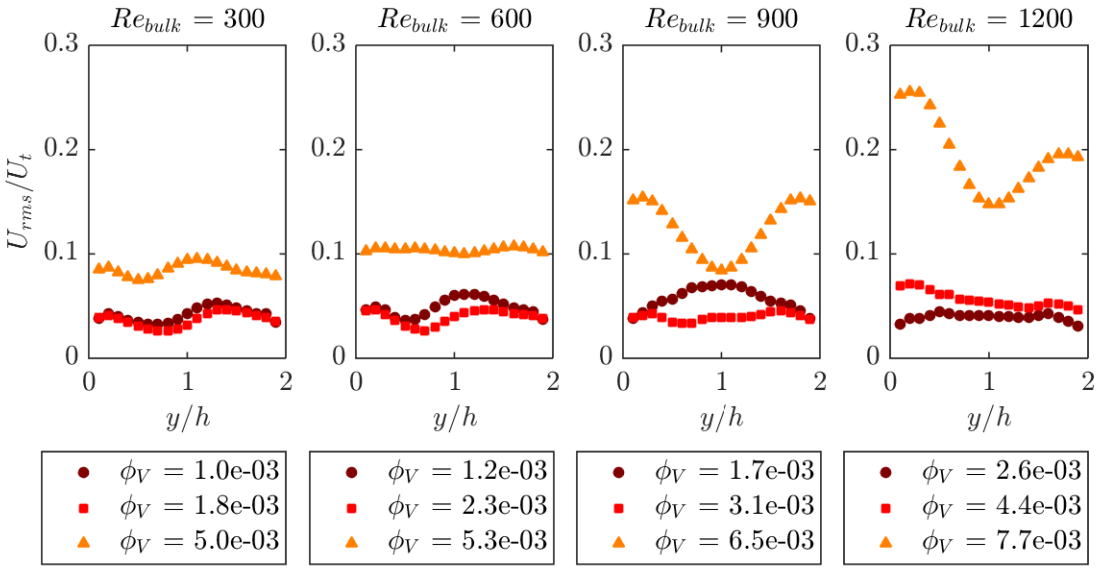

Figure 3.6: Profiles of r.m.s. fluctuations of particle streamwise velocities for different volume fractions, grouped by similar bulk fluidizing air velocities increasing from left to right.

as the bulk fluidizing air velocity. For each particle feed rate, higher Re_{bulk} results in higher volume fractions due to particle resuspension. Higher volume fractions are also observed near the walls for clustering and non-clustering cases, with the difference between near-wall and center-plane concentrations of up to 60%. This is in line with the expected particle distribution which is dilute at the core and more concentrated at the edges, as observed in Zhou *et al.* (1994) for a square cross-section, and McMillan *et al.* (2013) for a circular cross-section, in which the distribution pattern is termed the 'core-annulus' profile. The corner effect is compounded by the backlighting imaging method which results in an approximately depth-averaging as mentioned previously. Here we show again the cyan circles representing the mean particle volume fraction as obtained from the zoomed-in measurements (§3.4). The mean ϕ_V in the centerplane is found by dividing the total volume of particles found with the measurement volume, which is comparable to the depth-averaged ϕ_V at the centerpoint of the zoomed-out measurements (since the channel is square). Here it is shown that the value of ϕ_V are similar between the two measurement methods.

Figure 3.8 shows the profiles of the r.m.s. fluctuations of the particle volume fraction

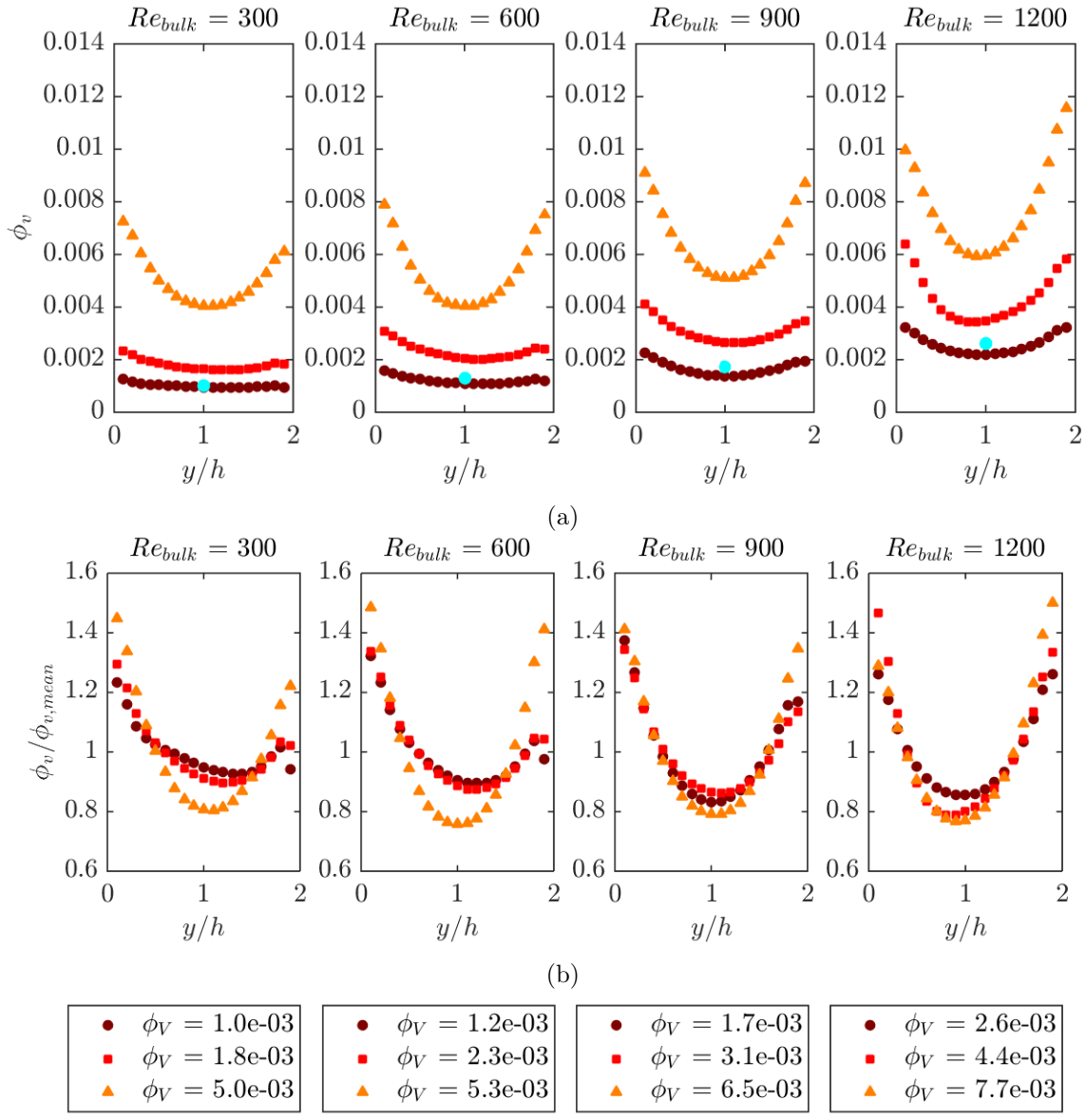

Figure 3.7: Profiles of particle volume fractions for different volume fractions, grouped by similar bulk fluidizing air velocities increasing from left to right. The volume fraction is plotted in (a) and is normalized by the mean volume fraction of the respective case in (b). Cyan circles in (a) represent the mean streamwise particle velocity as obtained from the zoomed-in measurements detailed in §3.4 for the lowest volume fraction cases in each Re_{bulk} group.

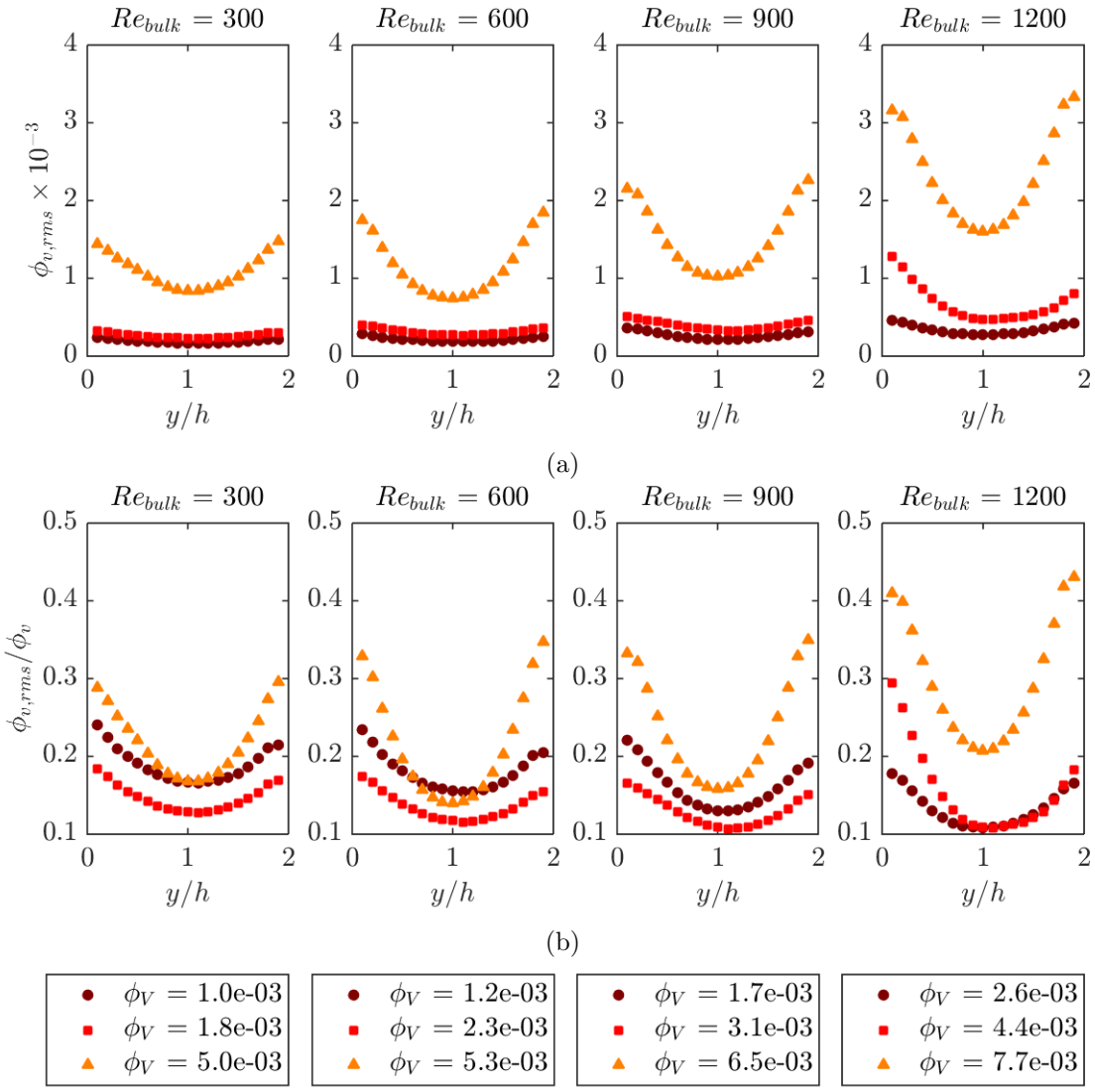

Figure 3.8: Profiles of r.m.s. fluctuations of the particle volume fraction for different volume fractions, grouped by similar bulk fluidizing air velocities increasing from left to right. The raw r.m.s. value is plotted in (a) and is normalized by the mean volume fraction of the respective case in (b).

across the channel for different bulk fluidizing velocities. Similar to the profiles of r.m.s. streamwise velocities , the r.m.s. concentration for the cases ($\phi_V > 5 \times 10^{-3}$) are shown to be an order of magnitude higher compared to the more dilute ones, as shown in figure 3.8a. One particular case of note is the case with $\phi_V = 4.4 \times 10^{-3}$ and $Re_{bulk} = 1200$. This case lies in a transitional regime where the mean volume fraction is below 5×10^{-3}, but the concentration near the walls is above (figure 3.7). Correspondingly, the r.m.s. volume fraction fluctuation profile shows an increase near the walls, suggesting that $\phi_V = 5 \times 10^{-3}$ acts as a threshold. Figure 3.8b shows that the r.m.s. fluctuations normalized by the mean volume fraction is about 20% for all cases. In addition, the difference between the near-wall peaks and the central regions increases with Re_{bulk}.

3.3.2 Space-time autocorrelation maps

We leverage the time-resolved dataset of the riser images to construct autocorrelation maps for both the velocity and concentration fields of the particle-phase in both the spatial and temporal directions. This approach has been commonly used in the turbulence community to track turbulence structures developing in the boundary layer (Dennis & Nickels, 2008), revealing a region of high correlation in space-time that can be used to deduce the convection velocity of the structures. In this analysis we implement a similar procedure using the streamwise velocity fluctuation fields for a given wall-normal location. The wall-normal locations selected are the centers and the second datapoint away from the walls, which are representative of the near-wall regions. The space-time autocorrelation is defined as:

$$R_{uu}(\Delta x, \Delta t) = \frac{\langle u(x,t)u(x+\Delta x, t+\Delta t)\rangle}{\langle u(x,t)^2\rangle}, \tag{3.2}$$

and is calculated for the full streamwise extent and up to 0.2 s in time, beyond which the correlation value drops near zero. Since the full acquisition time ranges from 10 to 16 seconds, we perform the space-time autocorrelation on the time-resolved data split into 0.2 s slices, and calculate the ensemble averaged correlation field $R_{uu}(\Delta x, \Delta t)$ using the correlation field of each slice. The same procedure is carried out on the fluctuating concentration fields.

Figure 3.9 shows the space-time autocorrelation maps for the densest riser case

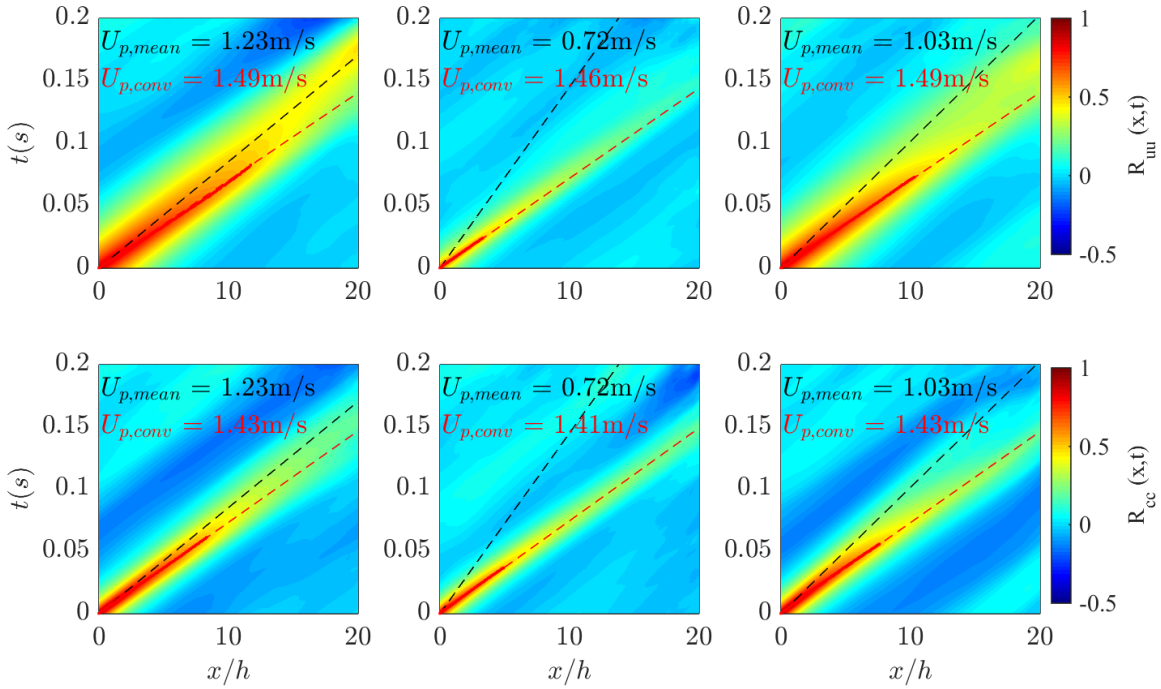

Figure 3.9: Space-time autocorrelation maps for particle velocities (top) and particle concentrations (bottom) for the densest riser case only($\phi_V = 7.7 \times 10^{-3}, Re_{bulk} = 1200$). Plots from left to right are the correlation maps for the left wall, channel center plane and the right wall.

($\phi_V = 7.7 \times 10^{-3}, Re_{bulk} = 1200$) performed for the velocity fields (top) and the concentration fields (bottom), as well as separated by wall-normal location for left wall, center plane and right wall. The correlation maps reveal high-correlation regions that are advected in time for both the velocity and concentration correlations, which could not be observed from the correlation functions in space or time alone. The slope of the highly correlated regions corresponds to a convection velocity of structures in the velocity and concentration fields. For comparison, the equivalent slope for the mean particle velocity is also plotted as a black dashed line across the correlation map.

Comparing the top and bottom plots reveals that the velocity fields are more strongly correlated, and structures persists longer in space-time compared to the concentration fields. The convection velocities of R_{uu} are also higher compared to the convection of R_{cc}, although they are both similar in magnitude and much higher compared to the mean particle velocity. In addition, while the particle velocities range from slower in the center to faster near walls, the convection velocities appear to be similar independent of wall-normal positions. These correlations paint a picture of highly concentrated structures falling faster than ensemble of the particles, with velocities relatively insensitive to the local air flow (which is expected to be moving upward at higher rate in the core of the channel than near the walls). These structures are associated to relatively long wakes, producing larger and longer-lasting footprints in the velocity fields than on the concentration fields.

To compare the effect of concentration and fluidizing airflow on the R_{uu} and R_{cc} fields, correlation maps computed for the left wall are plotted in figure 3.10 for R_{uu} and figure 3.11 for R_{cc}. Re_{bulk} increases from left to right, and plotted in the top row are cases with higher volume fractions which exhibits strong concentration r.m.s. fluctuations ($\phi_V > 5 \times 10^{-3}$) whereas the bottom row are cases with relatively small concentration variance ($\phi_V < 5 \times 10^{-3}$). The convection velocity is determined using the same method as in figure 3.9, and the mean particle velocities are also overlaid on each respective plot. It is now clear that the strongly correlated regions in R_{uu} and R_{cc} correlation fields are associated with high-volume fractions. In figure 3.10, the top row show strong correlations persisting across the space-time domain, in contrast to the bottom row where highly correlated regions ($R_{uu} > 0.5$) are almost non-existent except very near the origin.

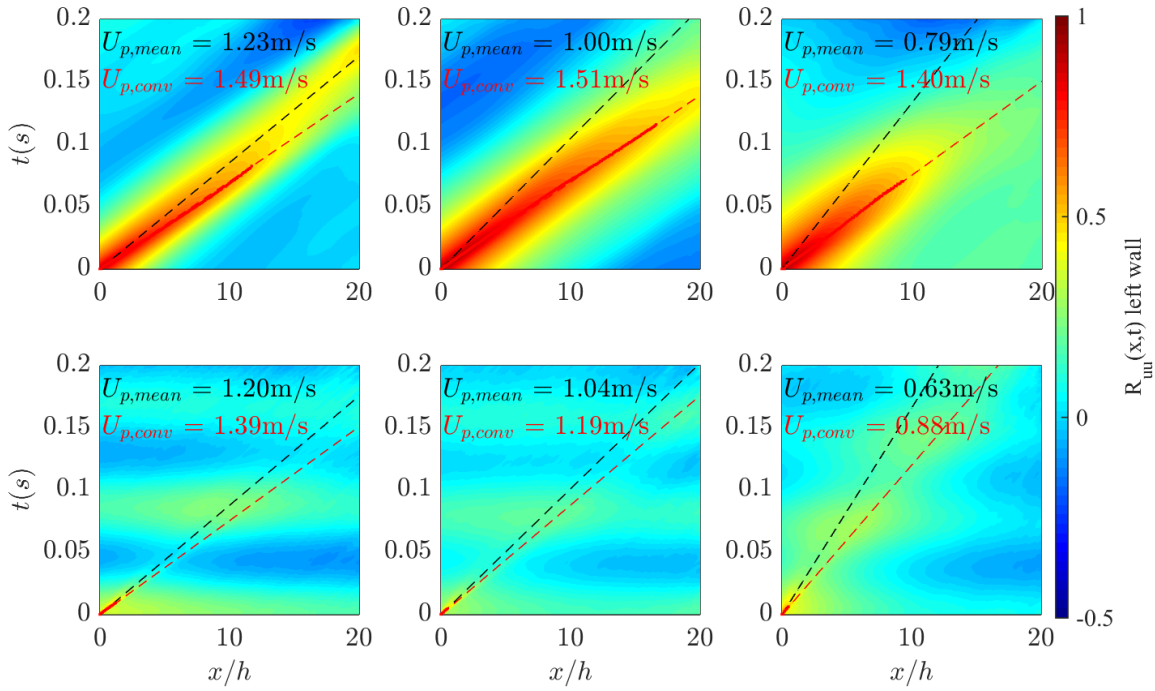

Figure 3.10: Space-time autocorrelation maps for R_{uu}. Plots from left to right is in increasing Re_{bulk} (600, 900, 1200). Plots in the top row are for cases with $\phi_V > 5\times10^{-3}$, and plots in the bottom row are for cases with $\phi_V < 5 \times 10^{-3}$.

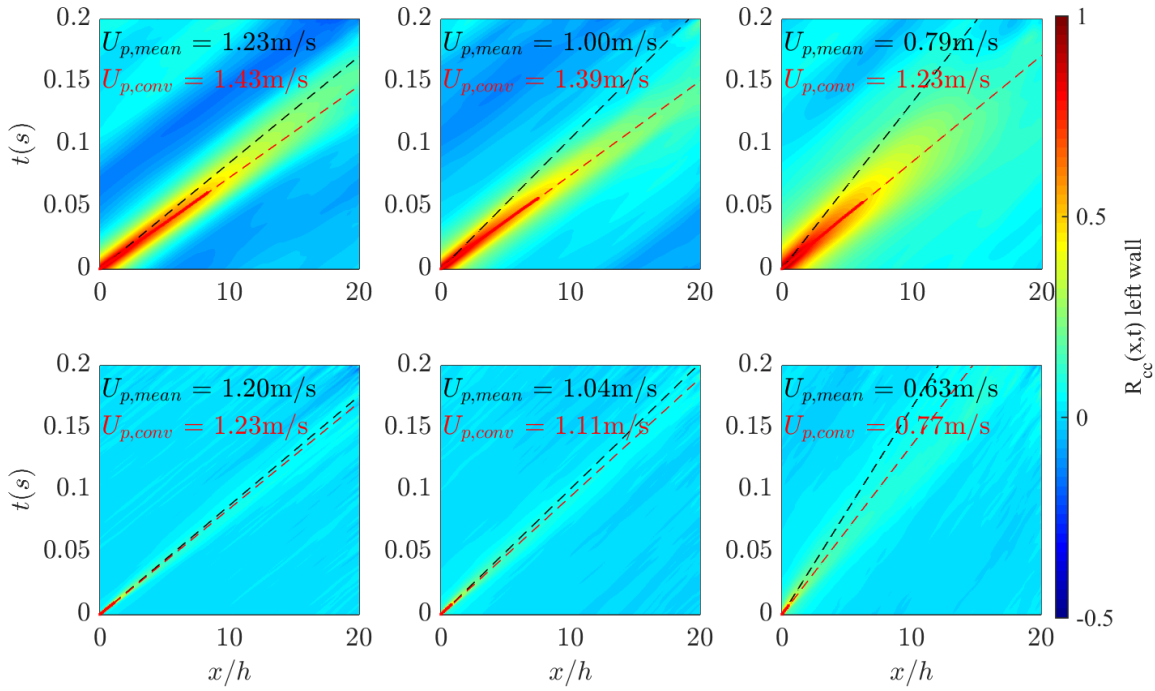

Figure 3.11: Space-time autocorrelation maps for R_{cc}. Plots from left to right is in increasing Re_{bulk} (600, 900, 1200). Plots in the top row are for cases with $\phi_V > 5\times10^{-3}$, and plots in the bottom row are for cases with $\phi_V < 5 \times 10^{-3}$.

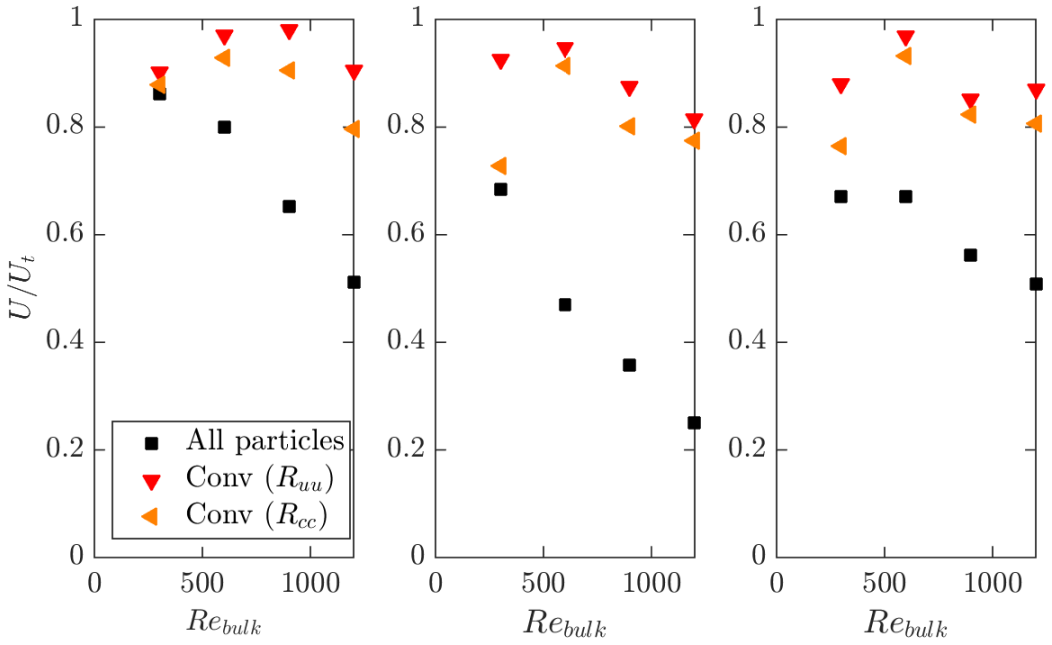

Figure 3.12: Plot of convection velocities and mean particle velocities against bulk fluidizing air velocity, Re_{bulk} for all cases with $\phi_V > 5 \times 10^{-3}$. Plots from left to right refers to velocities for the left wall, channel center plane and the right wall, respectively.

We also note the fact that the fluctuating velocity fields (in figure 3.10) are more strongly correlated than the concentration fields (in figure 3.11), which appears to be independent of Re_{bulk} (in the considered range). A summary plot in figure 3.12 shows that the convection velocities for both the R_{uu} and R_{cc} fields do not vary with Re_{bulk} and wall-normal distances, with the convection velocity for the R_{uu} fields being consistently higher than that of the R_{cc} fields. Interestingly, the convection velocities are also almost equal to the single-particle terminal velocity. This will be addressed and further studied in §3.3.6.

In the low-volume fraction cases, an undulation in the time domain is visible in the R_{uu} fields (figure 3.10) corresponding to a frequency of about 10 Hz, which is the frequency of the blower driving the airflow. This undulation is not observed in the R_{cc} fields (figure 3.11), indicating that particle distributions are not significantly affected by the blower frequency.

3.3.3 Gradient diffusion of particles in riser

Modelling efforts for dispersed particles in fluids range between highly-resolved models that capture the boundary layer around each particle, or kinetic theories that model the dispersed phase as a quasi-continuum (Fullmer & Hrenya 2017). The latter are popular in increasingly dense regimes due to the reduced modelling cost compared to the highly resolved models. The present experimental study features dense volume fractions and particle-phase turbulence generation due to the interaction with the falling particles with the rising air. This provides an avenue for us to check whether classic concepts of continuum behaviour are applicable to the flow field, one of which is the turbulent diffusion of momentum and concentrations.

The gradient diffusion hypothesis for turbulent transport of a passive scalar is well known and often applied in modelling turbulence and deducing turbulent parameters such as the mixing length and eddy viscosity. The basic idea is that turbulent fluxes follow the gradient of mean concentration and velocity, i.e.:

$$\langle uv \rangle = -\nu_t \frac{d\langle U \rangle}{dy}, \tag{3.3}$$

$$\langle vc \rangle = -D_t \frac{d\langle C \rangle}{dy}, \tag{3.4}$$

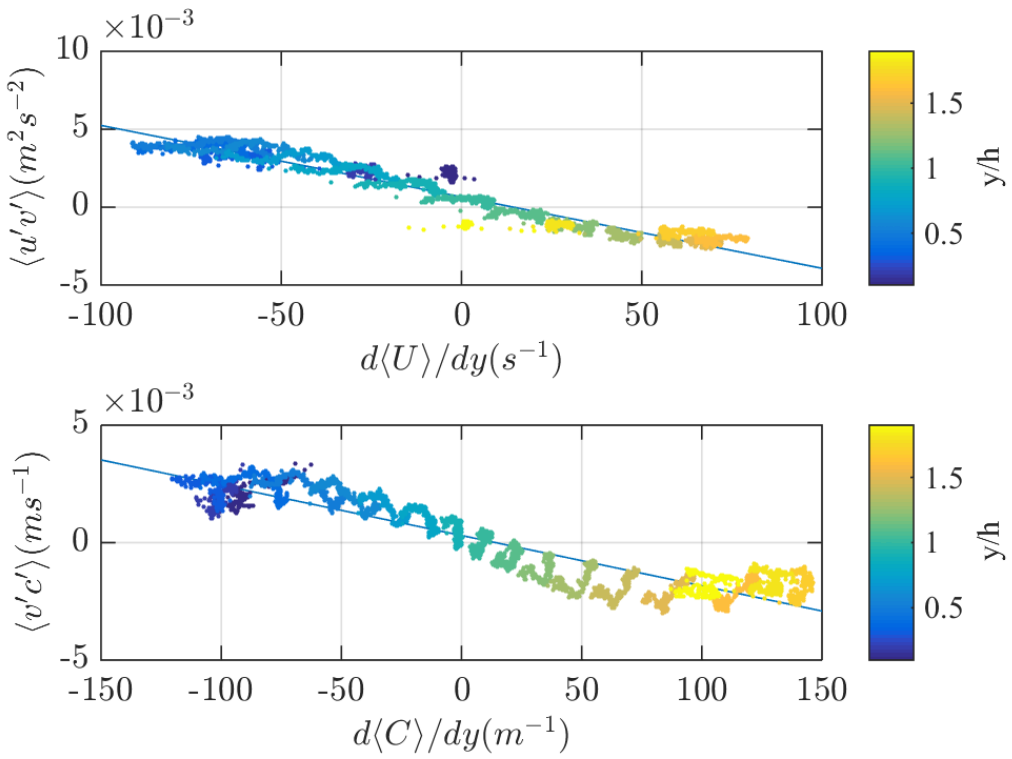

Figure 3.13: Scatter plots of $d\langle U\rangle/dy$ (top) and $d\langle C\rangle/dy$ (bottom) with the linear best fit plotted. This is for the densest riser case ($\phi_V = 7.7 \times 10^{-3}, Re_{bulk} = 1200$).

with 3.3 being the momentum diffusion equation and 3.4 being the mass diffusion equation. u, v and c denotes the fluctuating quantity of streamwise velocity, spanwise velocity and normalized concentration respectively, with the concentration field $C = \phi_V/\phi_{V,mean}$. The covariance $\langle uv \rangle$ is plotted against $d\langle U \rangle/dy$ at all (x, y) location in figure 3.13, showing a trend of linear decrease with the slope value representing the value of the eddy viscosity ν_t. The turbulent diffusivity, D_t is also calculated with the same procedure.

To assess whether the turbulent diffusivity of momentum and mass is captured by the gradient diffusion assumption, we plot the spanwise profile of the turbulent fluxes $\langle uv \rangle$ and $\langle vc \rangle$ and compare them with the model profiles defined by 3.3 and 3.4. This is done for all riser cases across all volume fractions and Re_{bulk}, with the results shown in figure 3.14 for the dense cases and figure 3.15 for the more dilute cases. As observed, the model profile matches well the observed profile for most cases, replicating the $\langle uv \rangle$ and $\langle vc \rangle$ profile in shape as well as in magnitude. Several cases show a large difference between the model and observed profiles, which notably are cases near the threshold $\phi_V = 5 \times 10^{-3}$. All computed values of ν_t and D_t are reported in figure 3.16. In the denser cases, the values of ν_t and D_t have of the order of the kinematic viscosity of air. In the lower volume fraction cases, the corresponding values are an order of magnitude lower; this is clearer in the values of D_t compared to ν_t.

3.3.4 Clustering of particles

With varying mean concentration, we have observed order-of-magnitude differences in the r.m.s. fluctuations of particle velocity and concentration, as well as in turbulent fluxes of mass and momentum. For the denser cases, space-time autocorrelation maps have revealed highly correlated structures of the particle field traveling at large velocities, relatively independent of the fluidizing air flow. This suggest that, as reported in previous riser studies, particle clusters are formed. Here we investigate the clustering phenomenon by detecting clusters and characterizing their geometry, locations, lifetime, velocities, and concentrations.

A widely accepted method to quantify clustering is needed is defined by Fessler *et al.* (1994) through the clustering parameter in classic box-counting, $D = (\sigma - \sigma_{Poisson})/\lambda$, where σ is the standard deviation of the number of particles in each box, $\sigma_{Poisson}$ is the

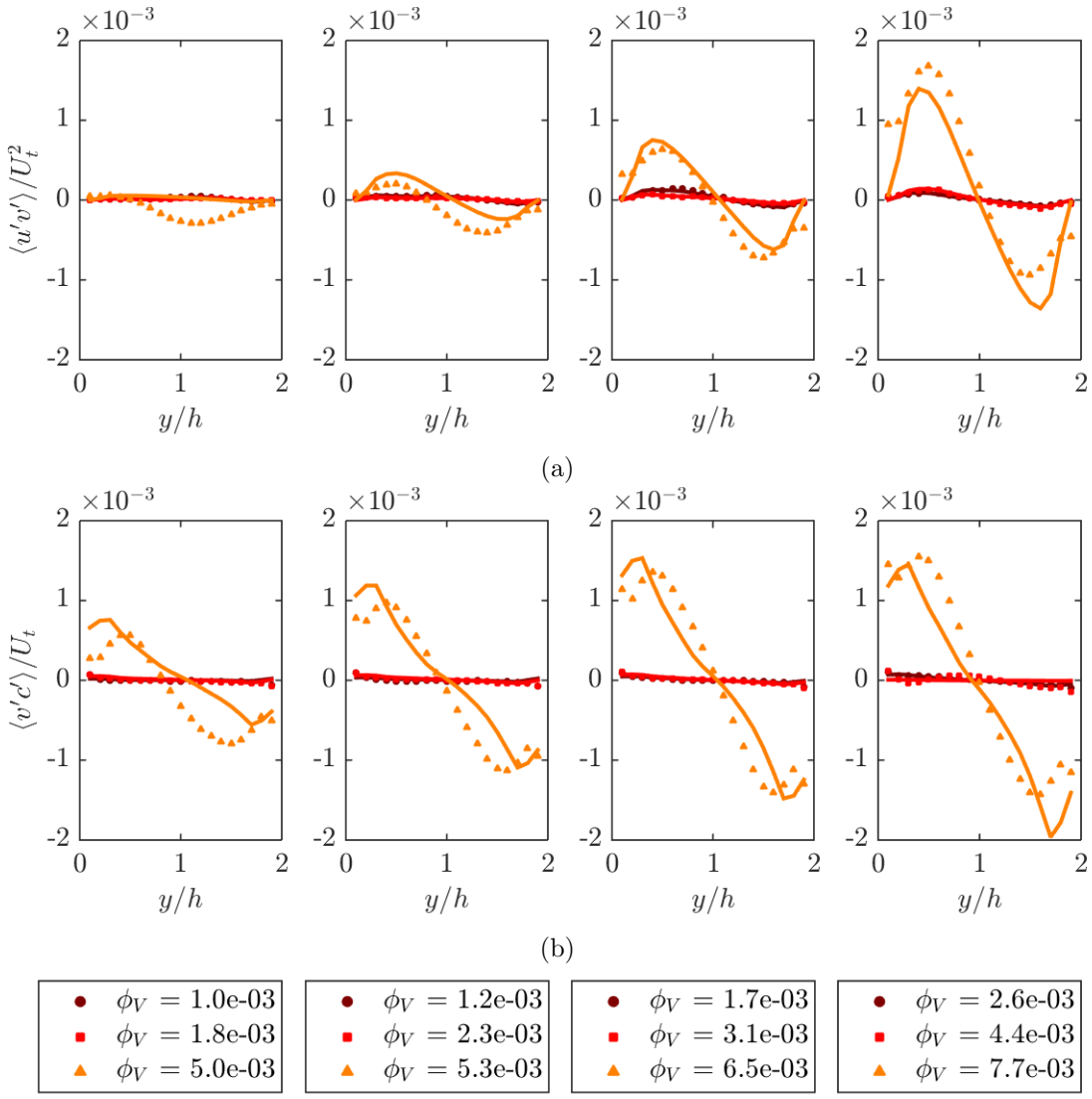

Figure 3.14: (a) Spanwise profiles of $\langle uv \rangle$, plotted as points compared to the model profile $-\nu_t d\langle U \rangle / dy$ plotted as a continuous straight line. (b) Spanwise profiles of $\langle vc \rangle$, plotted as points compared to the model profile $D_t d\langle C \rangle / dy$ plotted as a continuous straight line. For both plots, the colors denote the cases with different volume fractions (shown in the legend). The y-axis is scaled to feature the densest riser cases, which profile has values an order of magnitude higher compared to the more dilute cases.

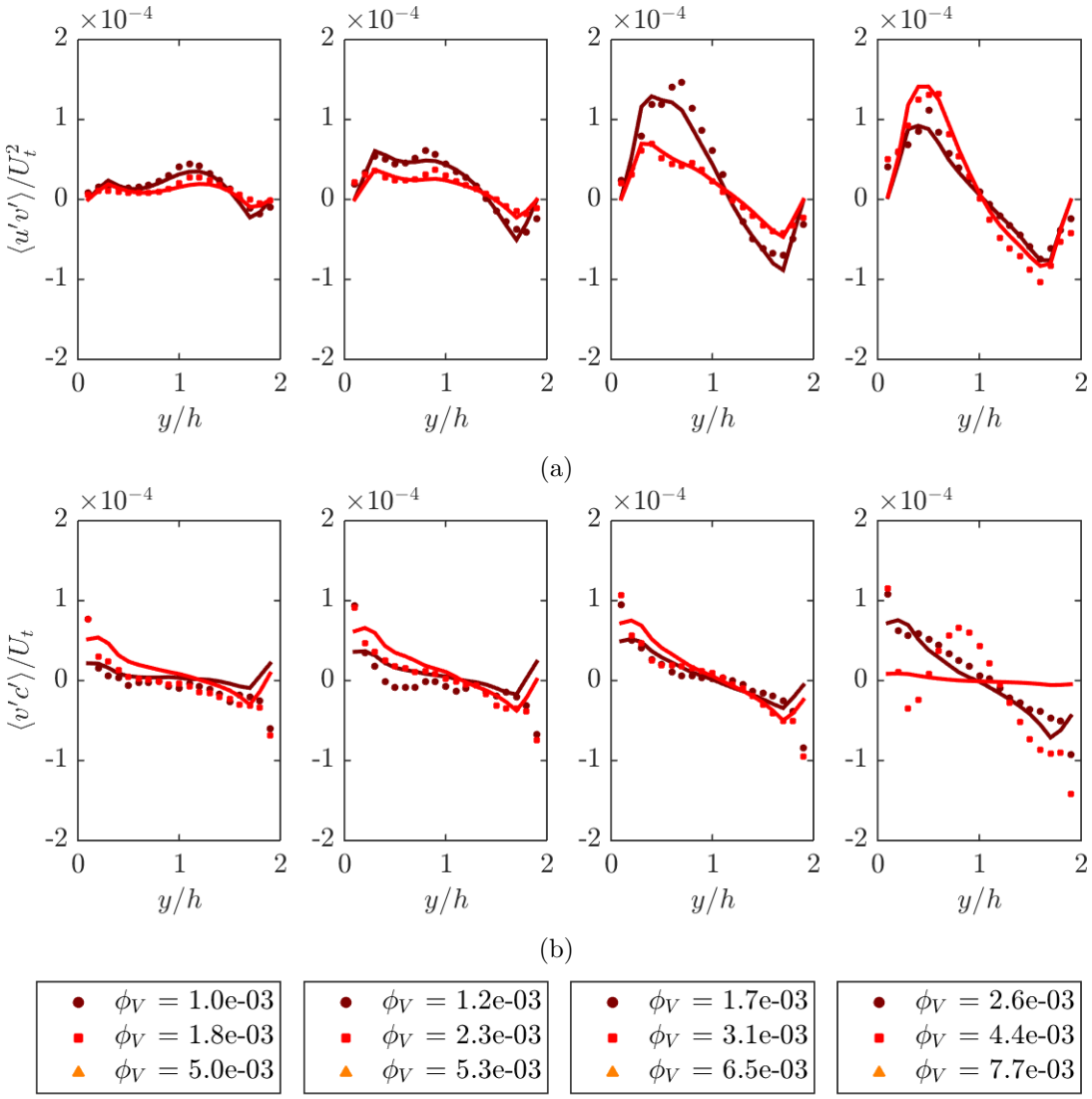

Figure 3.15: (a) Spanwise profiles of $\langle uv \rangle$, plotted as points compared to the model profile $-\nu_t d\langle U \rangle / dy$ plotted as a continuous straight line. (b) Spanwise profiles of $\langle vc \rangle$, plotted as points compared to the model profile $D_t d\langle C \rangle / dy$ plotted as a continuous straight line. For both plots, the colors denote the cases with different volume fractions (shown in the legend). The y-axis is now scaled to feature the more dilute cases.

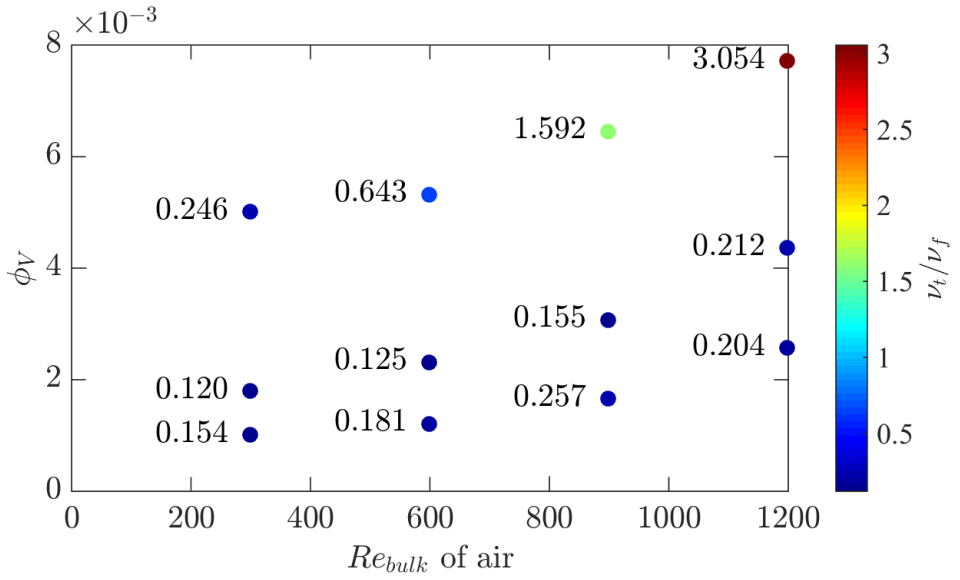

(a)

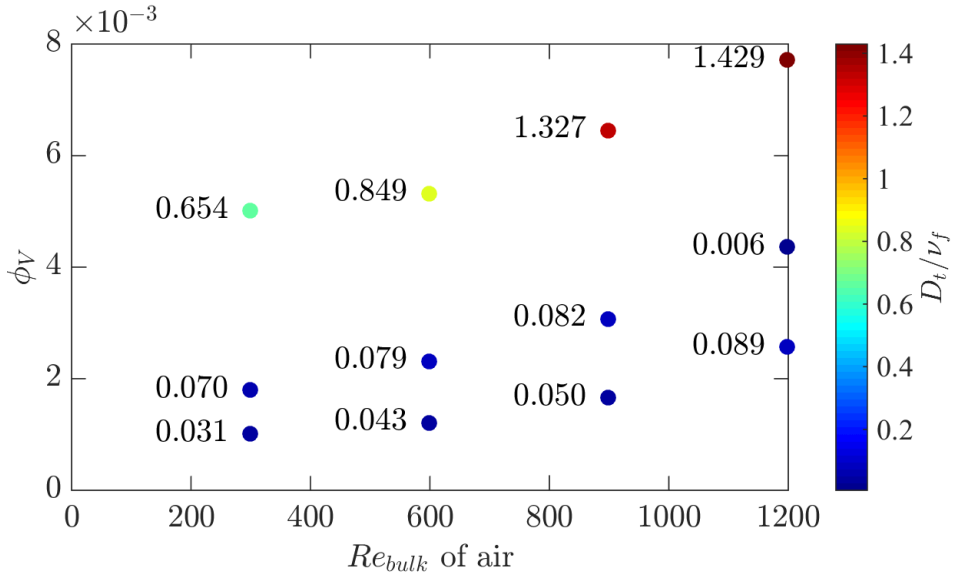

(b)

Figure 3.16: Values of (a) ν_t and (b) D_t represented by the color axis for each experiment in the probed parameter space. The value of (a) ν_t and (b) D_t are also printed beside each point for clarity.

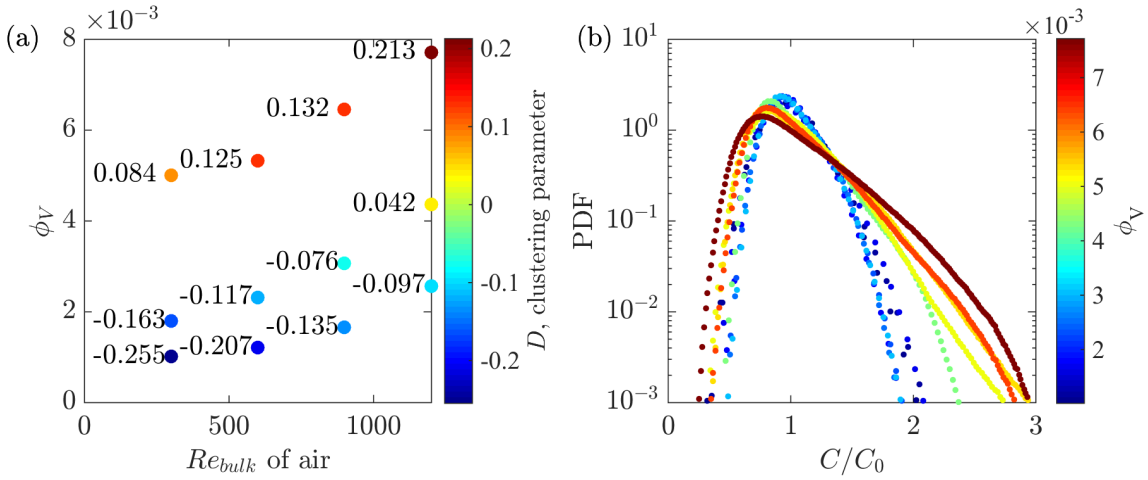

Figure 3.17: (a) The clustering parameter D in the color scale plotted for each case in the parameter space. The value of D is also printed besides the label for clarity. (b) PDFs of relative concentration for all cases, colored by the mean volume fraction.

standard deviations for the Poisson distribution, and λ is the mean number of particles in each box. If the particle distribution is wider compared to that of the Poisson distribution, the parameter D is positive meaning clustering is present and vice versa. This method is intended for cases where the individual particles are identified and binned into boxes. In our case, the 'box' is the PIV interrogation window, and a 'number of particles' count is estimated from the volume fraction, which is in turn determined from the brightness of the image: number of particles = $\phi_V \times$ box size $/V_{particle}$. Applying this procedure to all 12 riser cases, we observe a range of D values as shown in figure 3.17. Positive values of D are observed for all cases with $\phi_V > 5 \times 10^{-3}$. This agrees with our prior observations that above this threshold the concentration fields display greater variance, irrespective of Re_{bulk}.

3.3.5 Cluster identification and tracking

To capture and describe cluster characteristics, an automated cluster detection and tracking solution has to be implemented. Various threshold-based techniques for cluster detection exist in literature, from simple brightness threshold-based detection (Lints & Glicksman, 1993) to thresholds determined by the mean and standard deviation of the volume fraction field (Soong *et al.* 1994, Varas *et al.* 2017). The determination of

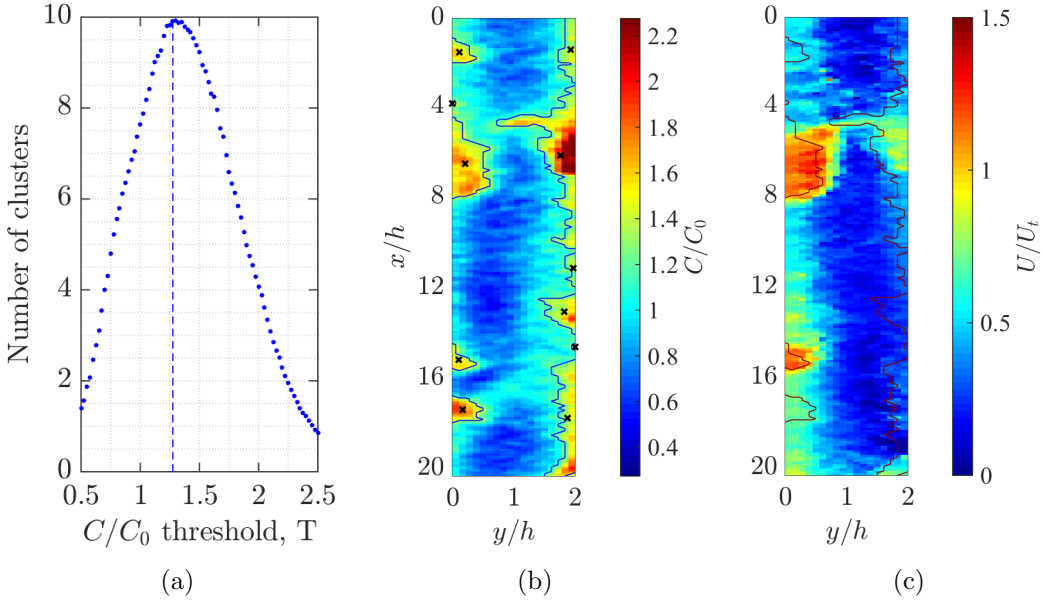

Figure 3.18: (a) Plot of the number of clusters detected with different values of the threshold T, varying from 0.5 C/C_0 to 2.5 C/C_0. (b) A snapshot of the concentration field normalized by the mean concentration. The contour lines indicate regions where the concentration exceeds T = 1.275 C/C_0, and black crosses indicate the centroids of the detected clusters. (c) A snapshot of the velocity field of (b), with the contour lines overlaid over the velocity field as well. All these plots are shown for the densest riser case ($\phi_V = 8 \times 10^{-3}$, $Re_{bulk} = 1200$).

the threshold is important due to the wide dynamic range of volume fractions in these flows. An underestimated threshold will lead to detection of false clusters, whereas an overestimated threshold will miss clusters.

To this end, we implement the percolation method, which has been used in turbulence studies to identify turbulent flow structures based on the vorticity and strain rate fields (Moisy & Jiménez, 2004). The percolation method has also been used in finding structures in the Q-criterion field (Carter & Coletti 2018) and clusters of falling snowflakes in the atmosphere (Li *et al.* 2021*a*) which is most similar to our application of this method. This method works by binarizing the concentration field at an arbitrary threshold T. A search for connected units in the binary field is then performed, and the total number of connected units (i.e. clusters) is recorded for different values of T. Varying the value of T will change the number of clusters, from one large "super-cluster" when the threshold is low, to few small clusters when the threshold is high. Finally, the threshold value T that results in the highest number of clusters detected is chosen. This allows determination of a threshold without need for user input, and also shows that small variations in the threshold does not drastically change the clusters that are detected using the method (figure 3.18a). Once a suitable threshold is determined, the concentration fields are processed to identify the clusters present in each frame and their centroids. A sample snapshot of the clusters identified by this method is shown in figure 3.18b and 3.18c, where figure 3.18b shows the overlay of the cluster boundaries over the concentration field and their associated centroids; 3.18c shows the overlay of the cluster boundaries over the streamwise velocity field.

Leveraging the time-resolved dataset, clusters can be tracked to determine their lifetimes (the time from their appearance to their termination). This is done by using a nearest-neighbour algorithm applied to the centroids of the clusters. A cluster is terminated when its centroid is not found at close proximity in the subsequent frame, having dissipated into concentrations lower than the threshold T. Alternately, it may have undergone a merging or breaking event, and its shape has changed dramatically such that the centroid had a very large displacement. An additional tracking step is applied at the end of each cluster track to capture this dynamic, of which details are elaborated upon in Appendix B. This additional step enables tracking of merging clusters, breaking clusters, and very large clusters that exhibits large changes in their

shapes and centroid locations over their lifetime.

An additional criterion for cluster identification is that each cluster such persist for an extended time (lifetime), beyond random fluctuations of the concentration field. In the present range of volume fraction, the latter is expected to exhibit small-scale fluctuations in space and time associated to the mean free path between particle collisions, $\lambda_p = 1/(\sqrt{2}\pi d_p^2 N_V)$, where d_p is the diameter of the particles and N_V is the number of particles in a $1m^3$ volume. From the mean free path, a timescale is derived using $t_p = \lambda_p / U_{p,rms}$ using the ensemble mean particle r.m.s. velocity. Clusters with lifetimes shorter than t_p are discarded. For the densest riser, t_p is calculated to be 11.0 ms. This is 14 times smaller compared to the individual particle response time (155 ms), implying that particle collisions occur well before the particle velocities adjust to the airflow fluctuations.

3.3.6 Cluster characteristics in the densest riser case

When clusters are tracked, instantaneous cluster data and data averaged over its lifetime are available for statistical analysis. For example, a cluster with a lifetime of 72 frames will have 72 instantaneous information, compared to a mean cluster data averaged over its lifetime. This is important to distinguish as both carry different information: as clusters evolve in time, their areas (and other characteristics) may change drastically, which is not reflected if only the mean area over time is considered. Therefore, in the following results, most statistics are compiled based on all cluster instances. The mean cluster statistics are used only when a cluster characteristic is compared against its lifetime, and an overbar is denoted when the lifetime-averaged data is used.

In the densest riser case ($\phi_V = 7.7 \times 10^{-3}$, $Re_{bulk} = 1200$), a total of 192565 cluster instances are found, resulting in 1512 clusters being tracked over their lifetimes; this case shows trends representative of the clustered cases exhibiting clustering ($\phi_V > 8 \times 10^{-3}$). In figure 3.19a, the cluster area PDF shows a peak at $0.3D^2$, and up to 20% of the clusters are as large as the channel cross-section. Figure 3.19c shows a wall-normal profile of the centroid locations of found clusters, showing that clusters are found to exist mostly near the walls of the channel, agreeing with observations from other experiments in rectangular channels (e.g. Varas *et al.* 2017).

For the mean concentrations of the clusters, a similar plot of their distribution

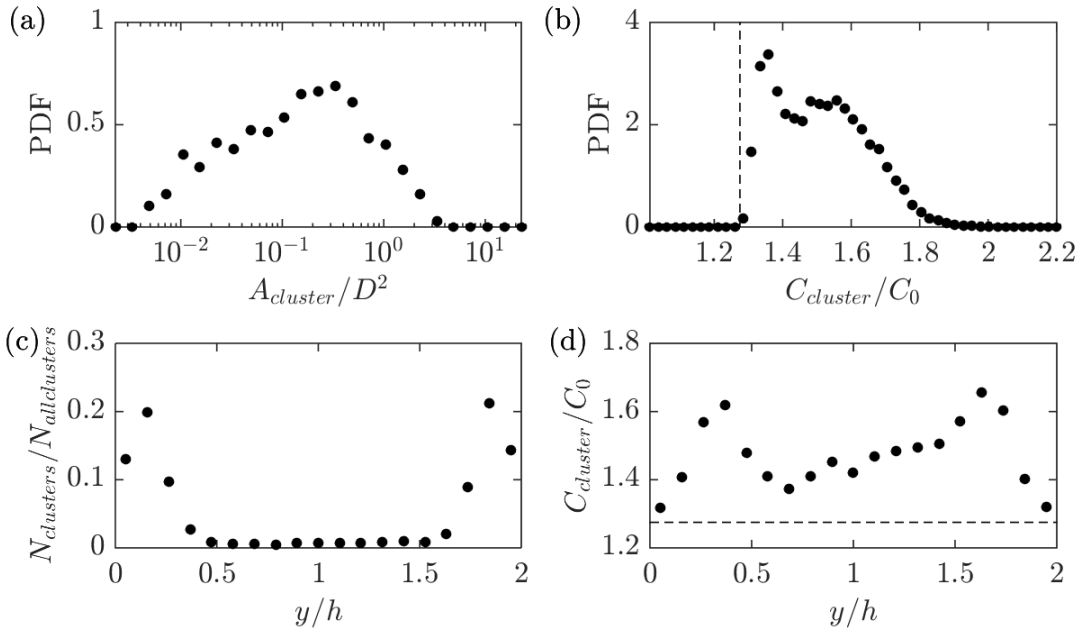

Figure 3.19: For the densest riser case, (a) the PDF of the cluster areas normalized by the channel cross-section. (b) PDF of the cluster concentrations normalized by the mean concentration, with the vertical line denoting the percolation threshold T. (c) Profile of number of clusters binned in the spanwise direction. (d) Profile of cluster concentrations binned in the spanwise direction, with the horizontal line denoting the percolation threshold T.

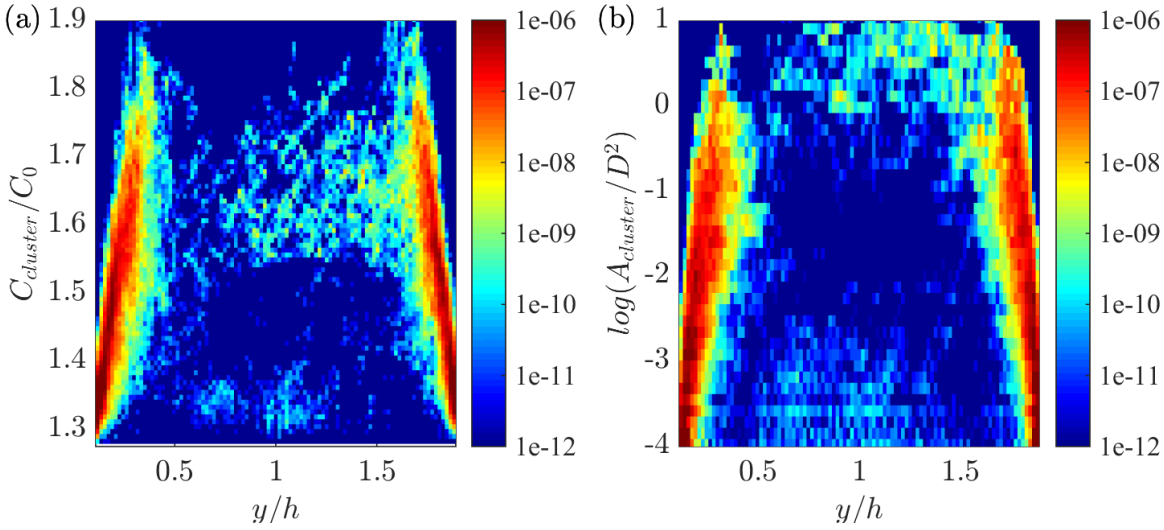

Figure 3.20: (a) A joint PDF of the normalized cluster concentration against its wall-normal location. The logarithmic color axis indicates the frequency in which a cluster appears in said wall-normal location, e.g. clusters with $C/C_0 < 1.44$ are mostly found near the wall. (b) A joint PDF of the cluster area normalized by D^2, plotted logarithmically in the y-axis, against its wall-normal location.

PDF is shown in figure 3.19b, which exhibits a bimodal distribution with peaks at 1.3 and 1.6 C/C_0. Not observed in the area PDF, this hints at different cluster features near the walls compared to in the channel center. Indeed, plotting a JPDF of cluster concentration against their centroid locations reveals the source of the bimodal peaks in the concentration PDF, which is shown in figure 3.20. Small, less dense clusters dominate very near the wall and contribute to the first peak in the PDF. Whereas, in the channel center, clusters of mean 1.6 C/C_0 in concentration exists sporadically and contribute to the second peak in the concentration PDF. They also account for the mean C/C_0 profile being flat at around 1.4 C/C_0 in the center, as shown in the profile of mean cluster concentrations across the channel in figure 3.19d.

The JPDF shown in figure 3.20a shows a trend of clusters growing denser as the distance from the wall increases. The concentrations in these clusters increases up to 1.7 C/C_0, although this growth is limited to the near-wall region of up to 0.5 y/h away from the wall. A similar JPDF plotted for the cluster areas in figure 3.20b also shows that the cluster areas are also increasing away from the wall. This suggests that

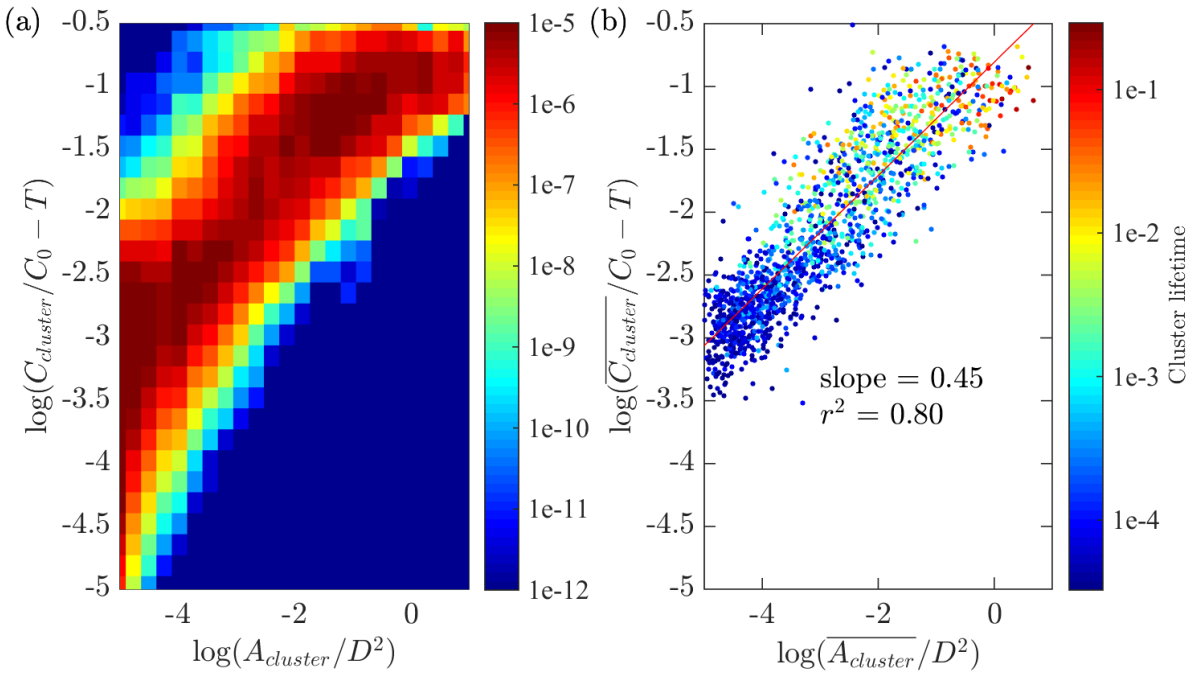

Figure 3.21: (a) A joint PDF of the cluster concentrations against the normalized cluster areas. (b) A scatter plot of the mean cluster concentration against the mean cluster areas, averaged over the cluster lifetime. The color of the symbols indicate the lifetime of the clusters.

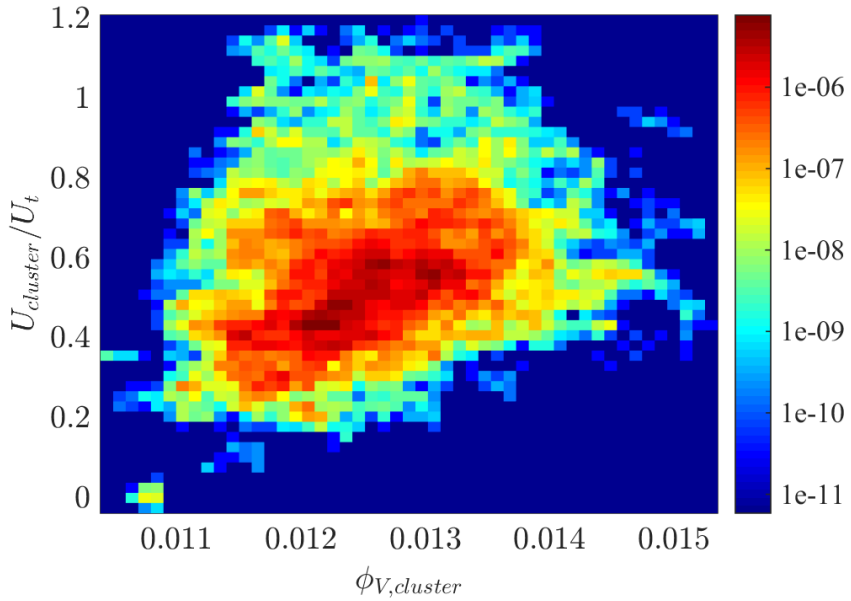

Figure 3.22: A joint PDF of the cluster volume fractions against the cluster velocity normalized by U_t.

clusters are growing by incorporating more particles, rather than dilating and becoming more dilute. To this end, we compare the cluster concentrations directly against the cluster area in figure 3.21, for both the instantaneous cluster realizations as well as the mean cluster statistics over its lifetime. We observe a power-law relationship in both plots, with a linear fit in figure 3.20b indicating that the cluster concentration grows proportional to the square root of the area. In figure 3.20b, the color of the scatter points also indicates the lifetime of the cluster, which is also shown to increase with both size and concentration.

Figure 3.22 features a joint PDF of the cluster volume fractions against the cluster velocity for the densest riser case, showing a trend where denser clusters are also falling faster in the channel. This summarizes the nature of the clusters: clusters with longer lifetimes are likely to have larger area and larger concentration, the cluster concentration grows proportional to the square root of the area (that is, approximately linearly with the cluster size), and that the denser clusters fall faster.

At this point it is important to keep in mind that the imaging technique employed

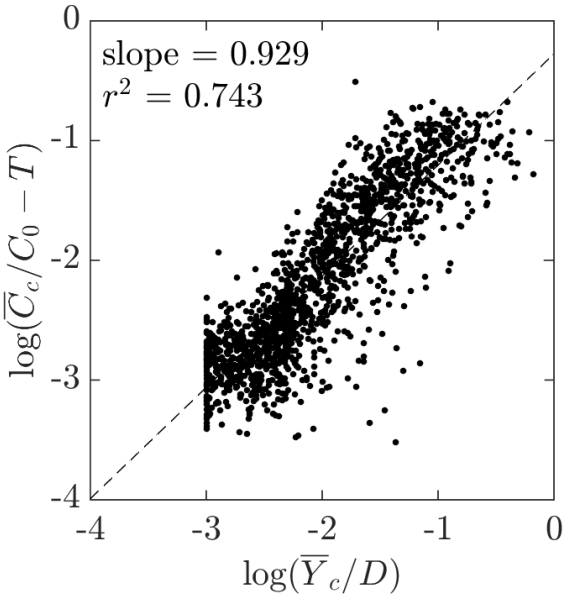

Figure 3.23: Scatter plot of mean cluster concentration against the mean cluster width in the spanwise direction.

results in a concentration field that is optically depth-averaged. What we observe here as the increase in cluster concentration, could be a result of the cluster growing in the direction perpendicular to the imaging plane, thus appearing denser because of the back-lighting. A way to investigate this point is to compare the cluster mean concentration against the cluster width, i.e. its size in the y-direction, which is expected to be similar to that in the z (depth) direction. As shown in figure 3.23, a nearly linear relationship is observed between the cluster span and the concentration. This result lends support to the hypothesis that the increase in concentration is due to the depth-wise growth of the cluster.

3.3.7 Cluster characteristics across all riser cases

Cluster detection and tracking are performed on all riser cases which clustering is observed, using their respective values of the percolation threshold T, and the minimum timescale for clusters, t_p. Values of the thresholds as well as the resulting number of clusters detected and tracked are shown below in Table 3.2.

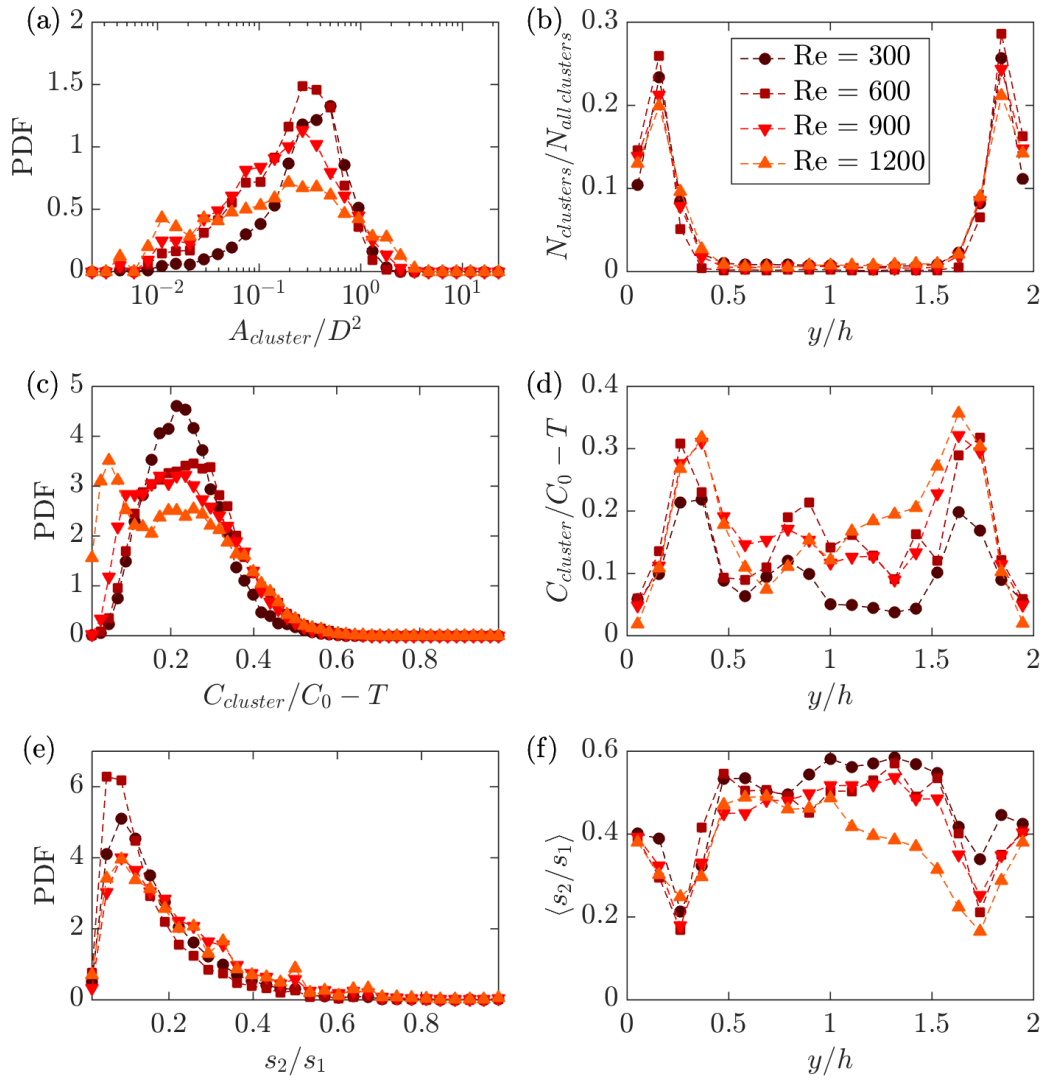

Figure 3.24: For all clustered riser cases, (a) the PDF of the cluster areas normalized by the channel cross-section, (b) profile of number of clusters binned in the spanwise direction, (c) the PDF of the cluster concentrations, normalized by the mean concentration C_0 and subtracted with the percolation threshold T for each case, (d) profile of cluster concentrations binned in the spanwise direction, normalized by C_0 and subtracted with T for each case, (e) the PDF of the cluster aspect ratios for all cases, and (f) profile of the mean cluster aspect ratio binned in the spanwise direction for all cases.

Re_{bulk}	Percolation threshold, T	Particle timescale (ms)	No. of cluster instances	No. of clusters tracked
300	1.225	41.8	141278	371
600	1.3	30.3	170617	752
900	1.225	20.6	204464	906
1200	1.275	11.0	192565	1512

Table 3.2: Values of percolation threshold and the particle timescale threshold used, and the resulting number of cluster instances detected, and number of clusters tracked for each riser case.

Figure 3.24 compares the characteristics of clusters detected for all riser cases. Across all cases, the cluster area PDFs show a peak near $0.3D^2$, with some clusters having areas equal to or larger than the channel cross-section. As the strength of the fluidizing air increases, the peak height of the area PDF decreases, showing that fluidization increases the range of cluster sizes. However, the range of areas are similar across all cases and are likely to be limited by the channel geometry. Clusters are also found to exist mostly near the walls of the channel, with a distribution similar to the densest riser case.

Comparison of cluster concentrations between cases are made more complicated due to the different thresholds used as determined by the percolation method. Nevertheless, it is shown in figure 3.24c that a wide range of cluster concentrations are observed, with a maximum of up to 0.6 C/C_0 above the percolation threshold. The bimodal distribution that was observed for the densest riser case is also less pronounced in the lower Re_{bulk} cases. This may be influenced by the increased cluster timescale threshold, which filters out more of the small and short-lived clusters. Comparing the wall-normal profiles of the mean cluster concentrations in figure 3.24d, we also observe the increase in cluster concentrations in the first 3 data points similar to results shown in the JPDF in figure 3.20. In the channel center, the relatively few clusters detected show a constant cluster concentration, with mean concentration up to 0.2 C/C_0 above the percolation threshold.

Finally, figure 3.24e shows the PDF of the cluster aspect ratios calculated as a ratio of s_2/s_1, with s_1 being the length of the larger principal axis of the cluster and s_2 being the smaller principal axis. The limit values 0 correspond to an infinitely thin and long

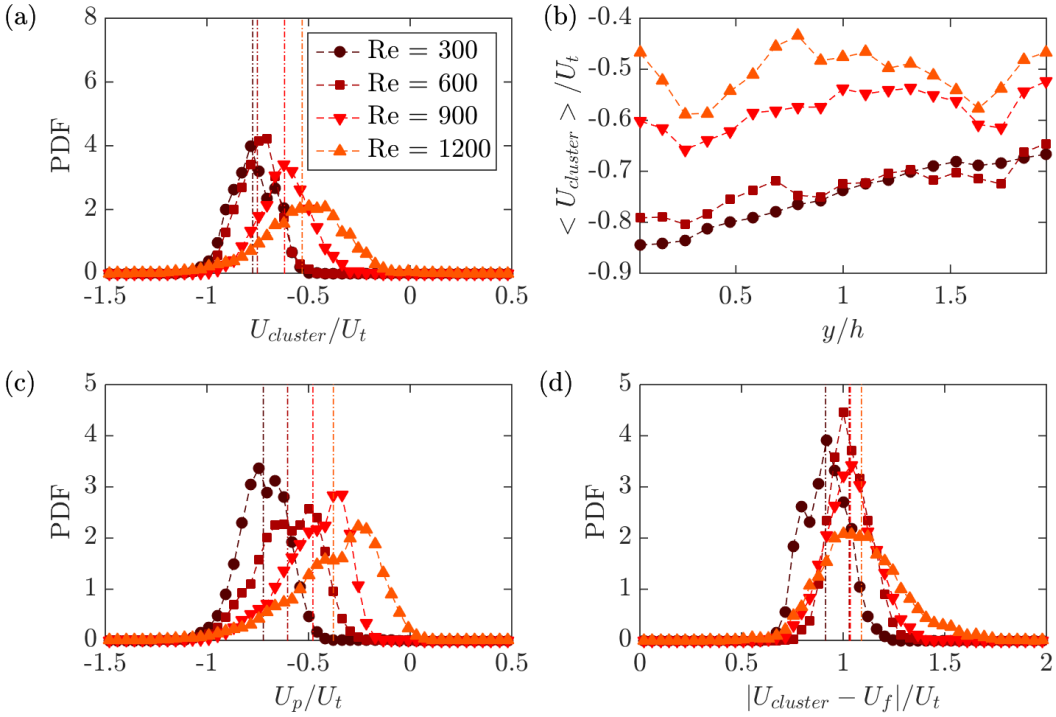

Figure 3.25: For all clustered riser cases, (a) the PDF of the cluster velocities normalized by U_t. (b) Profile of the mean cluster velocities binned in the spanwise direction. (c) the PDF of the global particle velocities normalized by U_t. (d) PDF of the cluster slip velocities normalized by U, t for all clustered riser cases. For (a, c, d), vertical lines denote the mean of the PDF for each case

cluster, and 1 corresponds to a square or circular cluster with $s_1 = s_2$. Here it is shown that for all riser cases the clusters are elongated. Figure 3.24f also shows a minimum mean aspect ratio in the 3rd bin from the walls, corresponding to the peaks in mean cluster concentrations as shown in figure 3.24d.

Figure 3.25 compares the cluster descent velocities, $U_{cluster}$, tracked via their centroids for all riser cases. As shown in the PDF of the cluster descent velocities in figure 3.25a, clusters fall more slowly on average as the strength of the fluidizing air increases. In addition, the spread of the velocities becomes larger, which is attributable to the larger range of cluster areas resulting from the stronger rising air. In figure 3.25b, the wall-normal profiles of the cluster descent velocity show an asymmetry from left to right

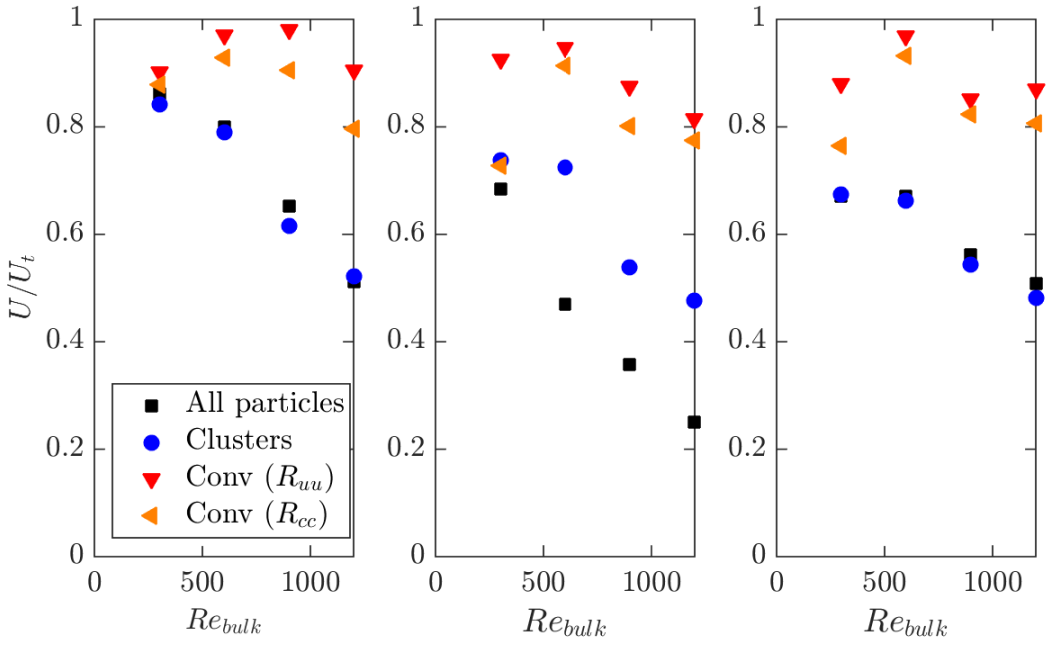

Figure 3.26: Plot of mean particle velocities, cluster velocities and convection velocities against bulk fluidizing air velocity, Re_{bulk} for all cases with $\phi_V > 5 \times 10^{-3}$. Plots from left to right refers to velocities for the left wall, channel center and the right wall, respectively.

for the lower Re_{bulk} cases, consistent with the weak asymmetry in certical velocity shown in figure 3.5. In contrast, for the high Re_{bulk} cases with stronger mixing, the cluster descent velocities are independent of their wall-normal position. Considering that most clusters are found near the wall as shown in figure 3.24c, one can deduce that clusters in the 'center' are most likely near-wall clusters as well, forming near the front and back wall. This may explain why cluster descent velocities appear to be independent of their y-axis locations.

Figure 3.25c shows the PDF of the global particle velocities normalized by U_t. Comparing the means of each PDF in figure 3.25c to figure 3.25a, we observe that the clusters on average are falling faster than the global particle velocity. In addition, we compare the cluster velocities and the global velocities to the convection velocities from the space-time autocorrelation plots in §3.3.2 as shown in figure 3.26. At the walls, the clusters and the particles show similar velocities, which is expected as clusters primarily form

near the walls and particles near the walls are often part of a cluster. Clusters are less frequent in the channel center, and thus the difference in clusters velocities and the global particle velocities are more distinct. It is also shown that the cluster velocities are still slower compared to the convection velocities for both the velocity and concentration fluctuation fields. We suspect that in the space-time autocorrelation analysis, denser clusters have a stronger influence on the value of R_{cc}, The higher value of R_{cc} also means the denser clusters are falling faster, which is corroborated by the JPDF in figure 3.22. In overall, the velocities of the percolation-defined clusters are similar or higher than the global particle velocity, but the convection velocities which are weighted by the denser clusters appear even higher.

Finally, we compare the cluster descent velocities to a model proposed by Noymer & Glicksman (2000). In their paper, they study large particle riser experiments and collect empirical data of cluster descent velocities at the near-wall region, comparing them to permeability and aerodynamic drag models for the clusters. They show that both drag models influence the cluster velocities, but the influence of permeability drag is stronger. Their model equation, $U_{cluster} = 0.75\sqrt{(gd_p\rho_p)/\rho_f}$, depends only on the intrinsic properties of the particles and fluid, i.e. the particle and fluid density, and the particle diameter. Essentially, all riser cases will have the same cluster descent velocity, which in our experiment $U_{cluster} = 1.56\ m/s$, or nearly unity with U_t. This contradicts the results shown in figure 3.25a, where the mean cluster velocities are obviously decreasing with increasing Re_{bulk}. However, we can calculate a rough estimate of the cluster slip velocities against the rising air by $U_{slip} = |U_{cluster} - U_f|$, where U_f is the bulk velocity of the rising air in the channel. Plotting the PDF of the cluster slip velocities results in all riser cases showing a mean slip velocity that is close to U_t, as shown in figure 3.25d. We note that the Noymer-Glicksman model was devised for large risers ($D/D_p > 10^3$) where the clusters are expected to be embedded in the near-wall boundary layers (although full three-dimensional concentration measurements are lacking); there the upward air flow velocity is relatively small. In our case, on the other hand, the clusters stretch relatively deep in the core of the duct, and therefore the importance of the upward airflow in determining $U_{cluster}$ is not unexpected.

Bulk Reynolds number, Re_{bulk}	300	600	900	1200
Air density, ρ_f (kg m^{-3})	1.2			
Air kinematic viscosity, ν (m^2 s^{-1})	1.5×10^{-5}			
Channel half width, h (mm)	10.5			
Bulk flow velocity, U_{bulk} (m s^{-1})	0.214	0.428	0.642	0.856
Particle volume fraction, ϕ_V ($\times 10^{-3}$)	1.0	1.2	1.7	2.6
Particle density, ρ_p (kg m^{-3})	2500			
Mean diameter, d_p (µm)	212			
Particle response time, τ_p (s)	0.155			
Particle terminal velocity in still air, V_t (m s^{-1})	1.52			
Particle Reynolds number in still air, Re_p	21.5			
Galileo number, Ga	29.4			

Table 3.3: Fluid and particle parameters for the zoomed-in cases.

3.4 Zoomed-in measurements

The following section details zoomed-in measurements conducted on the particle riser using the same setup as described in figure 3.1. The parameter space explored is the most dilute non-clustered cases, which allows imaging of the center-plane without being obscured by particle clusters. Table 3.3 shows the fluid and particle parameters for the zoomed-in measurements, which is identical to table 3.1 with the additional information of only one particle volume fraction for each Re_{bulk} case.

3.4.1 Imaging and particle detection procedure

For the zoomed-in setup, the imaging setup (figure 3.27a) is similar to that of the zoomed-out setup with the only difference being the use of a 200 mm lens instead (Nikkor, aperture f/4) to achieve higher magnification. The camera is at a standoff distance of 1.5 m, imaging 30.6 mm streamwise, or about 1.5 channel widths. This magnification level (31.3 pixels per mm) allows individual particles to be resolved (figure 3.27b, figure 3.28), appearing as annular rings when they are in focus. The particle identification procedure is as follows:

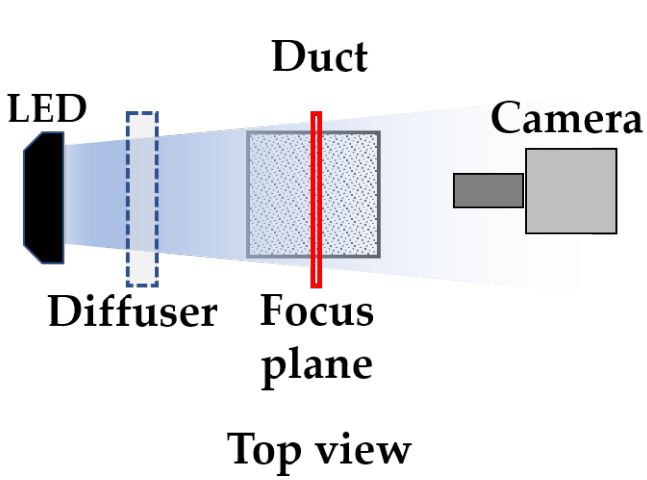

(a)

(b)

Figure 3.27: (a) Imaging setup of the zoomed-in experiment as viewed from the top of the facility. (b) A sample raw image as imaged by the camera.

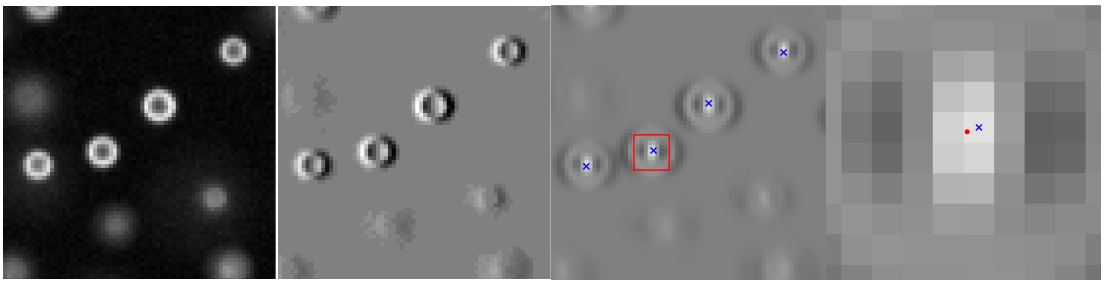

(a) (b) (c) (d)

Figure 3.28: A sequence of images illustrating the particle identification procedure from steps (i) through (iv). Frame (d) shows the difference of the peak-locked centroid (blue cross) and the subpixel centroid (red circle) for the particle shown in the red box in frame (c).

i. The image is inversed, and background subtraction is performed to remove lighting artifacts.

ii. The gradient of the image is computed, where the particles in focus are more easily distinguished due to their sharpness.

iii. A sample particle that is visually determined to be well-focused is chosen, and its image is cross-correlated across the gradient image to obtain a correlation intensity map. A peak-finder algorithm is applied to find local maxima in the cross-correlation map, shown as blue crosses in figure 3.28c. At this stage the maxima location is 'peak-locked', i.e. the particle centroid is constrained to integer pixel values.

iv. A 3-point Gaussian fit is applied to the correlation intensity map around the local maximum to obtain a subpixel peak location, yielding sub-pixel accuracy in the particle centroid. The sub-pixel centroid location is plotted as a red dot in figure 3.28d.

Using this particle identification method, the depth-of-field is experimentally determined by traversing a pair of transparent slides sandwiching sparse glass particles across the depth of the channel. The depth-of-field is determined to be approximately 2 mm as shown by the particle count at various depths (Figure 3.29).

For each experimental condition, 20000 time-resolved images are taken at an acquisition frequency of 4300 Hz, for a total recording time of 4.6 seconds. This frequency enables accurate particle tracking, with a mean vertical displacement of 9 pixels (less than one particle diameter) observed in the weakest riser case (for which the particles fall the fastest). Particle tracking is performed using the "4th-best estimate" method proposed by Ouellette *et al.* (2006), which considers the acceleration history of a particle. At the relatively large concentration considered, this method is more suitable than conventional nearest-neighbor approaches.

Differentiating the data to calculate velocities and accelerations amplifies measurement noise. To mitigate it, we follow an approach proposed by Voth *et al.* (2002) and Mordant *et al.* (2004), and used in several studies of inertial particles in turbulence (e.g., Gerashchenko *et al.* 2008, Nemes *et al.* 2017). The method involves convolving a

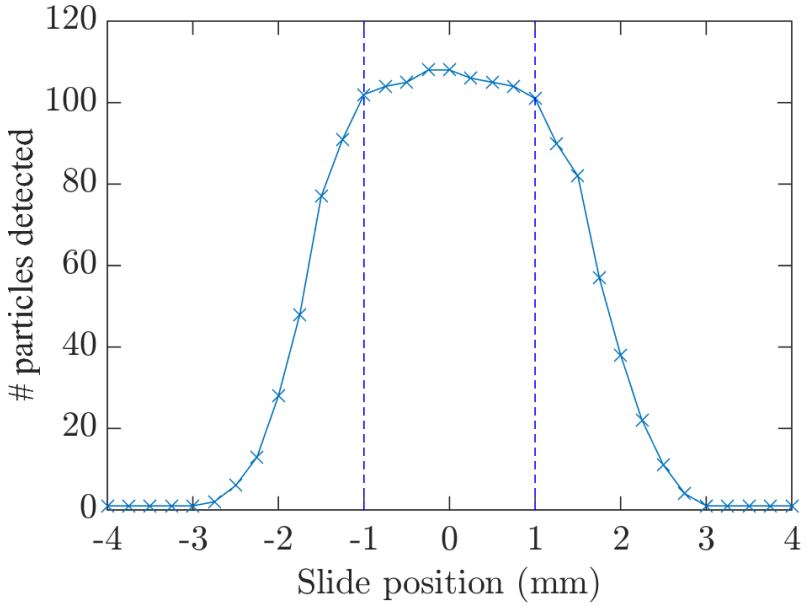

Figure 3.29: Plot of number of particles detected on the microscopic glass slide against the slide position, showing the depth-of-field achieved by the imaging setup.

Gaussian kernel over the particle trajectory, which acts both as a numerical derivative and a low-pass filter. A suitable kernel must be determined – an undersized kernel will not effectively remove all the noise, and an oversized kernel will damp true fluctuations in the particle tracks. Figure 3.30 shows, for a representative case, the ensemble acceleration variance across all particle tracks, $\langle a_x^2 \rangle$, versus the kernel size τ_k varying from 3 to 30 frames. Following the above-mentioned studies, we choose the first τ_k beyond which the acceleration variance decreases exponentially. The is determined to be 19 frames for the Re_{bulk} = 300 - 900 cases, and 20 frames for the Re_{bulk} = 1200 case. Figure 3.31 shows, along a sample trajectory, the reduction in measurement noise from the application of the Gaussian smoothing kernel, without which the velocity and acceleration exhibit unphysical oscillations due to the uncertainty on the particle centroid.

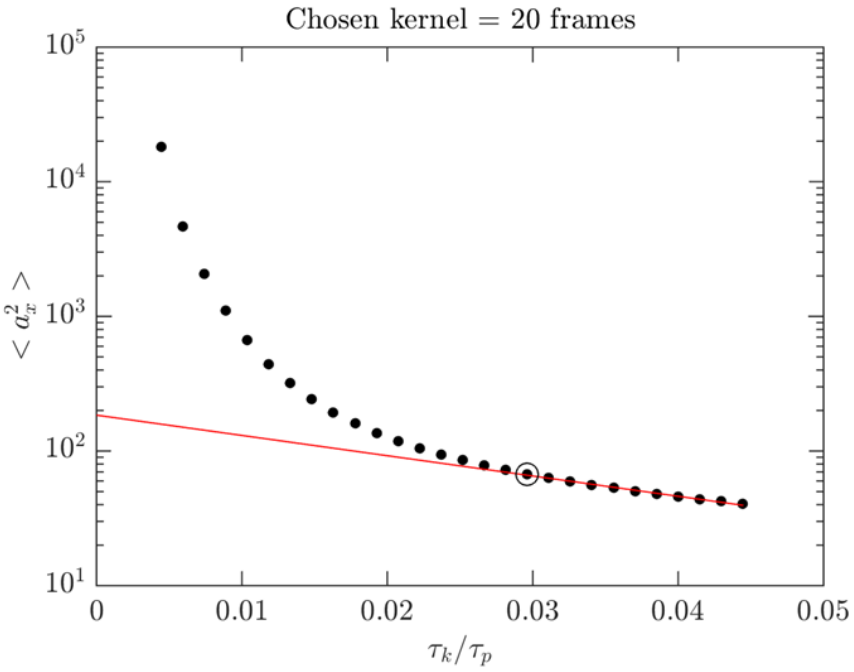

Figure 3.30: Plot of acceleration variance against the timescale of the applied kernel width, τ_k, normalized by the particle response time τ_p. The red line represents the exponential fit, and the final applied kernel width is denoted by the open circle.

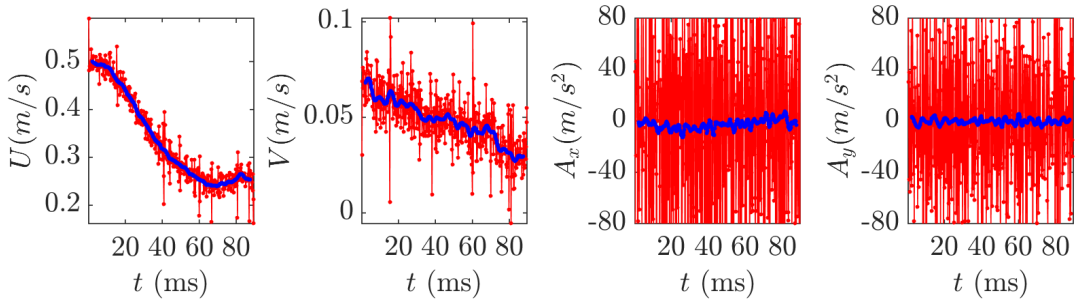

Figure 3.31: Plot of the raw velocity and acceleration data (in red) and the smoothed velocity and acceleration data (in blue) along a particle trajectory, plotted for both the streamwise (U and A_x) and spanwise (V and A_y) directions.

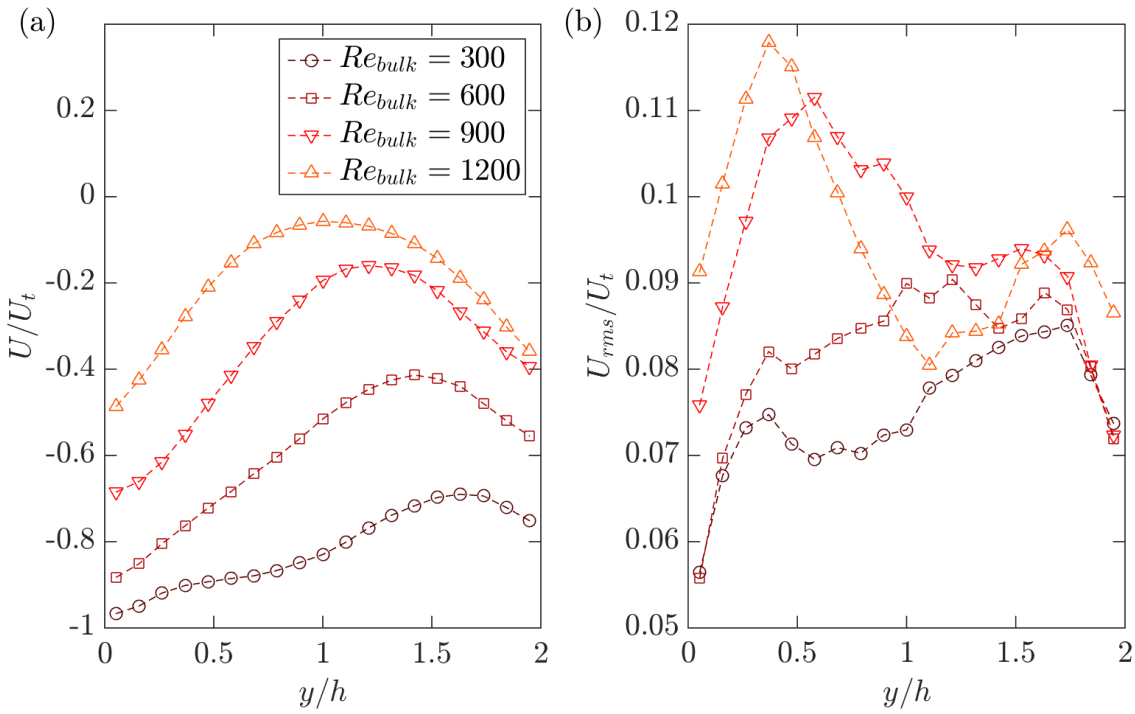

Figure 3.32: For 4 riser cases of increasing volume fractions (dark red to orange), (a) shows mean velocity profiles and (b) shows the r.m.s velocity profiles normalized by the single-particle terminal velocity, U_t.

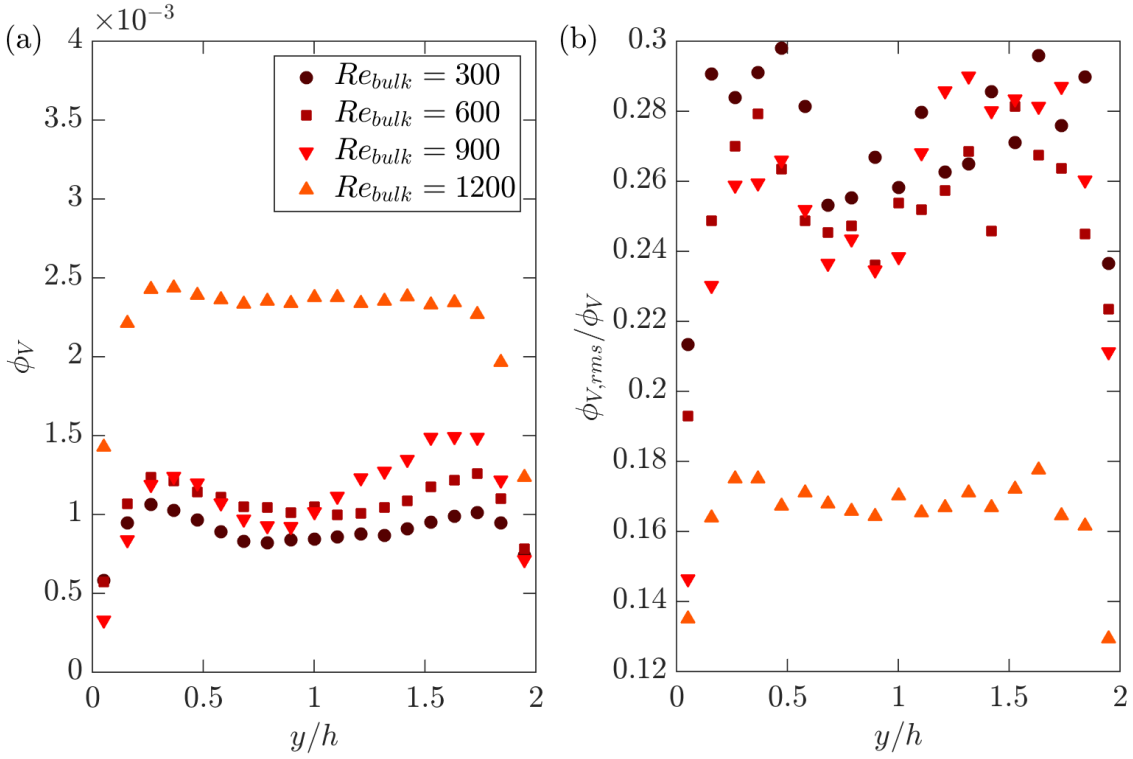

Figure 3.33: For 4 riser cases of increasing volume fractions (dark red to orange), (a) shows mean volume fractions and (b) shows the r.m.s fluctuations in the volume fraction normalized by the overall mean volume fraction for each case.

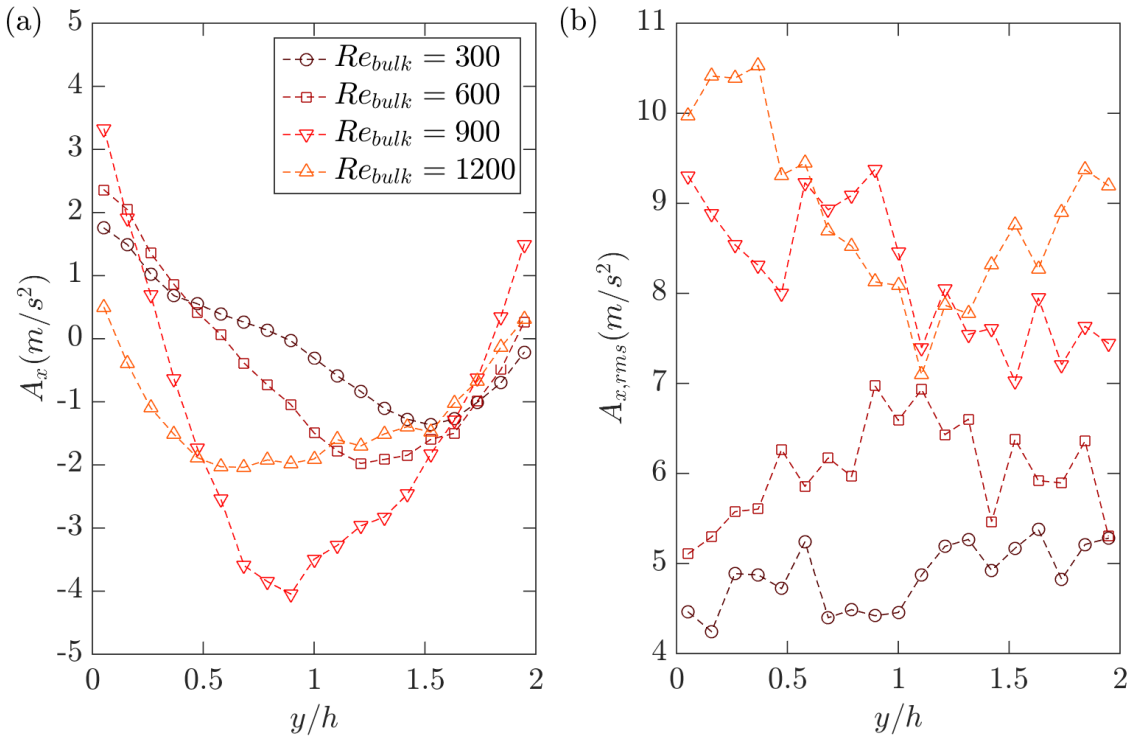

Figure 3.34: For 4 riser cases of increasing volume fractions (dark red to orange), (a) shows mean acceleration profiles and (b) shows the r.m.s acceleration profiles.

3.5 Zoomed-in measurements: Results

3.5.1 Particle velocity, concentration, and acceleration profiles

Figure 3.32a shows wall-to-wall profiles of mean particle velocities for different Re_{bulk}. Particles fall slower with stronger fluidizing air, in addition to making the profile more symmetric about the mean. This is due to higher mixing associated to the stronger fluidizing air, which is also reflected in the r.m.s. velocity profile in figure 3.32b where the variance of particle velocities increases with volume fraction. With the strongest fluidizing velocities, the r.m.s. profile shows peaks in particle velocity variance near the walls and a minimum in the channel center. For lower fluidization velocities, the r.m.s. profiles are more uniform throughout the channel. The overall mean of the zoomed-in velocity profile is comparable to the center of the zoomed-out profiles, with the zoomed-in velocities generally larger than the zoomed-out velocities, as well as showing similar trends as the zoomed-out velocities with regards to the fluidizing air.

Figure 3.33 shows the wall-to-wall profiles of the mean and normalized r.m.s. particle volume fraction. In the mean volume fractions, near-wall peaks are observed at wall-normal positions around 0.25 and 1.75 y/h across all cases, more prominent in the lower volume Re_{bulk} (and lower volume fraction). For all cases, the volume fractions drop off near the walls. The r.m.s. volume fractions fluctuate between 12 to 30 % of the mean, with higher percentage of fluctuation in the more dilute cases. Like the mean values, the r.m.s. concentration also appear lower near the walls. A reduction of concentration and fluctuation in the immediate vicinity of the wall is likely due to the excluded-volume effect: near-wall particles get in contact with the wall and/or interact with it through hydrodynamic processes, including lubrication forces, and they are repelled from it while losing kinetic energy (as suggested also by the near-wall drop of U_{rms} in figure 3.32b).

Figure 3.34a shows wall-to-wall acceleration profiles for the mean acceleration, showing that particles are accelerating near the wall (falling increasingly faster) and decelerating (falling increasingly slower) in the channel center. We observe no trends on acceleration magnitudes with fluidizing air strength, however the profile does appear to be more symmetric for the higher fluidizing airflow. The r.m.s. fluctuation profiles show high acceleration variances (figure 3.34b), which increases with higher fluidizing airflow up to values exceeding the gravitational acceleration. This shows that the particle tracks

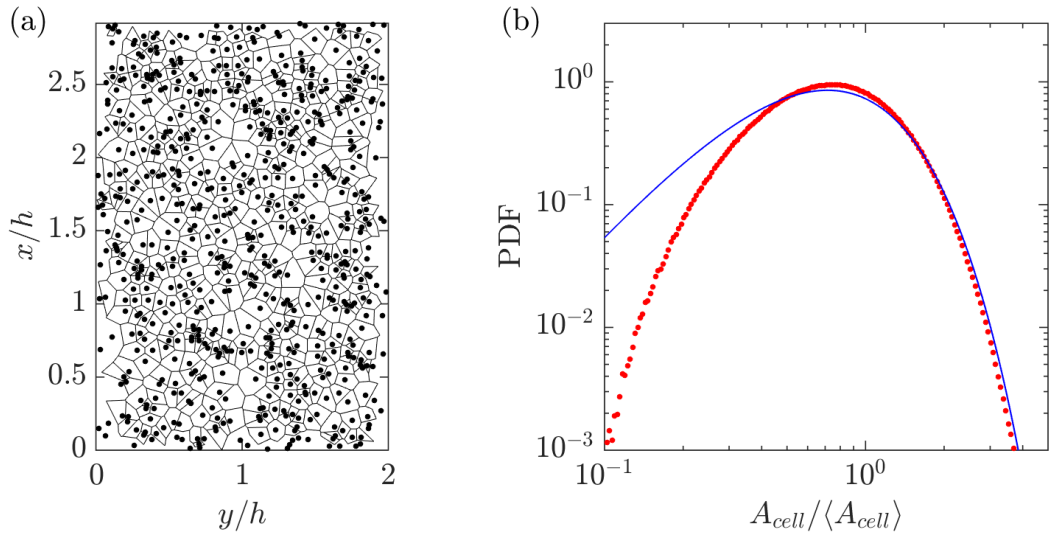

Figure 3.35: (a) Voronoi tessellation diagram in a sample realization for the case with $Re_{bulk} = 1200$ and $\phi_V = 2.6 \times 10^{-3}$. (b) Probability distribution function of the Voronoi cell areas A_{cell} (red circles), compared with a γ distribution (blue line).

are dominated by high acceleration r.m.s. events, which can include particle-wall collisions, interparticle collisions, and hydrodynamical interactions, which will be discussed in a later section.

3.5.2 Particle distribution: Voronoi analysis

In order to further study the instantaneous distribution of particle positions in the center-plane of the riser, we apply the Voronoi tessellation method (Monchaux *et al.*, 2010) designating a cell around every particle. Figure 3.35a shows a sample instantaneous realization of the Voronoi cells generated for every particle. Note that since the imaging area is bounded by walls, cells that border the walls are considered as biased to the wall shape and are discarded. Figure 3.35b shows, for the case $Re_{bulk} = 1200$, a PDF of the cell area distribution normalized by the mean, and compared with a random Poisson process which is well approximated by a γ distribution (Ferenc & Néda, 2007).

Here it is shown that the distribution of the cell sizes is 'sub-Poissonian', i.e. the variance of particle sizes is smaller compared to that of a randomly generated particle field. This implies that the topology of the particle field is in a 'crystallized' pattern

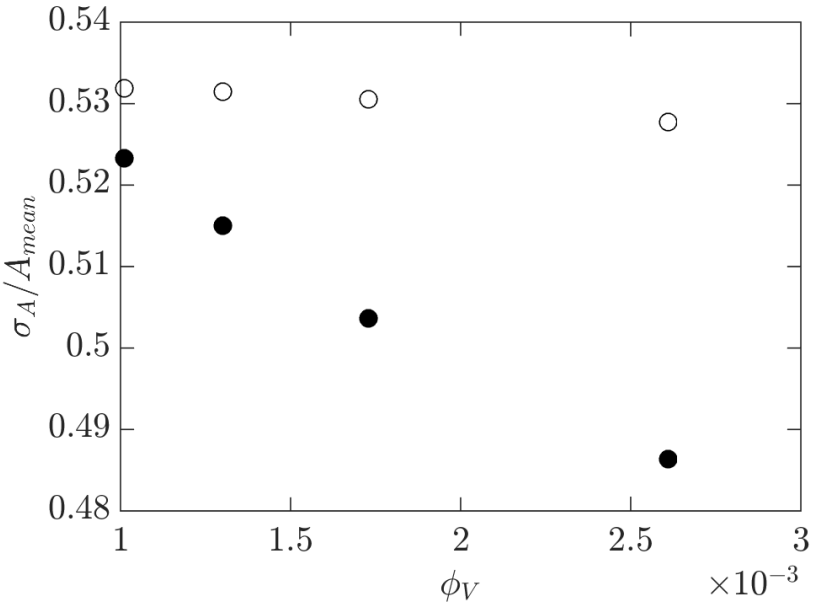

Figure 3.36: Plot of normalized standard distribution of cell sizes, σ_A/A_{mean} against volume fraction ϕ_V corresponding to $Re_{bulk} = 300, 600, 900, 1200$ of fluidizing air. Solid circles indicate experimental values and open circles indicate values from the simulated random 3D particle field.

with a relatively regular arrangement of cells, as observed in the distribution of near-wall inertial particles earlier in §2.3.2. In this experiment, this result can be due to the fact that particles are interacting with one another (either hydrodynamically or through collisions) in a way that leads to a relatively orderly arrangement. For this case, the normalized standard distribution of cell sizes, $\sigma_A/A_{mean} = 0.49$, which is lower than 0.53 for a purely random 2D distribution(Monchaux *et al.*, 2010) .

Similar results are observed for all other Re_{bulk} cases, with stronger 'sub-Poissionian' behaviour with increasing Re_{bulk} of fluidizing air. In Figure 3.36, we plot the value of σ_A/A_{mean} for each case, as well as the equivalent value for a random particle field, known to be 0.53 for a purely random 2D distribution (Monchaux *et al.*, 2010) . However, we have a nonstandard imaging setup with a depth-of-field of 2 mm. We simulate the imaging conditions by generating a 20000 randomly distributed particle fields in a volume equivalent to the imaged region, specifying the particles be non-overlapping spheres of the same mean diameter as the particles in our experiment. For each 3D field, we projected the particle positions on a 2D plane, reproducing the imaging process. We then generate the Voronoi tessellations on such 2D particle fields, and calculate the resulting σ_A/A_{mean}.

As shown in figure 3.36, even with the non-standard imaging, the values of σ_A/A_{mean} from the simulations are evidently higher compared to those from the experiments, showing that the particle distribution is indeed 'sub-Poissonian' for all riser cases. We remark that the zoomed-out imaging of the same cases did not indicate clustering, which is consistent with the particle spatial distribution being relatively orderly.

3.5.3 Eulerian two-point correlation of particle velocities

Even when the particles are not clustering, they could interact with one another hydrodynamically. We investigate this possibility by considering their two-point Eulerian velocity correlations, using the same procedure as outlined in §2.3.1. Once again, we are calculating the polar correlations, in which the separation vector spans the (r, θ) space. We only consider particles within $0.5 < y/h < 1.5$ to eliminate the influence of the wall, and we compute the correlations for the streamwise velocity fluctuations, u_p between particle pairs (m, n) using equation 2.3.

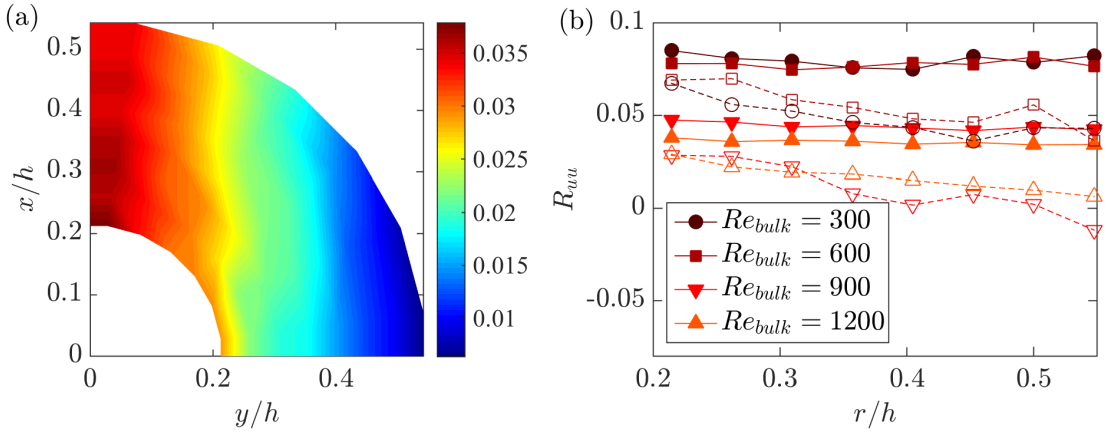

Figure 3.37: (a) Polar map of streamwise velocity two-point correlation along the centerplane for case $Re_{bulk} = 300$. (b) Two-point correlation of streamwise velocity fluctuations with separations in streamwise (filled symbols) and spanwise (empty symbols) directions along the centerplane for all riser cases.

Figure 3.37a displays the polar diagram of the streamwise velocity two-point correlation, R_{uu} at the centerplane for case $Re_{bulk} = 300$. As shown in the polar diagram, the streamwise velocity fluctuations are more correlated in the streamwise direction compared to the spanwise direction. This shows that particles are interacting with one another hydrodynamically in the streamwise direction more than in the spanwise direction. The overall magnitude is vanishingly low compared with figure 2.15 from the same R_{uu} plot in §2.3.1. This is expected, because the particles in the riser are much more inertial than those in the turbulent channel flow (212 µm compared to 47 µm in mean particle diameter), and therefore their fluctuating velocity have a much larger uncorrelated component.

Figure 3.37b displays the streamwise and spanwise R_{uu} against separation distances only, comparing between all particle riser cases $Re_{bulk} = 300$ through 1200. Here it is shown that with increasing strength of fluidizing air, the magnitude of the R_{uu} correlations in the streamwise direction is weakened, even though the directional trends are retained. This suggests that the spatial correlation of the particle velocity is not dictated by the airflow, but by particles interacting with each other's wakes, which are partly disrupted by the fluidizing airflow. We remark that, in this experiment, the particle Reynolds number, Re_p of the particles is of order $\mathcal{O}(10)$, and the particles are not

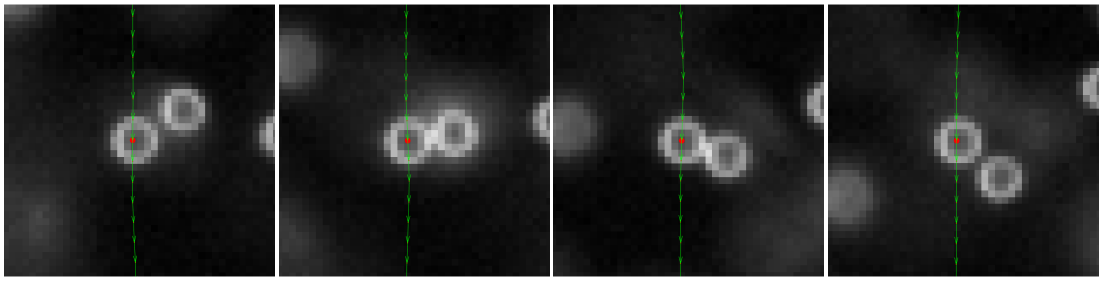

Figure 3.38: Sequence of snapshots showing hydrodynamic interaction between two particles.

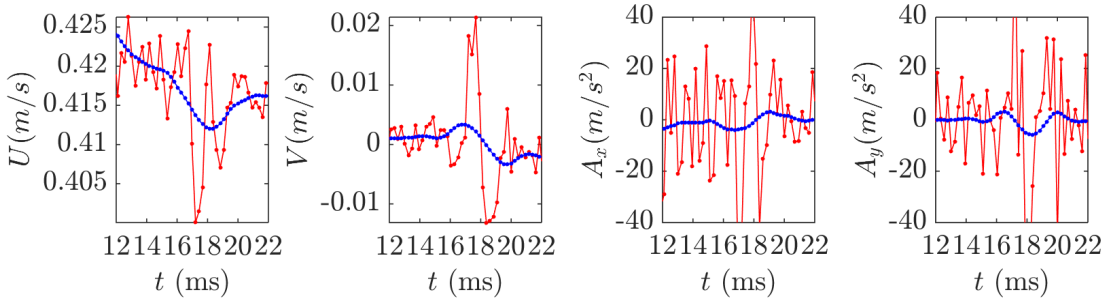

Figure 3.39: (from left) Plot of streamwise velocity U, spanwise velocity V, streamwise acceleration A_x, and spanwise acceleration A_y of the target particle throughout the sequence of snapshots in figure 3.38. Red lines are the raw data, whereas blue lines are the smoothed velocity and acceleration trajectories.

expected to generate very energetic wakes .

3.5.4 Collision detection and statistics

Particles can interact either hydrodynamically or via direct collisions. Hydrodynamic interactions are mediated by the fluid, causing relatively smooth changes in particle kinematics; while direct particle collisions is expected to lead to abrupt changes in particle trajectories. This is commonly observed as particle 'slipping' by each other, which is shown in the sequence of snapshots in figure 3.38. In figure 3.38, the target particle (with the red centroid) is overtaken by the particle to the right. This results in a slight perturbation in the target particle's velocity, most notably in the spanwise direction (figure 3.39) where the particle exhibits a transient spanwise velocity change, inducing an acceleration that does not exceed the gravitational acceleration $g = 9.81m/s^2$. After

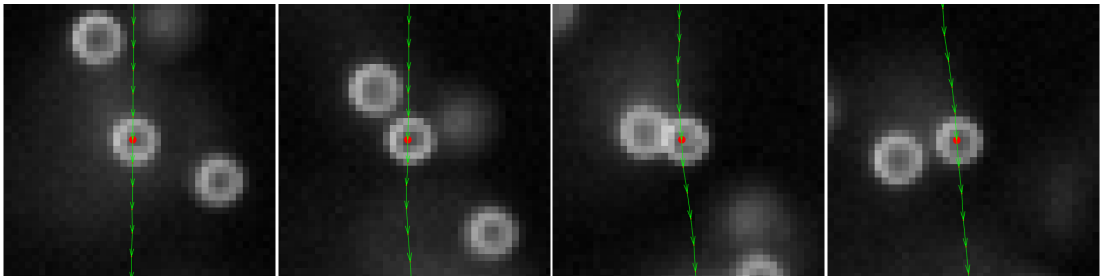

Figure 3.40: Sequence of snapshots showing a direct collision between two particles.

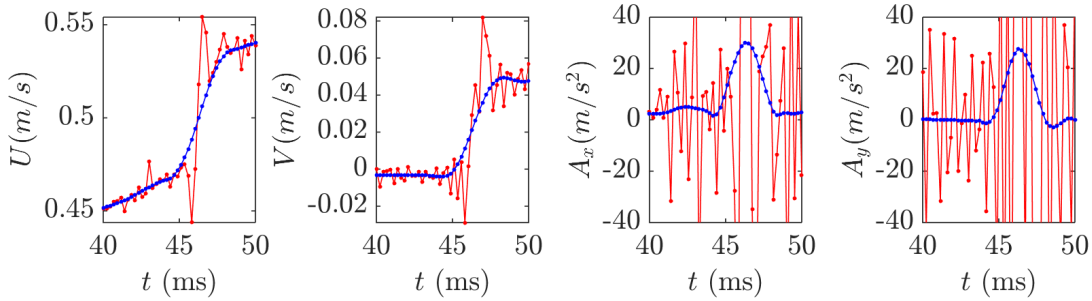

Figure 3.41: (from left) Plot of streamwise velocity U, spanwise velocity V, streamwise acceleration A_x, and spanwise acceleration A_y of the target particle throughout the sequence of snapshots in figure 3.40. Red lines are the raw data, whereas blue lines are the smoothed velocity and acceleration trajectories.

the interaction, the U and V velocities resume their previous trend, with little change to the trajectory of the particle.

Collisions between two particles, on the other hand, involve sudden changes in trajectory and velocities for both particles. One such example is shown below, with figure 3.40 being the sequence of snapshots of two colliding particles, and figure 3.41 being the velocity and acceleration plots of the target particle during the collision. Figure 3.41 shows typical signatures of collisions, including a step change in velocities during the collisions, and large acceleration events in the particle tracks usually exceeding $2g$ in magnitude. Importantly, these large acceleration events (blue lines) are distinguishable from the random noise caused by the uncertainty in particle centroid locations (red lines) after the smoothing procedure is applied as outlined in §3.4.1 .

Using this observation of extreme acceleration events, a simple collision detection method is implemented, detecting tracks with accelerations exceeding $2g$ when two

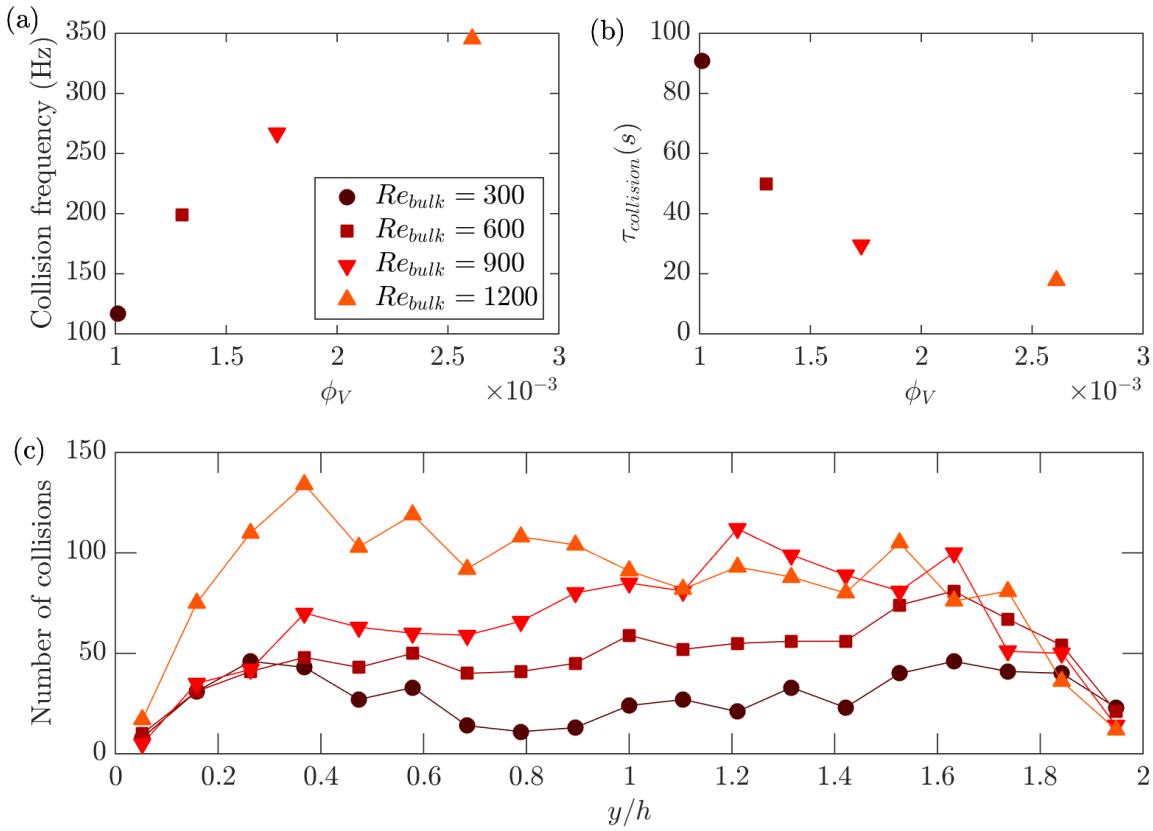

Figure 3.42: (a) Plot of collision frequency per particle in the volume, against the mean volume fraction. (b) Plot of the per-particle collision timescale, against the mean volume fraction. (c) Plot of number of collisions detected against wall-normal locations for cases $Re_{bulk} = 300$–1200.

particles get in contact with each other (i.e. their centroid-to-centroid distance is within $1.5d_p$). This is corroborated with visual inspection of $\sim$ 50 tracks, confirming that collisions are indeed observed in the tracks with accelerations exceeding the thresholds. Figure 3.42a shows that the frequency of collisions detected (i.e. the number of collisions divided by the recording time) increases with the case volume fraction, which in this case grows also with the strength of the fluidizing airflow. Normalizing by the particle number flow rate per second (computed from the volume fraction) reveals a per-particle collision timescale of $\mathcal{O}(10)$ seconds, with the timescale decreasing from 90 to 20 seconds with increasing volume fractions as shown in figure 3.42b. These collision timescales are much longer than the single particle relaxation timescale ($\tau_p = 0.155$s), signifying that particles have ample time to readjust to local fluid velocities after experiencing collisions. However, the observations are limited to collisions that occur in-plane, meaning that the collision timescale averaged for all particles throughout the riser volume is expected to be lower. Finally, figure 3.42c shows a profile of collision locations in the wall-normal direction, which shows that collisions are more likely to occur near-wall in the lower Re_{bulk} cases, but are more uniformly distributed in the higher Re_{bulk} cases.

Chapter 4

Conclusion and Discussion

In this thesis, we conducted experimental studies of the preferential concentration and clustering of particles in gas-solid duct flows over a broad range of parameters. In studying the preferential concentration phenomenon in turbulent wall-bounded flows, we have reported on a series of experiments conducted on a vertical turbulent channel flow at Re_τ =235 and 335, in which particle–laden air flows downward. Several aspects of the configuration are chosen to provide a canonical case: smooth walls, streamwise development, relatively large aspect ratio of the cross-section and small size-selected particles with $St_\eta = \mathcal{O}(10)$ and $St^+ = \mathcal{O}(100)$. Care is taken to keep the experimental parameters under strict control, including the smoothness of the walls and the particle mass loading. The latter is varied across what is usually considered the boundary between one-way and two-way coupling. Using laser imaging we have investigated in detail the particle spatial distribution and velocity, gaining new insight expected to be useful to reach a predictive understanding of particle–laden wall-bounded flows. The main findings are summarized as follows:

1. At volume fractions $\mathcal{O}(10^{-6})$, the particles show a distinct, although relatively mild, tendency to segregate near the wall, with the concentration displaying a second maximum at the channel centerline. The results are consistent with turbophoresis acting down the gradients of turbulence intensity, and in particular of V_{rms} as proposed by Young & Leeming (1997). At volume fractions $\mathcal{O}(10^{-5})$, the near-wall peak is much more pronounced and the centerline maximum is absent,

indicating more vigorous turbophoretic drift towards the wall. The increase of near-wall segregation with mass loading is opposite to that reported in previous two-way-coupled point-particle simulations.

2. The mean velocity profiles show particles travelling faster than the unladen fluid in the immediate vicinity of the wall, resulting in an effective slip velocity. Away from the wall, the more dilute case has particles following a profile similar to the unladen air velocity. In the denser case, the particles are measurably slower up to $y/h \sim 0.4(0.6)$ for the lower (higher) Stokes number. Both streamwise and wall-normal velocity fluctuations of the particles exceed those of the unladen fluid near the wall; in the denser case the effect is much more significant and extended to larger wall distances.

3. The wall-normal fluctuations do not vanish close to the wall, and lead to estimates of the deposition velocity in line with the expectations in the dilute case, but several times larger in the dense case. The particle Reynolds shear stress follows a similar behaviour to the normal stresses: it equals the unladen fluid stress in the channel core, but exceeds it when approaching the wall to a degree that depends on the loading. A quadrant analysis reveals that the prevalence of Q4 events (the equivalent of 'sweeps' for the fluid motion) is enhanced in the near-wall region compared to the unladen fluid, suggesting that fluid sweeps are key in the particle segregation process. The effects above are similarly displayed by all cases investigated here, but are more evident for the higher St.

4. In the channel core, the particles show a strong propensity to cluster, forming somewhat elongated objects preferentially aligned in the vertical streamwise direction. Clustering is more intense for the cases closer to the condition $St_\eta \sim 1$, although at higher St the clusters tend to be larger (Petersen *et al.* 2019). Groups of particles above a certain size range ('coherent clusters'; Baker *et al.* 2017) reach concentrations several times higher than the global mean, and tend to travel faster than the non-clustered particles. This suggests that, although the flow in the channel core is a poor approximation of homogeneous isotropic turbulence, the classic phenomena of preferential concentration (Squires & Eaton 1991) and preferential sweeping (Wang & Maxey 1993) are at play.

5. In the near-wall region the particles are observed to form elongated streaks, several channel heights in length and spaced by $\mathcal{O}(100)$ wall units. Those streaks tend to move slower than the generic particles, supporting the view that they are coupled to fluid low-speed streaks typical of wall turbulence. The particle velocity contains a significant component of random uncorrelated motion. In agreement with the mesoscopic Eulerian formalism introduced by Fevrier *et al.* (2005), this Brownian-like motion is more prominent for higher St and in the near-wall region, where the particle response time is much longer than the turbulent time scales.

6. Taken together, these results are consistent with a scenario in which the increase in volume fraction from $\mathcal{O}(10^{-6})$ to $\mathcal{O}(10^{-5})$ triggers two-way and (locally) four-way coupling effects. In particular, the particle back-reaction may alter the turbulence structure in ways that enhance the turbophoretic drift towards the wall (e.g. by enhancing the peak of turbulence intensity and/or displacing it away from the wall). In turn, the higher near-wall concentration may promote interparticle and wall–particle collisions. These would damp the particle kinetic energy, causing them to travel more slowly but enhancing their velocity fluctuations, as observed. Moreover, the inelastic collisions may prevent the particles from escaping the near-wall region (Hrenya & Sinclair 1997).

In studying clustering in dense gas-solid flows, we have reported on a series of experiments conducted on a vertical square channel from $Re_{bulk} = 300$ to 1200, with particles falling against rising air. The particles are characterized by a Galileo number $Ga = 29.4$. The configuration of the experiment allows control over the solids volume fraction from $\phi_V = 1 \times 10^{-3}$ to 8×10^{-3}, and the square cross-section allows 3-dimensional clusters to form. Using backlighting imaging, we have investigated the particle concentration and velocities, and performed statistical analysis to uncover relationships between the velocities and concentration of particles and their evolution in time. The main findings from the experiment are as follows:

1. Results show that, in the present range of parameters investigated, cases with volume fraction above $\phi_V = 5 \times 10^{-3}$ exhibits clustering, regardless of fluidization velocities. The critical volume fraction found is an empirically observed quantity

and currently not deductible from particle properties or flow parameters. Formation of these clusters influence the mean and the r.m.s. statistics of the riser, and also strongly modulates the two-point correlation statistics of the riser.

2. Space-time autocorrelation analysis reveals the convection of structures in the velocity and concentration fluctuation fields, at velocities larger than the mean largely independent of the wall-normal location and also the strength of the fluidizing air. It was also shown that the convection velocity in the velocity fluctuation field is greater than that of the concentration fluctuation field. We also show that the fluctuations of velocities and concentrations in most riser cases are also well-described by the classic gradient diffusion hypothesis, with the clustered cases showing enhanced mixing compared to the non-clustered cases. This also shows the continuum nature of the particle field in this riser, and lends credence to simulations using kinetic models that models the dispersed phase as a quasi-continuum.

3. Across all clustered cases, clusters are found mostly near the wall, and their areas mostly range between $0.1D^2$ and $1D^2$ regardless of the fluidizing air. The cluster areas and concentrations grow with increasing distance away from the walls up to $0.5y/h$, suggesting that clusters grow by incorporating more particles.

4. The cluster slip velocities are shown to follow a model prediction by Noymer & Glicksman (2000), which dictates that the cluster descent velocities are dependent only on the intrinsic properties of the particle and fluid. However, rather than predicting the absolute descend velocity, in the present system the model can rather be applied to the slip velocity relative to the upward bulk flow velocity.

5. Particles in the center plane of the riser are shown to have a sub-Poissonian spatial distribution and are not clustered, even though their streamwise velocity fluctuations are correlated in the streamwise direction.

6. Preliminary results on inter-particle interactions indicate that direct collisions produce accelerations in excess of $2g$, which become more frequent for higher concentration and bulk flow velocities.

7. Taken together, these results present a scenario in which reaching a critical volume fraction triggers the clustering of particles in a particle riser regardless of the fluidization velocity of the rising air, which is in line with the condition for kinematic instability leading to clustering (Fullmer & Hrenya 2017).

4.1 Discussions and recommendations

In the study of preferential concentration of particles in turbulent wall-bounded flows and its effect on the fluid via two-way coupling, previous experiments focused on the present regime have been scarce (refer to table 2.1 for a short list of relevant experiments). The lack is unfortunate, especially given the need to validate point-particle models and the exorbitant cost of particle-resolved simulations. Contrasting our observations with previous numerical studies suggests that, while point-particle simulations capture many key features of the particle transport (Soldati & Marchioli 2009), the underlying hypotheses may be missing or misestimating some important aspects, especially concerning the two-way and four-way coupling. This is exemplified by the increased near-wall concentration measured here for increasing mass loading, which is opposite to the trend found in past simulations. The limitations of point-particle methods in capturing the two-way coupling are well known (Eaton 2009; Balachandar & Eaton 2010); however, recent approach such as volume-filtering methods (Capecelatro & Desjardins 2015) are showing promising improvements. The moderate Reynolds number in our study may also allow for a comparison with future particle-resolved simulations, which are becoming feasible even for relatively small particles (Schneiders *et al.* 2017).

Future experimental studies should also fill the knowledge gap of the fluid-phase statistics in the flow, for example using phase separation techniques (Kiger & Pan 2000; Khalitov & Longmire 2002; Capone *et al.* 2015; Petersen *et al.* 2019) to accurately measure fluid statistics in the near-wall region. This, however, is expected to be a challenging task: small inertial particles accumulating near the wall pose a major problem to imaging surrounding tracers. This can be partly alleviated by augmenting the spatial resolution, which is becoming possible thanks to the steady increase of the sensor size of available cameras (Discetti & Coletti, 2018).

Studies of particle clustering in dense gas-solid risers with fine control over the

particle volume fraction in the system are scarce. Most studies employ a fluidized bed setup (Harris *et al.* 2002, Cahyadi *et al.* 2017), with few notable exceptions such as Weit *et al.* (2018, 2019) whose experiments are described in §1.3. The opaqueness of the dense gas-solid flow renders traditional laser-based imaging inapplicable due to the optical thickness of the mixture, and one must resort to optically depth-averaged methods like shadow imaging (Xu & Zhu 2011; Yang & Zhu 2014, 2015) to capture the dynamics of the particle field, especially in the large scales. Small-scale imaging, on the other hand have been achieved with the use of a borescope (Tartan & Gidaspow 2004; Shaffer *et al.* 2013) and can yield valuable information on individual particle velocities and densities. More recently, 3D imaging methods such as digital inline holography (Li *et al.* 2021*b*) recently shows promising results in resolving individual 3D particle locations in a particle riser, albeit still limited to a small field of view. This approach, like the borescope method, is thus unable to capture mesoscale clusters. For the large fields of view, high-speed X-ray imaging can represent a viable alternative to achieve cluster-scale resolution, having been shown to work for other dense multiphase flows such as gas-liquid atomizers and fluidized beds reactors (Aliseda & Heindel 2021).

The present experiments have shown that cluster formation occurs beyond a critical volume fraction, while strength of the fluidizing airflow has little influence in the considered range. However, the microscopic process of cluster formation is still unclear. A possible microscopic scenario involves the interaction of two particles via collisions during a timescale where the effect of the encounter dissipates. After this recovery time, both particles are only influenced by the interstitial fluid again. However, if the particle encounters another particle before the recovery time lapses, they meet with less kinetic energy than the previous encounter. Frequent collision would result in a continuous dissipation of energy at the macroscopic level, leading to clusters. In this scenario, the volume fraction dictates the rate of encounters, and when a critical volume fraction is met, the likelihood of collisions is higher. Attempts with the zoomed-in dataset shows that the rate of collisions increases with volume fractions. However, the observations are limited to collisions that occur in-plane, and also are limited to cases where the solid volume fraction does not lead to clustering. This hypothesis is unfortunately one that cannot be investigated with currently known experimental means, and thus must

rely on numerical studies using either particle-resolved methods or four-way coupled Lagrangian particle methods. Special care must be taken in simulating collisions by using a realistic definition of the restitution coefficient, which is shown to vary significantly depending on the collision velocity (Joseph *et al.* 2001;Gondret *et al.* 2002). Given the possibly large variance of the collision velocity and the role of inelastic collisions to enhance particle clustering (Fullmer & Hrenya, 2017), the common assumption of a constant restitution coefficient might be inadequate.

References

Agrawal, Kapil, Loezos, Peter N, Syamlal, Madhava & Sundaresan, Sankaran 2001 The role of meso-scale structures in rapid gas-solid flows. *Journal of Fluid Mechanics* **445**, 151.

Aliseda, Alberto, Cartellier, Alain, Hainaux, F & Lasheras, Juan C 2002 Effect of preferential concentration on the settling velocity of heavy particles in homogeneous isotropic turbulence. *Journal of Fluid Mechanics* **468**, 77–105.

Aliseda, Alberto & Heindel, Theodore J 2021 X-ray flow visualization in multiphase flows. *Annual Review of Fluid Mechanics* **53**, 543–567.

Baek, SJ & Lee, SJ 1996 A new two-frame particle tracking algorithm using match probability. *Experiments in Fluids* **22** (1), 23–32.

Baker, Lucia, Frankel, Ari, Mani, Ali & Coletti, Filippo 2017 Coherent clusters of inertial particles in homogeneous turbulence. *Journal of Fluid Mechanics* **833**, 364–398.

Balachandar, S. & Eaton, J. K. 2010 Turbulent dispersed multiphase flow. *Annu. Rev. Fluid Mech.* **42**, 111–133.

Balachandar, S, Liu, Kai & Lakhote, Mandar 2019 Self-induced velocity correction for improved drag estimation in euler–lagrange point-particle simulations. *Journal of Computational Physics* **376**, 160–185.

Beetham, S & Capecelatro, J 2019 Biomass pyrolysis in fully-developed turbulent riser flow. *Renewable energy* **140**, 751–760.

Benson, Michael, Tanaka, Tomohiko & Eaton, John K 2005 Effects of wall roughness on particle velocities in a turbulent channel flow. *Journal of fluids engineering* **127** (2), 250–256.

Bernard, Peter S & Wallace, James M 2002 *Turbulent flow: analysis, measurement, and prediction*. John Wiley & Sons.

Bernardini, Matteo 2014 Reynolds number scaling of inertial particle statistics in turbulent channel flows. *Journal of Fluid Mechanics* **758**.

Bewley, Gregory P, Saw, Ewe-Wei & Bodenschatz, Eberhard 2013 Observation of the sling effect. *New Journal of Physics* **15** (8), 083051.

Bosse, Thorsten, Kleiser, Leonhard & Meiburg, Eckart 2006 Small particles in homogeneous turbulence: Settling velocity enhancement by two-way coupling. *Physics of Fluids* **18** (2), 027102.

Bragg, Andrew D & Collins, Lance R 2014 New insights from comparing statistical theories for inertial particles in turbulence: I. spatial distribution of particles. *New Journal of Physics* **16** (5), 055013.

Breault, Ronald W, Rowan, Steven L, Weber, Justin M & Yang, Jingsi 2020 Effects of riser diameter on solids holdup and particle velocity profiles in circulating fluidized bed riser systems. *Journal of Energy Resources Technology* **142** (7).

Cahyadi, Andy, Anantharaman, Aditya, Yang, Shiliang, Karri, SB Reddy, Findlay, John G, Cocco, Ray A & Chew, Jia Wei 2017 Review of cluster characteristics in circulating fluidized bed (cfb) risers. *Chemical Engineering Science* **158**, 70–95.

Capecelatro, Jesse & Desjardins, Olivier 2013 An euler–lagrange strategy for simulating particle-laden flows. *Journal of Computational Physics* **238**, 1–31.

Capecelatro, Jesse & Desjardins, Olivier 2015 Mass loading effects on turbulence modulation by particle clustering in dilute and moderately dilute channel flows. *Journal of Fluids Engineering* **137** (11), 111102.

Capecelatro, Jesse, Desjardins, Olivier & Fox, Rodney O 2015 On fluid-particle dynamics in fully developed cluster-induced turbulence. *Journal of Fluid Mechanics* **780**, 578.

Capecelatro, Jesse, Desjardins, Olivier & Fox, Rodney O 2016 Strongly coupled fluid-particle flows in vertical channels. i. reynolds-averaged two-phase turbulence statistics. *Physics of Fluids* **28** (3), 033306.

Capecelatro, Jesse, Desjardins, Olivier & Fox, Rodney O 2018 On the transition between turbulence regimes in particle-laden channel flows. *Journal of Fluid Mechanics* **845**, 499–519.

Capecelatro, Jesse, Pepiot, Perrine & Desjardins, Olivier 2014 Numerical characterization and modeling of particle clustering in wall-bounded vertical risers. *Chemical Engineering Journal* **245**, 295–310.

Capone, Alessandro, Romano, Giovanni Paolo & Soldati, Alfredo 2015 Experimental investigation on interactions among fluid and rod-like particles in a turbulent pipe jet by means of particle image velocimetry. *Experiments in Fluids* **56** (1), 1.

Caporaloni, M, Tampieri, F, Trombetti, F & Vittori, O 1975 Transfer of particles in nonisotropic air turbulence. *Journal of the atmospheric sciences* **32** (3), 565–568.

Caraman, N, Borée, J & Simonin, Olivier 2003 Effect of collisions on the dispersed phase fluctuation in a dilute tube flow: Experimental and theoretical analysis. *Physics of Fluids* **15** (12), 3602–3612.

Carter, Douglas W & Coletti, Filippo 2018 Small-scale structure and energy transfer in homogeneous turbulence. *Journal of Fluid Mechanics* **854**, 505–543.

Clift, Roland, Grace, John R & Weber, Martin E 2005 *Bubbles, drops, and particles*. Courier Corporation.

Cocco, Ray, Karri, SB Reddy, Knowlton, Ted & others 2014 Introduction to fluidization. *Chem. Eng. Prog* **110** (11), 21–29.

Davidson, Peter Alan 2015 *Turbulence: an introduction for scientists and engineers*. Oxford university press.

Dennis, David JC & Nickels, Timothy B 2008 On the limitations of taylor's hypothesis in constructing long structures in a turbulent boundary layer. *Journal of Fluid Mechanics* **614**, 197.

Discetti, Stefano & Coletti, Filippo 2018 Volumetric velocimetry for fluid flows. *Measurement Science and Technology* **29** (4), 042001.

Dritselis, Chris D & Vlachos, Nicholas S 2011 Numerical investigation of momentum exchange between particles and coherent structures in low re turbulent channel flow. *Physics of Fluids* **23** (2), 025103.

Eaton, John K 2009 Two-way coupled turbulence simulations of gas-particle flows using point-particle tracking. *International Journal of Multiphase Flow* **35** (9), 792–800.

Eaton, John K & Fessler, JR 1994 Preferential concentration of particles by turbulence. *International Journal of Multiphase Flow* **20**, 169–209.

Elghobashi, S. 1994 On predicting particle-laden turbulent flows. *Appl. Sci. Res.* **52** (4), 309–329.

Ern, Patricia, Risso, Frédéric, Fabre, David & Magnaudet, Jacques 2012 Wake-induced oscillatory paths of bodies freely rising or falling in fluids. *Annual Review of Fluid Mechanics* **44**, 97–121.

Ferenc, Járai-Szabó & Néda, Zoltán 2007 On the size distribution of poisson voronoi cells. *Physica A: Statistical Mechanics and its Applications* **385** (2), 518–526.

Fessler, John R, Kulick, Jonathan D & Eaton, John K 1994 Preferential concentration of heavy particles in a turbulent channel flow. *Physics of Fluids* **6** (11), 3742–3749.

Fevrier, Pierre, Simonin, Olivier & Squires, Kyle D 2005 Partitioning of particle velocities in gas–solid turbulent flows into a continuous field and a spatially

uncorrelated random distribution: theoretical formalism and numerical study. *Journal of Fluid Mechanics* **533**, 1–46.

Fouxon, Itzhak, Schmidt, Lukas, Ditlevsen, Peter, van Reeuwijk, Maarten & Holzner, Markus 2018 Inhomogeneous growth of fluctuations of concentration of inertial particles in channel turbulence. *Physical Review Fluids* **3** (6), 064301.

Frankel, Ari, Pouransari, Hadi, Coletti, Filippo & Mani, Ali 2016 Settling of heated particles in homogeneous turbulence. *Journal of Fluid Mechanics* **792**, 869–893.

Fullmer, William D & Hrenya, Christine M 2017 The clustering instability in rapid granular and gas-solid flows. *Annual Review of Fluid Mechanics* **49**, 485–510.

Garcia-Villalba, Manuel, Kidanemariam, Aman G & Uhlmann, Markus 2012 Dns of vertical plane channel flow with finite-size particles: Voronoi analysis, acceleration statistics and particle-conditioned averaging. *International Journal of Multiphase Flow* **46**, 54–74.

Gerashchenko, S, Sharp, NS, Neuscamman, S & Warhaft, Z 2008 Lagrangian measurements of inertial particle accelerations in a turbulent boundary layer. *Journal of fluid mechanics* **617**, 255.

Goldhirsch, ISAAC & Zanetti, G 1993 Clustering instability in dissipative gases. *Physical review letters* **70** (11), 1619.

Gondret, P, Lance, M & Petit, L 2002 Bouncing motion of spherical particles in fluids. *Physics of fluids* **14** (2), 643–652.

Gualtieri, Picano, Picano, F & Casciola, CM 2009 Anisotropic clustering of inertial particles in homogeneous shear flow. *Journal of Fluid Mechanics* **629**, 25–39.

Gualtieri, Paolo, Picano, F, Sardina, Gaetano & Casciola, Carlo Massimo 2015 Exact regularized point particle method for multiphase flows in the two-way coupling regime. *Journal of Fluid Mechanics* **773**, 520–561.

Guha, Abhijit 2008 Transport and deposition of particles in turbulent and laminar flow. *Annu. Rev. Fluid Mech.* **40**, 311–341.

Guo, Lei & Capecelatro, Jesse 2019 The role of clusters on heat transfer in sedimenting gas-solid flows. *International Journal of Heat and Mass Transfer* **132**, 1217–1230.

Gustavsson, K & Mehlig, B 2016 Statistical models for spatial patterns of heavy particles in turbulence. *Advances in Physics* **65** (1), 1–57.

Hadinoto, K, Jones, EN, Yurteri, C & Curtis, JS 2005 Reynolds number dependence of gas-phase turbulence in gas–particle flows. *International journal of multiphase flow* **31** (4), 416–434.

Hardalupas, Y, Taylor, AMKP & Whitelaw, James Hunter 1989 Velocity and particle-flux characteristics of turbulent particle-laden jets. *Proc. R. Soc. Lond. A* **426** (1870), 31–78.

Harris, AT, Davidson, JF & Thorpe, RB 2002 The prediction of particle cluster properties in the near wall region of a vertical riser (200157). *Powder Technology* **127** (2), 128–143.

Hassan, YA, Blanchat, TK, Seeley Jr, CH & Canaan, RE 1992 Simultaneous velocity measurements of both components of a two-phase flow using particle image velocimetry. *International Journal of Multiphase Flow* **18** (3), 371–395.

Holtzer, Gretchen L & Collins, Lance R 2002 Relationship between the intrinsic radial distribution function for an isotropic field of particles and lower-dimensional measurements. *Journal of Fluid Mechanics* **459**, 93–102.

Horwitz, JAK & Mani, Ali 2016 Accurate calculation of stokes drag for point–particle tracking in two-way coupled flows. *Journal of Computational Physics* **318**, 85–109.

Hrenya, Christine M & Sinclair, Jennifer L 1997 Effects of particle-phase turbulence in gas-solid flows. *AIChE Journal* **43** (4), 853–869.

Huisman, Sander G, Barois, Thomas, Bourgoin, Mickaël, Chouippe, Agathe, Doychev, Todor, Huck, Peter, Morales, Carla E Bello, Uhlmann, Markus & Volk, Romain 2016 Columnar structure formation of a

dilute suspension of settling spherical particles in a quiescent fluid. *Physical Review Fluids* **1** (7), 074204.

Ireland, Peter J & Desjardins, Olivier 2017 Improving particle drag predictions in euler–lagrange simulations with two-way coupling. *Journal of Computational Physics* **338**, 405–430.

de Jong, J, Salazar, JPLC, Woodward, SH, Collins, LR & Meng, H 2010 Measurement of inertial particle clustering and relative velocity statistics in isotropic turbulence using holographic imaging. *International Journal of Multiphase Flow* **36** (4), 324–332.

Joseph, GG, Zenit, R, Hunt, ML & Rosenwinkel, AM 2001 Particle–wall collisions in a viscous fluid. *Journal of Fluid Mechanics* **433**, 329–346.

Kaftori, D, Hetsroni, G & Banerjee, S 1995*a* Particle behavior in the turbulent boundary layer. i. motion, deposition, and entrainment. *Physics of Fluids* **7** (5), 1095–1106.

Kaftori, D, Hetsroni, G & Banerjee, S 1995*b* Particle behavior in the turbulent boundary layer. ii. velocity and distribution profiles. *Physics of Fluids* **7** (5), 1107–1121.

Kajishima, Takeo & Takiguchi, Saotshi 2002 Interaction between particle clusters and particle-induced turbulence. *International Journal of Heat and Fluid Flow* **23** (5), 639–646.

Khalitov, DA & Longmire, EK 2002 Simultaneous two-phase piv by two-parameter phase discrimination. *Experiments in fluids* **32** (2), 252–268.

Khalitov, Daniel A & Longmire, Ellen K 2003 Effect of particle size on velocity correlations in turbulent channel flow. In *ASME/JSME 2003 4th Joint Fluids Summer Engineering Conference*, pp. 445–453. American Society of Mechanical Engineers.

Kiger, KT & Pan, C 2000 Piv technique for the simultaneous measurement of dilute two-phase flows. *Journal of fluids engineering* **122** (4), 811–818.

Kiger, KT & Pan, C 2002 Suspension and turbulence modification effects of solid particulates on a horizontal turbulent channel flow. *J. Turbulence* **3** (19), 1–17.

Kim, John, Moin, Parviz & Moser, Robert 1987 Turbulence statistics in fully developed channel flow at low reynolds number. *Journal of fluid mechanics* **177**, 133–166.

Kleinstreuer, C & Zhang, Z 2010 Airflow and particle transport in the human respiratory system. *Annual review of fluid mechanics* **42**, 301–334.

Knowles, Philip L & Kiger, Ken T 2012 Quantification of dispersed phase concentration using light sheet imaging methods. *Experiments in fluids* **52** (3), 697–708.

Kuerten, Johannes GM & Vreman, AW 2015 Effect of droplet interaction on droplet-laden turbulent channel flow. *Physics of fluids* **27** (5), 053304.

Kulick, Jonathan D, Fessler, John R & Eaton, John K 1994 Particle response and turbulence modification in fully developed channel flow. *Journal of Fluid Mechanics* **277**, 109–134.

Kussin, J & Sommerfeld, M 2002 Experimental studies on particle behaviour and turbulence modification in horizontal channel flow with different wall roughness. *Experiments in Fluids* **33** (1), 143–159.

Li, Cheng, Lim, Kaeul, Berk, Tim, Abraham, Aliza, Heisel, Michael, Guala, Michele, Coletti, Filippo & Hong, Jiarong 2021*a* Settling and clustering of snow particles in atmospheric turbulence. *Journal of Fluid Mechanics* **912**, A49.

Li, Cheng, Panday, Rupendranath, Gao, Xi, Hong, Jiarong & Rogers, William A 2021*b* Measuring particle dynamics in a fluidized bed using digital in-line holography. *Chemical Engineering Journal* **405**, 126824.

Li, Dong, Luo, Kun & Fan, Jianren 2016 Modulation of turbulence by dispersed solid particles in a spatially developing flat-plate boundary layer. *Journal of Fluid Mechanics* **802**, 359–394.

Li, Jing, Wang, Hanfeng, Liu, Zhaohui, Chen, Sheng & Zheng, Chuguang 2012 An experimental study on turbulence modification in the near-wall boundary layer of a dilute gas-particle channel flow. *Experiments in fluids* **53** (5), 1385–1403.

Li, Yiming, McLaughlin, John B, Kontomaris, K & Portela, L 2001 Numerical simulation of particle-laden turbulent channel flow. *Physics of Fluids* **13** (10), 2957–2967.

Lin, Zhao-wu, Shao, Xue-ming, Yu, Zhao-sheng & Wang, Lian-ping 2017 Effects of finite-size heavy particles on the turbulent flows in a square duct. *Journal of Hydrodynamics* **29** (2), 272–282.

Lints, Michael C & Glicksman, Leon R 1993 The structure of particle clusters near the wall of a circulating fluidized bed. In *AIChE symposium series*, pp. 35–35. American Institute of Chemical Engineers.

Liu, Benjamin YH & Agarwal, Jugal K 1974 Experimental observation of aerosol deposition in turbulent flow. *Journal of Aerosol Science* **5** (2), 145–155.

Marchioli, Cristian & Soldati, Alfredo 2002 Mechanisms for particle transfer and segregation in a turbulent boundary layer. *Journal of fluid Mechanics* **468**, 283–315.

Marchioli, Ch, Soldati, A, Kuerten, JGM, Arcen, B, Taniere, A, Goldensoph, G, Squires, KD, Cargnelutti, MF & Portela, LM 2008 Statistics of particle dispersion in direct numerical simulations of wall-bounded turbulence: results of an international collaborative benchmark test. *International Journal of Multiphase Flow* **34** (9), 879–893.

Masi, Enrica, Simonin, Olivier, Riber, Eleonore, Sierra, P & Gicquel, Laurent YM 2014 Development of an algebraic-closure-based moment method for unsteady eulerian simulations of particle-laden turbulent flows in very dilute regime. *International Journal of Multiphase Flow* **58**, 257–278.

Maxey, MR 1987 The gravitational settling of aerosol particles in homogeneous turbulence and random flow fields. *Journal of Fluid Mechanics* **174**, 441–465.

McLaughlin, John B 1989 Aerosol particle deposition in numerically simulated channel flow. *Physics of Fluids A: Fluid Dynamics* **1** (7), 1211–1224.

McMillan, Jennifer, Shaffer, Frank, Gopalan, Balaji, Chew, Jia Wei, Hrenya, Christine, Hays, Roy, Karri, SB Reddy & Cocco, Ray 2013 Particle cluster dynamics during fluidization. *Chemical Engineering Science* **100**, 39–51.

Meneguz, Elena & Reeks, Michael W 2011 Statistical properties of particle segregation in homogeneous isotropic turbulence. *Journal of Fluid Mechanics* **686**, 338–351.

Moisy, Frédéric & Jiménez, Javier 2004 Geometry and clustering of intense structures in isotropic turbulence. *Journal of fluid mechanics* **513**, 111.

Monchaux, Romain, Bourgoin, Mickaël & Cartellier, Alain 2010 Preferential concentration of heavy particles: a voronoï analysis. *Physics of Fluids* **22** (10), 103304.

Monchaux, Romain, Bourgoin, Mickael & Cartellier, Alain 2012 Analyzing preferential concentration and clustering of inertial particles in turbulence. *International Journal of Multiphase Flow* **40**, 1–18.

Mordant, Nicolas, Crawford, Alice M & Bodenschatz, Eberhard 2004 Experimental lagrangian acceleration probability density function measurement. *Physica D: Nonlinear Phenomena* **193** (1-4), 245–251.

Moser, Robert D, Kim, John & Mansour, Nagi N 1999 Direct numerical simulation of turbulent channel flow up to re τ= 590. *Physics of fluids* **11** (4), 943–945.

Nasr, Hojjat, Ahmadi, Goodarz & McLaughlin, John B 2009 A dns study of effects of particle–particle collisions and two-way coupling on particle deposition and phasic fluctuations. *Journal of Fluid Mechanics* **640**, 507–536.

Nemes, Andras, Dasari, Teja, Hong, Jiarong, Guala, Michele & Coletti, Filippo 2017 Snowflakes in the atmospheric surface layer: observation of particle-turbulence dynamics. *Journal of Fluid Mechanics* **814**, 592.

Nicolai, Claudia, Jacob, B & Piva, Renzo 2013 On the spatial distribution of small heavy particles in homogeneous shear turbulence. *Physics of Fluids* **25** (8), 083301.

Nilsen, Christopher, Andersson, Helge I & Zhao, Lihao 2013 A voronoï analysis of preferential concentration in a vertical channel flow. *Physics of Fluids* **25** (11), 115108.

Niño, Y & Garcia, MH 1996 Experiments on particle—turbulence interactions in the near–wall region of an open channel flow: implications for sediment transport. *Journal of Fluid Mechanics* **326**, 285–319.

Noymer, Peter D & Glicksman, Leon R 2000 Descent velocities of particle clusters at the wall of a circulating fluidized bed. *Chemical engineering science* **55** (22), 5283–5289.

Ohmi, Kazuo & Li, Hang-Yu 2000 Particle-tracking velocimetry with new algorithms. *Measurement Science and Technology* **11** (6), 603.

Oliveira, JL Goes, van der Geld, CWM & Kuerten, Johannes GM 2017 Concentration and velocity statistics of inertial particles in upward and downward pipe flow. *Journal of fluid mechanics* **822**, 640–663.

Ouellette, Nicholas T, Xu, Haitao & Bodenschatz, Eberhard 2006 A quantitative study of three-dimensional lagrangian particle tracking algorithms. *Experiments in Fluids* **40** (2), 301–313.

Pan, Y. & Banerjee, S. 1996 Numerical simulation of particle interactions with wall turbulence. *Phys. Fluids* **8** (10), 2733–2755.

Paris, Anthony Dana 2001 Turbulence attenuation in a particle-laden channel flow .

Petersen, Alec J, Baker, Lucia & Coletti, Filippo 2019 Experimental study of inertial particles clustering and settling in homogeneous turbulence. *Journal of Fluid Mechanics* **864**, 925–970.

Picano, Francesco, Breugem, Wim-Paul & Brandt, Luca 2015 Turbulent channel flow of dense suspensions of neutrally buoyant spheres. *Journal of Fluid Mechanics* **764**, 463–487.

Pope, S. B. 2000 *Turbulent Flows*. Cambridge, UK: Cambridge Univ. Press.

Rabencov, B, Arca, J & van Hout, R 2014 Measurement of polystyrene beads suspended in a turbulent square channel flow: Spatial distributions of velocity and number density. *International Journal of Multiphase Flow* **62**, 110–122.

Reeks, MW 1983 The transport of discrete particles in inhomogeneous turbulence. *Journal of aerosol science* **14** (6), 729–739.

Reeks, Michael W 2014 Transport, mixing and agglomeration of particles in turbulent flows. In *Journal of Physics: Conference Series*, , vol. 530, p. 012003. IOP Publishing.

Richter, David H & Sullivan, Peter P 2013 Momentum transfer in a turbulent, particle-laden couette flow. *Physics of Fluids* **25** (5), 053304.

Richter, David H & Sullivan, Peter P 2014 Modification of near-wall coherent structures by inertial particles. *Physics of Fluids* **26** (10), 103304.

Righetti, M & Romano, Giovanni Paolo 2004 Particle–fluid interactions in a plane near-wall turbulent flow. *Journal of Fluid Mechanics* **505**, 93–121.

Robinson, Stephen K 1991 Coherent motions in the turbulent boundary layer. *Annual Review of Fluid Mechanics* **23** (1), 601–639.

Rouson, Damian WI & Eaton, John K 2001 On the preferential concentration of solid particles in turbulent channel flow. *Journal of Fluid Mechanics* **428**, 149–169.

Sahu, S, Hardalupas, Y & Taylor, AMKP 2014 Droplet–turbulence interaction in a confined polydispersed spray: effect of droplet size and flow length scales on spatial droplet–gas velocity correlations. *Journal of Fluid Mechanics* **741**, 98–138.

Sahu, S, Hardalupas, Y & Taylor, AMKP 2016 Droplet–turbulence interaction in a confined polydispersed spray: effect of turbulence on droplet dispersion. *Journal of Fluid Mechanics* **794**, 267–309.

Salazar, Juan PLC, De Jong, Jeremy, Cao, Lujie, Woodward, Scott H, Meng, Hui & Collins, Lance R 2008 Experimental and numerical investigation of inertial particle clustering in isotropic turbulence. *Journal of Fluid Mechanics* **600**, 245–256.

Sardina, G, Schlatter, Philipp, Brandt, Luca, Picano, F & Casciola, Carlo Massimo 2012*a* Wall accumulation and spatial localization in particle-laden wall flows. *Journal of Fluid Mechanics* **699**, 50–78.

Sardina, Gaetano, Schlatter, Philipp, Picano, Francesco, Casciola, CM, Brandt, Luca & Henningson, Dan Stafan 2012*b* Self-similar transport of inertial particles in a turbulent boundary layer. *Journal of Fluid Mechanics* **706**, 584–596.

Schiller, L & Naumann, A 1933 Fundamental calculations in gravitational processing. *magazine of the Association of German Engineers* **77**, 318–320.

Schneiders, Lennart, Meinke, Matthias & Schröder, Wolfgang 2017 Direct particle–fluid simulation of kolmogorov-length-scale size particles in decaying isotropic turbulence. *Journal of Fluid Mechanics* **819**, 188–227.

Shaffer, Frank, Gopalan, Balaji, Breault, Ronald W, Cocco, Ray, Karri, SB Reddy, Hays, Roy & Knowlton, Ted 2013 High speed imaging of particle flow fields in cfb risers. *Powder technology* **242**, 86–99.

Shokri, R, Ghaemi, S, Nobes, DS & Sanders, RS 2017 Investigation of particle-laden turbulent pipe flow at high-reynolds-number using particle image/tracking velocimetry (piv/ptv). *International Journal of Multiphase Flow* **89**, 136–149.

Soldati, Alfredo & Marchioli, Cristian 2009 Physics and modelling of turbulent particle deposition and entrainment: Review of a systematic study. *International Journal of Multiphase Flow* **35** (9), 827–839.

Soong, CH, Tuzla, K & Chen, JC 1994 Identification of particle clusters in circulating fluidized bed. *Circulating fluidized bed technology IV* pp. 615–620.

Squires, Kyle D & Eaton, John K 1991 Preferential concentration of particles by turbulence. *Physics of Fluids A: Fluid Dynamics* **3** (5), 1169–1178.

Sumbekova, Sholpan, Cartellier, Alain, Aliseda, Alberto & Bourgoin, Mickael 2017 Preferential concentration of inertial sub-kolmogorov particles: The roles of mass loading of particles, stokes numbers, and reynolds numbers. *Physical Review Fluids* **2** (2), 024302.

Sundaram, Shivshankar & Collins, Lance R 1997 Collision statistics in an isotropic particle-laden turbulent suspension. part 1. direct numerical simulations. *Journal of Fluid Mechanics* **335**, 75–109.

Sundaram, Shivshankar & Collins, Lance R 1999 A numerical study of the modulation of isotropic turbulence by suspended particles. *Journal of Fluid Mechanics* **379**, 105–143.

Sundaresan, Sankaran, Ozel, Ali & Kolehmainen, Jari 2018 Toward constitutive models for momentum, species, and energy transport in gas–particle flows. *Annual review of chemical and biomolecular engineering* **9**, 61–81.

Taniere, A, Oesterle, B & Monnier, JC 1997 On the behaviour of solid particles in a horizontal boundary layer with turbulence and saltation effects. *Experiments in Fluids* **23** (6), 463–471.

Tartan, Mehmet & Gidaspow, Dimitri 2004 Measurement of granular temperature and stresses in risers. *AIChE Journal* **50** (8), 1760–1775.

Tenneti, Sudheer & Subramaniam, Shankar 2014 Particle-resolved direct numerical simulation for gas-solid flow model development. *Annual review of fluid mechanics* **46**, 199–230.

Uhlmann, Markus & Doychev, Todor 2014 Sedimentation of a dilute suspension of rigid spheres at intermediate galileo numbers: the effect of clustering upon the particle motion. *arXiv preprint arXiv:1406.1667* .

Vance, Marion W, Squires, Kyle D & Simonin, Olivier 2006 Properties of the particle velocity field in gas-solid turbulent channel flow. *Physics of Fluids* **18** (6), 063302.

Varaksin, A Yu, Polezhaev, Yu V & Polyakov, Anatoly F 2000 Effect of particle concentration on fluctuating velocity of the disperse phase for turbulent pipe flow. *International journal of heat and fluid flow* **21** (5), 562–567.

Varas, AE Carlos, Peters, EAJF & Kuipers, JAM 2017 Experimental study of full field riser hydrodynamics by piv/dia coupling. *Powder Technology* **313**, 402–416.

Voth, Greg A, La Porta, Arthur, Crawford, Alice M, Alexander, Jim & Bodenschatz, Eberhard 2002 Measurement of particle accelerations in fully developed turbulence. *Journal of Fluid Mechanics* **469**, 121–160.

Vreman, AW 2007 Turbulence characteristics of particle-laden pipe flow. *Journal of fluid mechanics* **584**, 235–279.

Vreman, AW 2015 Turbulence attenuation in particle-laden flow in smooth and rough channels. *Journal of Fluid Mechanics* **773**, 103–136.

Wang, Guiquan, Abbas, Micheline & Climent, Éric 2017 Modulation of large-scale structures by neutrally buoyant and inertial finite-size particles in turbulent couette flow. *Physical Review Fluids* **2** (8), 084302.

Wang, Guiquan & Richter, David 2018 Modulation of the turbulence regeneration cycle by inertial particles in planar couette flow. *arXiv preprint arXiv:1807.02107* .

Wang, Lian-Ping & Maxey, Martin R 1993 Settling velocity and concentration distribution of heavy particles in homogeneous isotropic turbulence. *Journal of fluid mechanics* **256**, 27–68.

Weit, A, Roche, Olivier, Dubois, T & Manga, M 2018 Experimental measurement of the solid particle concentration in geophysical turbulent gas-particle mixtures. *Journal of Geophysical Research: Solid Earth* **123** (5), 3747–3761.

Weit, A, Roche, Olivier, Dubois, T & Manga, M 2019 Maximum solid phase concentration in geophysical turbulent gas-particle flows: Insights from laboratory experiments. *Geophysical Research Letters* **46** (12), 6388–6396.

Westerweel, Jerry & Scarano, Fulvio 2005 Universal outlier detection for piv data. *Experiments in fluids* **39** (6), 1096–1100.

Wilkinson, M & Mehlig, Bernhard 2005 Caustics in turbulent aerosols. *EPL (Europhysics Letters)* **71** (2), 186.

Wood, AM, Hwang, W & Eaton, JK 2005 Preferential concentration of particles in homogeneous and isotropic turbulence. *International journal of multiphase flow* **31** (10-11), 1220–1230.

Wu, Yi, Wang, Hangfeng, Liu, Zhaohui, Li, Jing, Zhang, Liqi & Zheng, Chuguang 2006 Experimental investigation on turbulence modification in a horizontal channel flow at relatively low mass loading. *Acta Mechanica Sinica* **22** (2), 99–108.

Wylie, Jonathan J & Koch, Donald L 2000 Particle clustering due to hydrodynamic interactions. *Physics of Fluids* **12** (5), 964–970.

Xu, Jing & Zhu, J-X 2011 Visualization of particle aggregation and effects of particle properties on cluster characteristics in a cfb riser. *Chemical engineering journal* **168** (1), 376–389.

Yang, Jingsi & Zhu, Jesse 2014 A novel method based on image processing to visualize clusters in a rectangular circulating fluidized bed riser. *Powder technology* **254**, 407–415.

Yang, Jingsi & Zhu, Jesse 2015 Visualization of solids phase separation in a rectangular cfb riser using a novel image calibration method. *Powder Technology* **273**, 76–82.

Yang, TS & Shy, SS 2005 Two-way interaction between solid particles and homogeneous air turbulence: particle settling rate and turbulence modification measurements. *Journal of fluid mechanics* **526**, 171–216.

Young, John & Leeming, Angus 1997 A theory of particle deposition in turbulent pipe flow. *Journal of Fluid Mechanics* **340**, 129–159.

Zamansky, Rémi, Coletti, Filippo, Massot, Marc & Mani, Ali 2016 Turbulent thermal convection driven by heated inertial particles. *Journal of Fluid Mechanics* **809**, 390–437.

Zhang, Haifeng & Ahmadi, Goodarz 2000 Aerosol particle transport and deposition in vertical and horizontal turbulent duct flows. *Journal of Fluid Mechanics* **406**, 55–80.

Zhao, LH, Andersson, Helge I & Gillissen, JJJ 2010 Turbulence modulation and drag reduction by spherical particles. *Physics of Fluids* **22** (8), 081702.

Zhou, J, Grace, JR, Qin, S, Brereton, CMH, Lim, CJ & Zhu, J 1994 Voidage profiles in a circulating fluidized bed of square cross-section. *Chemical Engineering Science* **49** (19), 3217–3226.

Appendix A

A.1 Electrostatic dissipative acrylic

Electrostatic dissipative acrylic (SciCron Technologies) is used to build the optical test section, and the channel is provided with static discharge wires grounded to structural supports. This prevents the particles from accumulating upon impaction and building up unwanted roughness, an effect that has impacted past experiments (Benson *et al.*, 2005). The importance of such precautions is illustrated in figure A.1, where cumulative wall-normal profiles of particle concentrations are plotted in the higher volume fraction case. The details of how those measurements are obtained are given in §2.2. When using standard acrylic walls, the concentration profiles start with a strong near-wall peak but drift in time, with particles migrating away from the wall. This is likely the consequence of wall deposition which leads to significant roughness (as verified by inspecting the wall surface at the end of the experiments), in turn altering the collision dynamics and ultimately enhancing particle dispersion towards the channel core. Using electrostatic dissipative acrylic virtually eliminates particle deposition (as also verified by direct wall inspection) and warrants consistent concentration profiles during each run and between different runs.

A.2 Coefficient of restitution

The coefficient of restitution, e for particle-wall collisions is measured by dropping individual glass beads from a height of 350 mm above a horizontal plate made of the same

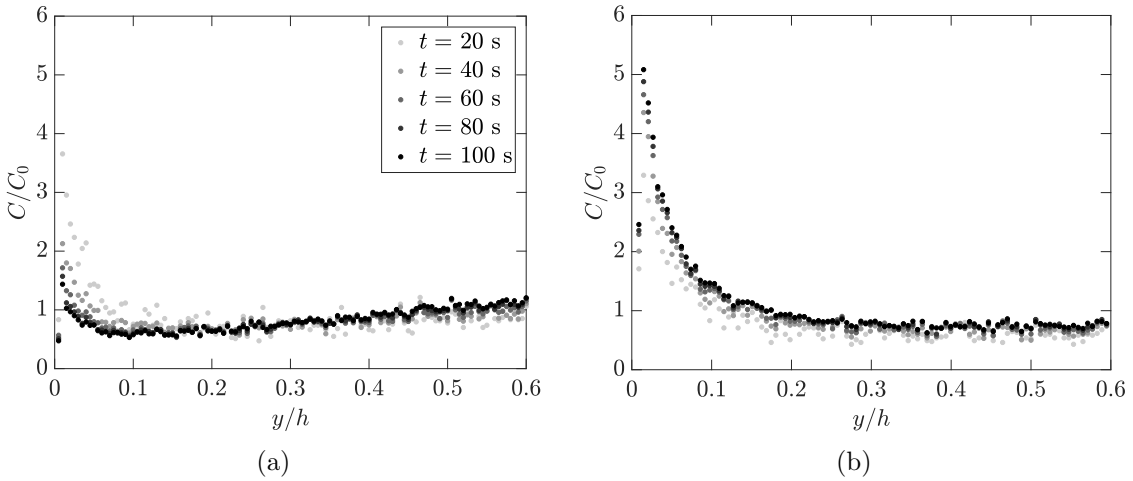

Figure A.1: Wall-normal profiles of mean concentration for recordings of different durations, using (a) standard acrylic and (b) electrostatic dissipative acrylic. $C_0 = 880$ particles/cm^3, corresponding to $\phi_v = 5 \times 10^{-5}$ for both cases. Refer to table 2.2 for definitions on y, h.

acrylic used for the test section. The particles reach steady-state terminal velocity before bouncing on the plate. This is achieved independently from the method of release due to the short free-fall stopping distance (of order $\tau_p^2 g \sim 3$ mm). Particles are imaged at 2300 fps with a high-speed CMOS camera (VEO 640) paired with a 200 mm lens at f/4, and tracked using the same method used for the particle-laden flow measurements. The coefficient of restitution e is defined as the ratio of the wall-normal particle velocity just after and just before the collision, and is calculated averaging over five trials as shown in figure A.2.

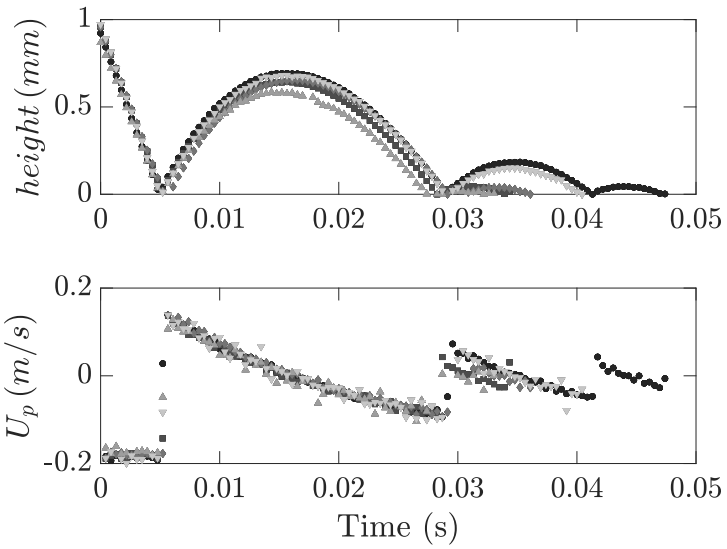

Figure A.2: Particle height and vertical velocity data used for determining the restitution coefficient for particle-wall collisions over five trials. Positive velocity indicates upward motion.Tracks for each trial are shown in markers of different shapes and colors.

Appendix B

Tracking step for continuing cluster tracks

A cluster is terminated when its centroid is not found at close proximity in the subsequent frame, having dissipated into concentrations lower than the threshold T. Alternately, it may have undergone a merging or breaking event, and its shape has changed dramatically such that the centroid had a very large displacement. An additional tracking step is applied at the end of each cluster track to capture this dynamic.

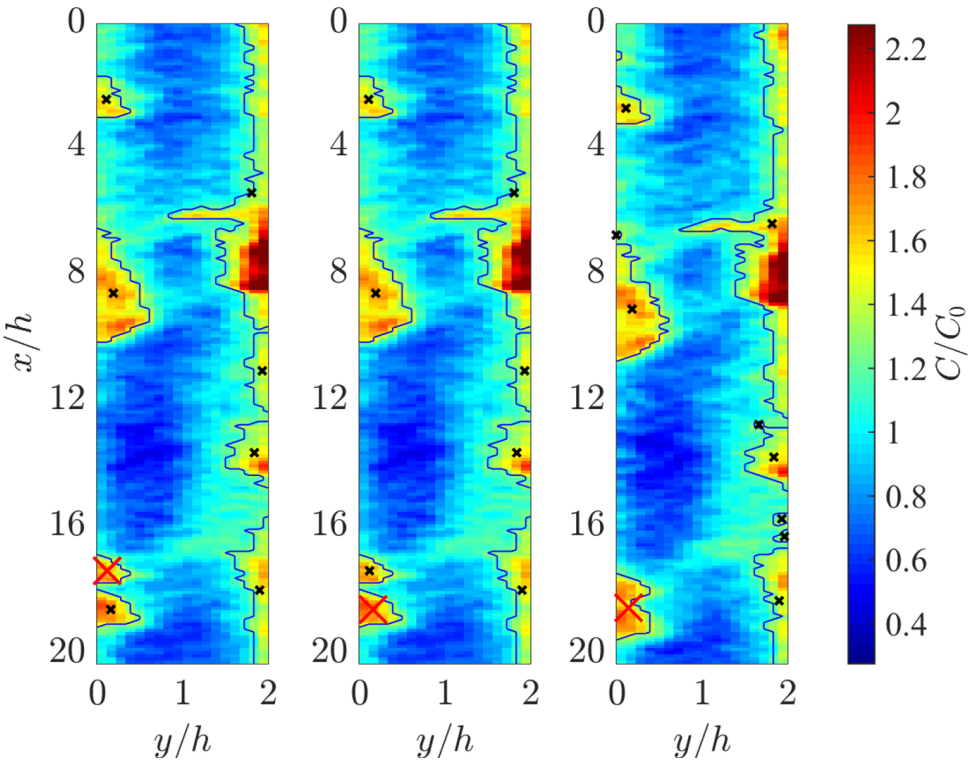

Figure B.1: An illustration of two clusters A (left) and B (middle) merging to form cluster C (right). The large red cross indicates the targeted cluster.

Cluster merging example (figure B.1):

- Cluster A (left) and B (middle) terminates at the same frame.
- A search is performed to check if interrogation windows associated with cluster A are found within a different cluster in the next frame, and the same is done for cluster B.
- If a cluster, C is found to consist of more than 50% of the interrogation windows formerly associated with cluster B, then cluster C is deemed a continuation of cluster B (and cluster A is deemed to be terminated).

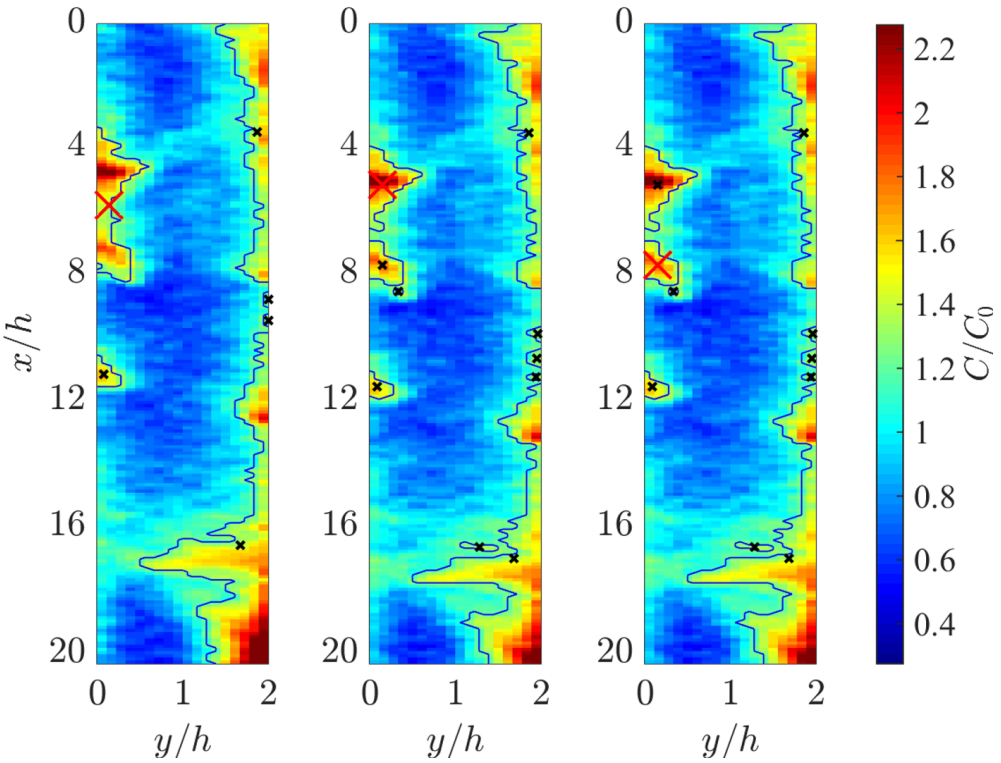

Figure B.2: An illustration of a cluster D (left) breaking to form two clusters E (middle) and F (right). The large red cross indicates the targeted cluster.

Cluster breaking example (figure B.2):

- Cluster D (left) terminates by breaking into two clusters E (middle) and F (right).
- If cluster E shares more than 50% of the members (i.e., interrogation windows associated with the cluster) with those of the former cluster D, the cluster E is deemed to be a continuation of cluster D (and cluster F is a new cluster).

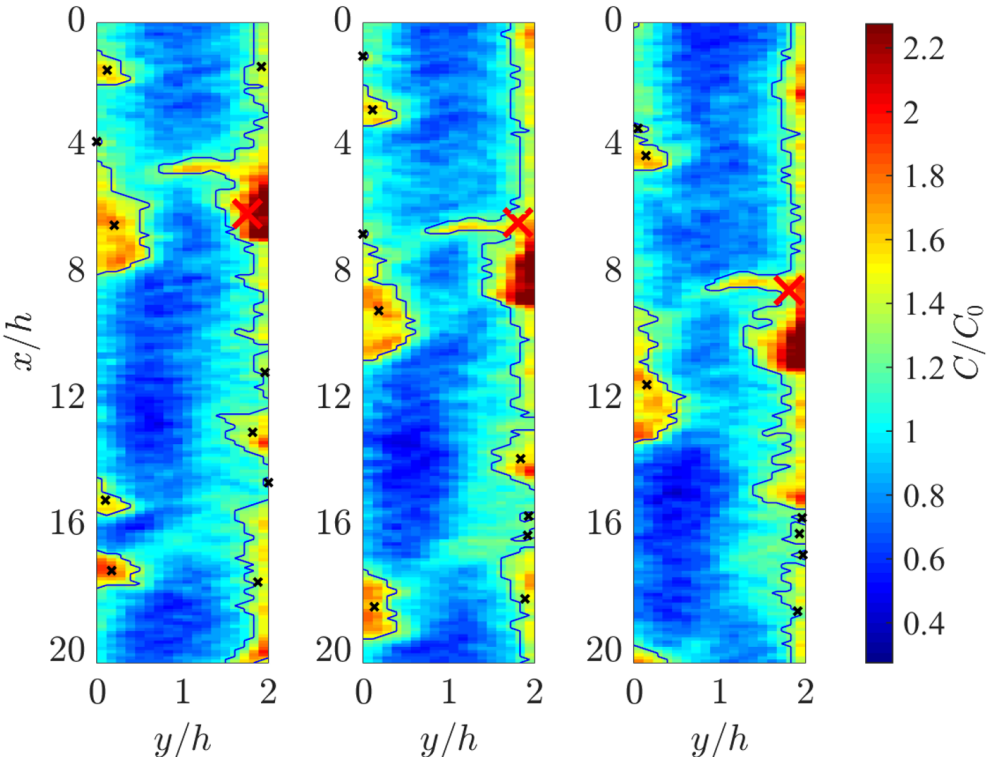

Figure B.3: This large cluster (indicated by large red cross) has undergone multiple merging events, but is still regarded as one cluster over the course of its lifetime.